Thermoelectric Studies of P-Type Narrow-Bandgap Bi-Sb and Modeling of Transport Properties

Xixiao Hu

A Dissertation Presented to the Graduate Faculty
of the University of Virginia in Candidacy for the Degree of
Doctor of Philosophy

Department of Physics
University of Virginia
Sept, 2021

Abstract

Thermoelectric research has been performed on p-type Bi-Sb system. We systematically study the doping effects of Ge, Sn, and Pb in Bi-Sb alloys. The samples are made using the melt spinning technique and the spark plasma sintering method. A “high pressure low temperature” method is developed to resolve the low solubility issue of Ge and Pb in Bi-Sb. We observe an increased doping level for Ge and an increased doping efficiency for Pb in Bi-Sb. Several strategies have been applied to enhance the thermoelectric performance of p-type Bi-Sb samples including the Ge + Pb/Sn co-doping method, transition metal + Sn/Pb co-doping method, Te + Sn/Pb co-doping method and the post high-pressure method. Enhanced power factors are obtained in p-type Bi-Sb samples and most of them can be attributed to the decreased ratio of the electron mobility to the hole mobility. The thermal conductivity is measured using the hot disk method. The $Bi_{88}Sb_{12}Ni_1Pb_{0.5}$ sample shows a peak of figure of merit $zT \sim 0.13$ around 200 K which is comparable to the performance of the best single crystal p-type Bi-Sb by far.

We apply a two-band effective mass model to fit the data of undoped and pure Ge, Sn, and Pb doped Bi-Sb samples and the band gap is set as a changing parameter. We find that the band gap needs to shrink as temperature rises in order to fit the data well. This helps explain why it is difficult to achieve a good thermoelectric performance in p-type Bi-Sb system. If the band gap shrinks as temperature rises, the electron channel starts to contribute to the transport at relatively low temperature which is detrimental to the p-type Seebeck coefficient.

Besides, the bipolar thermal conductivity becomes significant with both the hole channel and the electron channel participating the transport. Those factors lead to a low figure of merit zT for p-type Bi-Sb.

Moreover, we have studied p-type Si-Ge alloys. The ball milling technique and the spark plasma sintering method are applied to synthesize Si-Ge samples. We measure the resistivity and the Seebeck coefficient of Fe/Ni/Mo codoped Si-Ge, Si-Ge embedded with aerogel particles, and Si-Mo-B samples. The carrier concentration and the carrier mobility are affected by the Fe/Ni/Mo and aerogel particles which change the electrical conductivity and the Seebeck coefficient of Si-Ge alloys. Overall, we get about 10 % increase of the power factor in the transition metal codoped Si-Ge compared with the referenced p-type Si-Ge result.

Acknowledgements

Sincere appreciation to my advisor, Prof. Joseph Poon for his help and guidance though my PhD study and research. His tough-minded attitude towards research affects me a lot which helps me build the courage and independence in facing challenges and solving problems.

Thanks to Dr. Sheng Gao, who is my co-worker in the group and my friend. He trains me on using most of the apparatus in the lab with excellent explanations on the functionalities and provides much help on doing experiments and calculations.

Thanks to Prof. Patrick Hopkins and Dr. John Gaskins for the thermal conductivity measurement, and Kathleen Tomko for the help on getting scanning electron microscope images.

Thanks to Prof. Utpal Chatterjee, Prof. Jongsoo Yoon, and Prof. Mona Zebarjadi for serving on my thesis committee.

Thanks to Prof. Mona Zebarjadi, Prof. Subhendra D. Mahanti, Prof. Mark Lundstrom, Dr. Xufeng Wang, and Dr. Normand Modine for the valuable discussions on thermoelectrics.

Thanks to my friends Y. Du, J. Qi, L. Chen, S. Jian, M. Hua, C. Duan, and T. Chen. They provide much help in my life and insights which make me a better person.

Thanks to my parents and family members. They always trust me and support me to fulfill my goals.

Contents

List of Figures

List of Tables

Chapter 1

Introduction of thermoelectrics

Energy has become one of the central concepts in human society since the first industrial revolution. However, accompanied with the development of the energy technology, pollution to the environment and excess carbon dioxide to the atmosphere have become severe problems. In recent years, people have made a lot efforts on resolving the environmental problems. One of the directions is to find ways to generate clean energy. Thermoelectric (TE) technology is one of the technologies that can help generate energy in an environmentally friendly way [1]. In everyday life, a lot of heat energy, such as the heat generated by the vehicles' engines, is dissipated into the environment without recycling. With the help of the thermoelectric technology, we are able to save energy by converting heat into electrical energy and make the energy usable again.

1.1 Thermoelectric effects

To understand how and why thermoelectric technology works, we need to look into the mechanisms of the thermoelectric effects.

The three main thermoelectric effects are the Seebeck effect, Peltier effect, and Thomson effect. The Seebeck effect is mainly about converting the temperature gradient into the voltage difference at the joints of two materials. The Peltier effect involves a flowing electrical current in a circuit made by two connected materials and the phenomenon of generating and absorbing energy at the joints. When we apply both the current and the temperature gradient on a material, here comes the extra heating and cooling along the material and this is called the Thomson effect. The details of those three effects are introduced in the following sections separately.

1.1.1 Seebeck effect

The Seebeck effect is named after the German physicist Thomas Johann Seebeck[2]. It is discovered by Italian scientist Alessandro Volta in 1794 and independently rediscovered by Thomas Johann Seebeck in 1821.

There are two descriptive definitions on Seebeck effect. The first one is from the original observation point of view which involves two kinds of different materials. When we loop two different metal wires together, such as iron and copper, and set the two joints at different temperatures, an electrical current would be created through the wires. Because in different materials, the chemical potential changes with temperature differently, that causes an electrical potential difference between the joints which leads to the electrical current.

The other definition involves only a single material. The Seebeck effect is defined as the electromotive force (EMF) or voltage build up along the material when we set the two ends of the material at different temperatures. Based on this definition, we can use an equation to describe the capability of the material to convert the temperature difference into the voltage difference, which is called the Seebeck coefficient S:

$$S = -\frac{\Delta V}{\Delta T} \tag{1.1}$$

where ΔV and ΔT are the voltage difference and temperature difference between the two ends of the material respectively.

In general, the Seebeck coefficient can be measured given a small temperature gradient along the material. We can measure the voltage difference between the two ends and divide it by the temperature difference. In the real measurement of Seebeck coefficient, we usually use the four-probe method [3] considering that the contact resistance between the material and the electrodes may affect the measurement result.

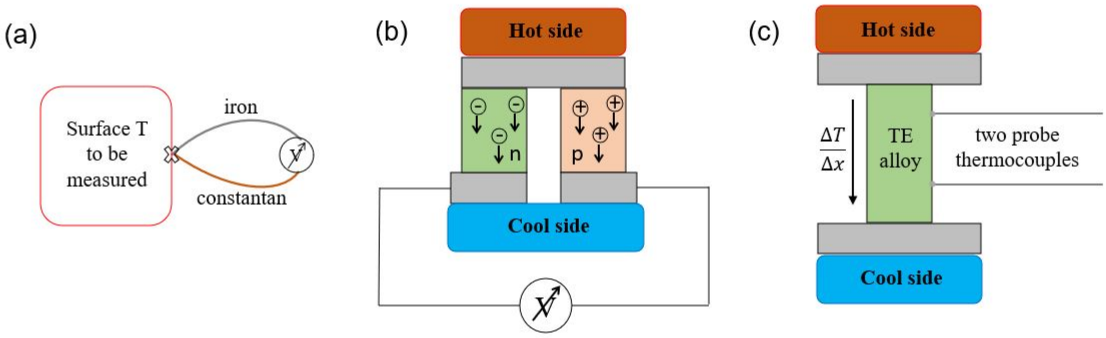

Figure 1.1: (a) Diagram of a thermocouple (b) Mechanism of the Seebeck effect (c) Set-up of measuring the Seebeck coefficient

In Figure 1.1 (a), we plot a thermocouple made using the iron wire and the constantan wire to demonstrate an application of the Seebeck effect. In (b), we set the n-type TE material and the p-type TE material connected to a hot object at one side and a cool object at the other side. The electrons in the n-type material and the holes in the p-type material would be driven from the hot side to the cool side. After connecting them with a voltage probe, we can find the voltage difference between the joint electrodes. In (c), we show a general four-probe method to measure the Seebeck coefficient of a certain material. The sample is mounted between two electrodes (gray parts in the diagram) which are connected to the current supply. The temperature gradient $\frac{\Delta T}{\Delta x}$ is being applied along the sample. Two probe thermocouples are connected with the sample to measure the voltage difference and the temperature difference. Considering the two electrodes and the two thermocouples connected with the sample, the method is called the four-probe method.

In terms of a microscopic point of view, we can understand the Seebeck effect with the help of a free electron gas model. When we apply the temperature difference at the two ends of the material, the carriers at the hot end have higher kinetic energy and the carriers at the cold end have lower kinetic energy. Then the carriers at the hot end would diffuse to the cold end. As a result, the carrier density at the cold end would increase. This process stops until the electric field developed by the diffusion of charge carriers prevents the further carrier motion from hot to cold end. That would lead to an electrical potential difference between the hot end and the cold end. The sign of the voltage is dependent on the sign of the major carriers in the material. The Seebeck coefficient is negative if the potential of the cold side is lower than the hot side.

1.1.2 Peltier effect

The Peltier effect is discovered by French physicist Jean Charles Athanase Peltier in 1834 [4]. This effect is kind of a reversed phenomenon to Seebeck effect. When we connect two materials together and apply the current through it, one joint of the materials would generate heat and the other one would absorb heat. Figure 1.2 shows the diagram of the Peltier effect. When considering the total generated heat, Joule heat needs to be considered besides the Peltier heat. This makes it difficult to measure the Peltier heat directly.

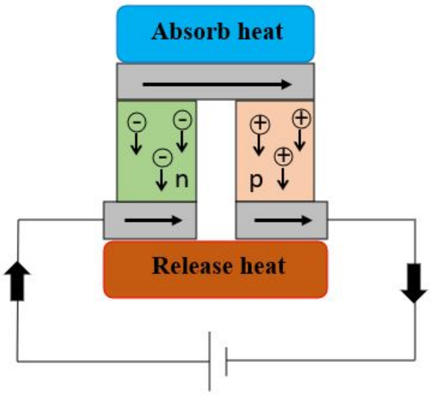

Figure 1.2: Mechanism of the Peltier effect

The Peltier heat can be described by the following equation:

$$\frac{dQ}{dt} = (\Pi_1 - \Pi_2)I \tag{1.2}$$

where $\frac{dQ}{dt}$ is the generated heat per unit time, Π_1 and Π_2 are the Peltier coeffcients of the first conductor and the second conductor, and I represents the electrical current. The Peltier coefficient Π is closely related to the Seebeck coefficient S with the equation:

$$\Pi = TS \tag{1.3}$$

1.1.3 Thomson effect

When we apply both the temperature gradient and current along a material, we can get additional heating or cooling, this effect is called the Thomson effect. William Thomson discovered it in 1851 [5].

Thomson effect can be described using the following equation:

$$\dot{q} = -K\vec{J} \cdot \nabla T \tag{1.4}$$

where $\dot{q}$ is the rate of generated heat per unit volume, $\vec{J}$ is the current density, ∇T is the temperature gradient, and $K = T\frac{dS}{dT}$ is the Thomson coefficient.

1.2 Figure of merit zT

In thermoelectric research, we mostly care about the Seebeck effect/Seebeck coefficient among the three thermoelectric effects. However, in order to convert the heat energy into electrical energy efficiently, a good Seebeck coefficent is not enough. We also need to consider the electrical conductivity and the thermal conductivity. Specifically, we want the material to be a good electrical conductor and a bad thermal conductor. Here a figure of merit zT is defined to describe the material's capability of energy conversion.

The equation for figure of merit zT is

$$zT = \frac{\sigma S^2 T}{\kappa} \tag{1.5}$$

where σ is the electrical conductivity, S is the Seebeck coefficient, κ is the thermal conductivity which can be separated as the electrical thermal conductivity κ_e and the lattice thermal conductivity κ_L.

The electrical thermal conductivity κ_e is related to the electrical conductivity σ by the Wiedemann-Franz law:

$$\kappa_e = L\sigma T \tag{1.6}$$

where L is called the Lorenz number and theoretically is a constant for metals:

$$L = \frac{\pi^2}{3}\left(\frac{k_B}{e}\right)^2 \tag{1.7}$$

where k_B is the Boltzmann constant and e is the unit charge. For semiconductors, the value of the Lorenz number depends on the scattering mechanisms in the material [6].

zT is proportional to the electrical conductivity, the square of the Seebeck coefficient, the temperature and reversely proportional to the thermal conductivity. In order to enhance the figure of merit zT, we need to improve the power factor which is defined as σS^2 while keep the thermal conductivity low. However, it is difficult to achieve that goal because the electrical conductivity, the Seebeck coefficient and the thermal conductivity are entangled together. We can see the relation from the Wiedemann-Franz law Equation 1.6 and the single band Seebeck coefficient Equation 1.8. When we try to improve one of the transport properties, the other two tend to become worse. This is the challenging part in thermoelectric research.

The Seebeck coefficient of a single band degenerate semiconductor can be expressed as [7]:

$$S = m_d^* \frac{8\pi^2 k_B^2 T}{3eh^2}\left(\frac{\pi}{3n}\right)^{2/3} \tag{1.8}$$

where m_d^* is density of states effective mass, k_B is the Boltzmann constant, e is the unit charge, h is the Planck constant and n is the carrier concentration. As the carrier concentration increases, the electrical conductivity $\sigma = n\mu e$ increases while the Seebeck coefficient decreases. μ is the mobility of the charge carriers.

To overcome the problem, researchers have tried a lot of methods. To increase the power factor, a usual way is through doping. By adding dopants into the alloy matrix, the carrier concentration and the scattering time can be changed [8], [9]. That can affect the electrical conductivity and the Seebeck coefficient and make it possible to optimize the power factor. Nano-structure process [10]–[13] is applied to decrease the thermal conductivity κ since it can increase the grain boundary scattering which leads to a lower lattice thermal conductivity κ_L while the power factor keeps roughly the same. Besides, the energy filter mechanism [14], [15] and resonant states mechanism [7], [16] have been applied to enhance the power factor of the materials.

1.3 Thermoelectric material

In terms of the material point of view, we can categorize the materials into metal, insulator, semi-metal, and semiconductor based on materials' electrical conductivities.

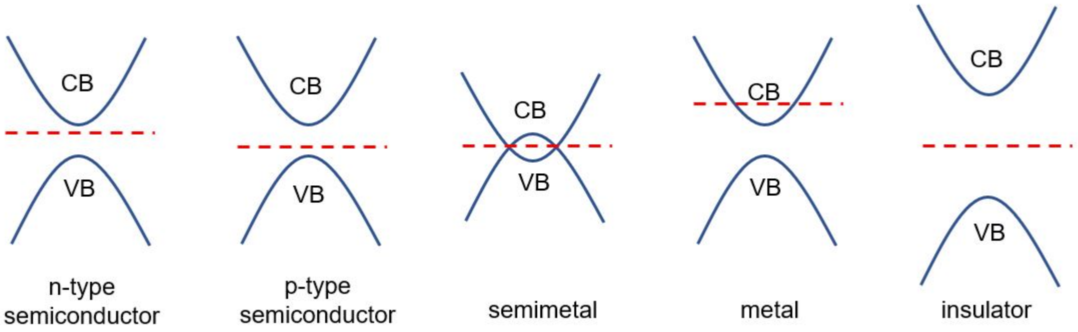

Figure 1.3: Diagrams of semiconductor, semimetal, metal and insulator

In the Figure 1.3, the difference between metal, insulator, semi-metal and semiconductor can be explained using the energy band model. CB represents the conduction band, VB represents the valence band, and the red line indicates the position of the Fermi level. For metal and semi-metal, the Fermi levels position in the bands, while for insulator and semiconductor, the Fermi levels position in the band gaps. The conduction band overlaps with the valence band in the semi-metal. For n-type semiconductor, the Fermi level is closer to the conduction band so that electrons can be thermally excited and raise the electrical conductivity. In contrast, the Fermi level is closer to the valence band for p-type semiconductor and the major carriers are holes. For insulator, the band gap is large and raising temperature cannot effectively make enough electrons or holes participate in the transport and the electrical conductivity stays low.

Metals generally have good electrical conductivities which are good for the power factor. However, the Seebeck coefficient is small for metals, typically several microvolts per Kelvin. Because for metallic systems, the electronic states below the Fermi level have a positive contribution to the Seebeck coefficient while the electronic states above the Fermi level have an opposite contribution to the Seebeck coefficient. The two parts compensate with each other, leading to a small total Seebeck coefficient. In the end, the power factors for metals are low because of the small Seebeck coefficient.

For insulators, the power factor is mainly restricted by the low electrical conductivies. Even though insulators may have decent Seebeck coefficent, the electrical transport is obstacled by the high resistance of the material.

For semi-metals, it's possible to get good thermoelectric performance if there is a significant asymmetry between the valence band and the conduction band [17]. That can lead to a large Seebeck coefficient which benefits the figure of merit zT.

Researchers have found that the semiconductor kind of materials have the best thermoelectric performance in most of the temperature ranges [7], [9], [11], [16], [18]–[20]. For semiconductors, the materials can be either n-type or p-type controlled by doping, with either electrons or holes as the major charge carriers. Since the compensation between electrons and holes is avoided, strong Seebeck coefficient is obtained in semiconductors. A good thermoelectric semiconductor has a Seebeck coefficient as high as hundreds of microvolts per Kelvin. With the decent electrical conductivity and thermal conductivity, semiconductors are the most promising type of materials in which we can search for good thermoelectric properties.

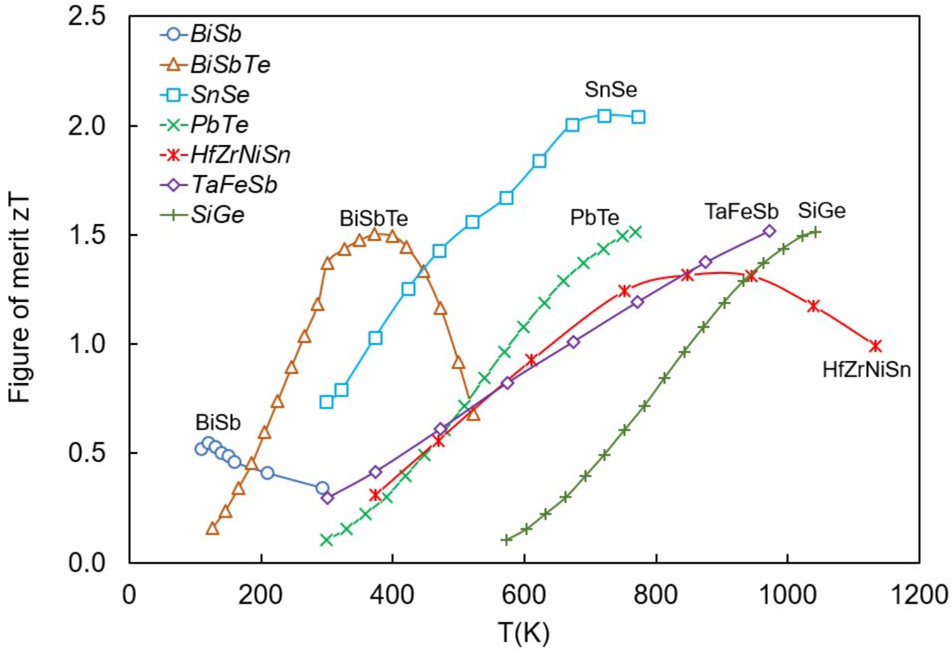

Figure 1.4: Figure of merit zT of different thermoelectric materials

Semiconductor and insulator both have band gaps. However, for semiconductors, the band gap is relatively small. As temperature rises, the energy is high enough to excite the charge carriers and make semiconductor conductive. This is the reason why the resistivity curve of semiconductors rises up at lower temperature and decreases at higher temperature.

The properties of semiconductors can be tuned by adding dopants into the system. The effect of dopants is determined by both the dopant element itself and also the matrix. The dopant atoms work as either electron acceptors or donors. For example, silicon is a group 14 element. We can add boron, which is a group 13 element, into the system and get a p-type semiconductor. Or we can add phosphorus, which is a group 15 element, into the system and get a n-type semiconductor.

In Figure 1.4, we plot the figure of merit zT of several typical TE materials over a wide temperature range. BiSb, ref.[18]; BiSbTe, ref.[19]; SnSe, ref.[9]; PbTe, ref.[7]; TaFeSb, ref.[20]; SiGe, ref.[11]; HfZrNiSn, ref.[16].

1.4 Thermoelectric device

After we find good thermoelectric materials, the important thing to do is to build thermoelectric devices using those materials and test their energy conversion efficiency.

Compared with conventional power generators or coolers, thermoelectric devices have the advantage of being environmentally friendly, small size, quiet, stable and less need for maintenance [1]. However, the thermoelectric devices do not have as good energy conversion efficiency as conventional devices. This limits the wide use of the thermoelectric devices.

1.4.1 Thermoelectric cooler

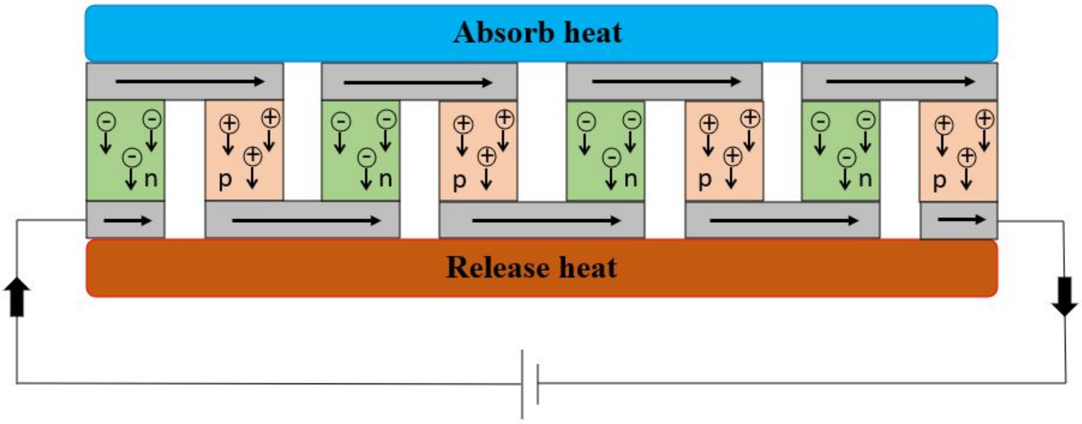

Figure 1.5: Diagram of a cooler made using the Peltier effect

Since we can use the Peltier effect to absorb heat, this mechanism can be applied to build thermoelectric coolers.

As we set up a current going through the circuit with connected n-type legs and p-type legs, the system can transport heat from a source to a sink. Figure 1.5

shows the schematic diagram of the thermoelectric cooler.

1.4.2 Thermoelectric power generator

Based on the Seebeck effect, we can build a thermoelectric generator by connecting many n-type and p-type legs of thermoelectric materials and put the two ends at different temperatures. As they are connected and the temperature gradient is maintained, we can get electric current going through the circuit and that forms a thermoelectric power generator.

As Figure 1.6 shows, after we set up the heat source and the sink, the charge carriers in both the n-type leg and the p-type leg move from the hot end towards the cold end. They will neutralize at the cold end. As the temperature gradient is maintained, this process will not stop. The conversion from heat energy to electrical energy is then achieved.

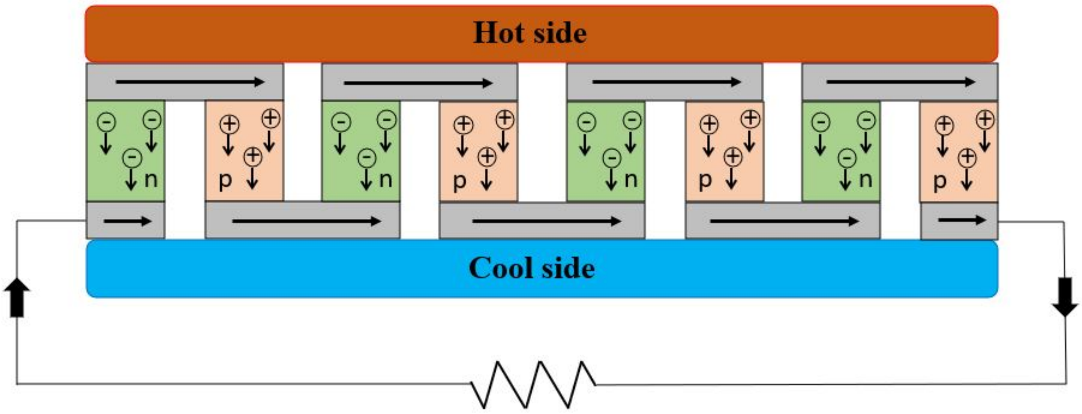

Figure 1.6: Diagram of a power generator made using the Seebeck effect

1.4.3 Energy conversion efficiency

Knowing the zT value of a certain material is not enough to calculate the energy conversion efficiency of a device which is composed of a n-type leg material and a p-type leg material. The relation between the energy conversion efficiency and the figure of merit zT of the two materials is introduced in this section.

The energy conversion efficiency is related to the figure of merit ZT of the thermocouples. Here we use the big Z in ZT to differentiate the device ZT from the material zT. We need to consider both the n-type leg (electrical conductivity σ_n, Seebeck S_n, and thermal conductivity κ_n) and the p-type leg (electrical conductivity σ_p, Seebeck S_p, and thermal conductivity κ_p) in the calculation of the device Z as shown in Equation 1.9. In order to achieve the highest figure of merit of the thermocouple, the two legs need to match each other to satisfy the geometry conditions [3].

The device Z is given by the following equation:

$$Z = \frac{(S_n - S_p)^2}{[(\kappa_n/\sigma_n)^{1/2} + (\kappa_p/\sigma_p)^{1/2}]^2} \tag{1.9}$$

Although there's a minus sign between the Seebeck coefficient S_n and S_p, it doesn't mean that we should subtract S_p from S_n since the sign of S_n is negative. The correct understanding is that we add the absolute value of the n leg Seebeck coefficient and p leg Seebeck coefficient and square it to get the numerator.

If we know the maximum temperature difference ΔT_{max} in a Peltier cooler, we can use it to calculate the ZT_{cooler} with Equation 1.10 [1], [3].

$$\Delta T_{max} = \frac{ZT^2_{cooler}}{2} \tag{1.10}$$

The relation between the TE generator efficiency η and the device ZT is described in Equation 1.11 [1], [3].

$$\eta = \frac{\Delta T}{T_{hot}} \cdot \frac{\sqrt{1+ZT} - 1}{\sqrt{1+ZT} + T_{cold}/T_{hot}} \tag{1.11}$$

where T_{hot} is the temperature of the heat source and T_{cold} is the temperature of the heat sink. The energy conversion efficiency of devices also depends on the compatibility between the n-type and p-type legs. If the n-type and p-type materials are incompatible, then the device ZT can be much lower than the zT

of the materials [21].

Chapter 2

Sample synthesis and characterization methods

As we discussed in the section of the figure of merit zT, the good thermoelectric material needs to have a decent power factor σS^2 and a low thermal conductivity κ. Besides, we expect that the experimental result should be reproducible and that put a requirement on the sample quality. The sample needs to be as homogeneous as possible and better to have only single phase. An inhomogeneous sample may have a wide range fluctuation of the distribution of elements inside it and that may affect the overall transport properties. A sample with a second phase tends to be inhomogeneous especially in a doped sample. Because the doping particles may form a second phase with one of the matrix elements and that distribution of the second phase is usually inhomogeneous. Another possibility that may cause the inhomogeneity is: when the doping level is high, the doping particles can cluster at certain positions in the alloy matrix and leave the other space with less doping particles. In this chapter, we introduce the experimental methods on how to make Bi-Sb and Si-Ge alloys with good quality and how to characterize samples' compositional and transport properties.

2.1 Sample synthesis methods

We have applied the following procedures to make Bi-Sb alloys and Si-Ge alloys.

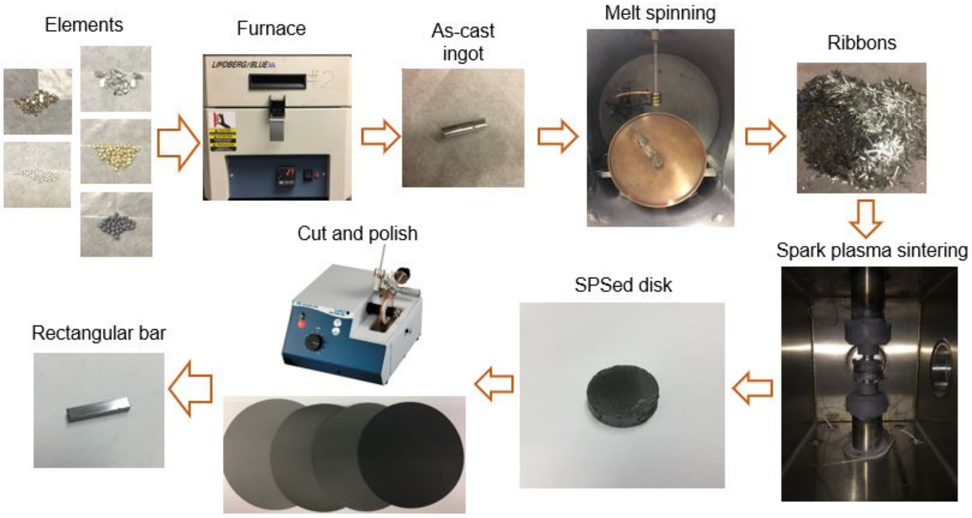

Figure 2.1: The typical sample making procedures of Bi-Sb

Procedures to make the Bi-Sb alloys:

Weigh the elements → put the elements into a quartz tube → vacuum the tube → put the quartz tube into a furnace → get the ingot out of the quartz tube and break the ingot into pieces → put the pieces into a quartz tube with a small hole → put the tube into the melt spinning system → vacuum the chamber of the melt spinning system → perform the melt spinning and collect the ribbons → powderize the melt spinning ribbons → put the powder into the graphite mold → put the mold into the chamber of the spark plasma sintering (SPS) system → vacuum the chamber and backfill it with argon → perform the sintering process → take the compact disk formed in the SPS process outside the mold → polish the surface of the disk and cut the disk into a rectangular bar → polish the sample again until it shows shiny metallic surface → measure the sample's transport properties on the physical properties measurement system

Figure 2.1 shows the pictures of most of the procedures described above.

To make the Si-Ge alloys, we apply the ball mill method to powderize the particles instead of using melt spinning. Besides, we use the ZEM-3 system to characterize the transport properties instead of using PPMS. The other procedures are similar to the procedures to make Bi-Sb.

Procedures to make the Si-Ge alloys: Weigh the elements → put the elements into a ball mill jar → ball milling for several hours → collect the ball milled powder from the jar → put the powder into the graphite mold → put the mold into the chamber of the spark plasma sintering (SPS) system → vacuum the chamber and backfill it with argon → perform the sintering process → take the compact disk formed in the SPS process outside the mold → polish the surface of the disk and cut the disk into a rectangular bar → polish the sample again until it shows shiny metallic surface → measure the sample's transport properties on ZEM-3 system

The sample making process can be categorized to three parts: preprocess which involves the experiments on how to prepare powder for sintering; in-process which is the sintering process in the SPS system; and postprocess which involves the afterwards treatment of the SPSed disk and make it prepared for the transport properties measurements. I'll introduce the processes separately in the following sections.

2.1.1 Preprocess

The preprocess of the Bi-Sb alloys includes melting the elements into the as-cast ingot in the furnace and applying the melt spinning with the broken pieces of the ingot. While for the Si-Ge alloys, ball milling is required to obtain the fined powder with nano-size particles.

Furnace

To prepare the as cast ingot of the Bi-Sb alloys, we first need to weigh the elements according to the compositions that we need. The elements are from the Sigma Aldrich and Alfa Aesar company with purity of 99.999%. We put the bismuth and antimony particles into a quartz tube. The quartz tube is vacuumed to avoid the oxidation effects. Bismuth and antimony can form oxides if exposed to oxygen. The existence of bismuth oxides and antimony oxides are not good for the overall thermoelectric properties of the Bi-Sb alloys. Then we seal the quartz tube and put it into a furnace. The melting point of bismuth is 271.5 °C and the melting point of antimony is 630.63 °C. We set the temperature to be 800 °C to melt normal Bi-Sb alloys and raise it to 875 °C if some dopants with high melting point (germanium, iron and nickel) are added into the alloy matrix. After the furnace reach the setting temperature, we let it stay at the temperature for $1 \sim 3$ hours and shack the tube $1 \sim 2$ times with a pincer during the period. After that, we take out the quartz tube and quench it into liquid nitrogen or water. This quench process is meant to decrease the segregation effect in Bi-Sb alloys [22], [23]. If the temperature decreasing rate is very high, then there is no time for bismuth particles and antimony particles to diffuse and segregate. We find that the difference between using water and liquid nitrogen is small. The as-cast ingot after quench is not homogeneous, we need to apply the melt spinning technique to increase the homogeneity of the samples.

Melt spinning technique

Melt spinning is a technique that can make thin metal ribbons from molten alloy with a high cooling rate [24]. It is used to produce the ribbon of amorphous materials. Since the cooling rate is very high, there is no time for molten alloy to crystalize before it turns into solid. Amorphous phase is then formed. For Bi-Sb alloys, we apply the melt-spinning mostly for the purpose of getting homogeneous samples.

We break the ingot into small pieces and put them into the quartz tube again. A small nozzle is left on the quartz tube so that the molten alloy can be pushed out there. The chamber of the melt spinner is vacuumed and then backfilled with argon gas. The basic set-up for the melt spinning system is shown in Figure 2.2. During the melt spinning process, an alternating current passes

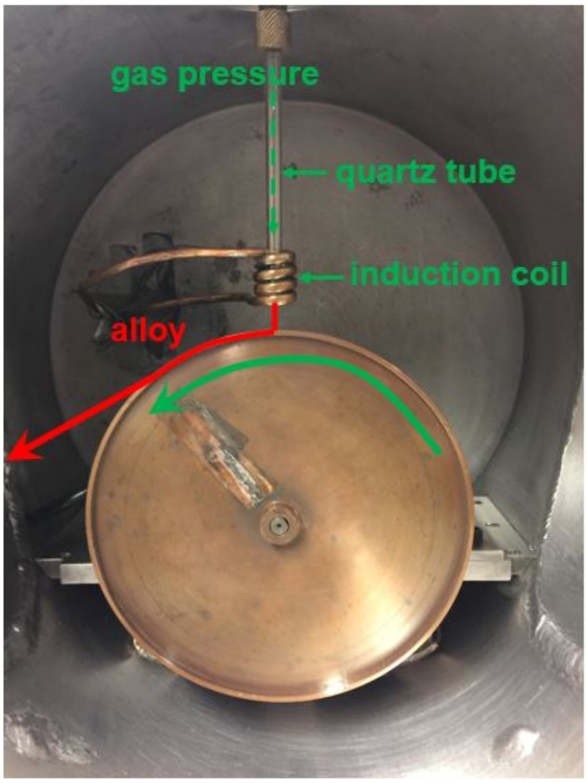

Figure 2.2: The set-up of the melt spinning

through the induction coil and the alloy in the quartz tube becomes melted. Then we turn on the argon gas pressure. The liquid alloy is pushed by the gas and hits on the rotating copper wheel. The surface linear velocity of the wheel is controlled between 10 m/s and 30 m/s. As the wheel rotates, the shear force between the wheel and the molten alloy helps form thin metal ribbons. The viscosity of the molten alloy is expected to be low to get high quality ribbons. Otherwise, if the molten alloy drops discretely from the nozzle and the liquid drop is relatively big, then thin ribbons may not be formed, instead we may get some small circular sheets of metal piece which are usually not as homogeneous as thin ribbons. This process happens very fast, and the cooling rate can be as high as on the order of $10^4 \sim 10^6$ Kelvins per second (K/s). With such a high cooling rate, the segregation between bismuth and antimony particles can be effectively avoided.

Depending on the materials, there are some factors that can affect the quality of the melt-spun ribbons [25]–[27].

1. The nozzle size: the nozzle size we used is between 0.5 mm and 1 mm. This can affect the width of the ribbons.

2. The distance between the nozzle and the copper wheel: we set up the distance to be in range of 1 cm to 2 cm. This can affect the thickness of the ribbons.

3. The surface linear velocity of the copper wheel: this can affect the thickness of the ribbons. We have measured the transport properties of two Bi-Sb samples made using wheel velocity of 10 m/s and 30 m/s and there is no significant difference between those two samples.

The ribbons of Bi-Sb are brittle, we can put the ribbons into a mortar and powderize them using a pestle. After that, the homogeneous Bi-Sb alloy powder is well prepared.

Ball milling

To prepare the powder for Si-Ge alloys, ball milling method is applied. Ball milling method is a kind of grind/mechanical alloy methods which utilizes the mechanical interaction between material particles and metal balls to grind the particles and form alloy [28].

Figure 2.3 shows the ball jar, metal balls, and the inside set-up of the ball mill machine. We first put three big balls of diameter 11 mm and five small balls of diameter 5.5 mm in the ball mill jar with silicon and germanium particles. The balls and jar are made of stainless-steel. Then we seal the jar in the glovebox under argon atmosphere. After we put the ball mill jar in the machine and tighten the holder, we can start the ball milling process. The holder of the jar oscillates during the process, so that the material particles collide with the balls inside the jar. The holder oscillates at a high frequency of $\sim$ 1000 rpm. The high energy during the collision helps break the particles into smaller pieces and finally into nano-size powder.

In order to get Si-Ge powder with good quality, we set the ball milling time to be eight hours. In every two hours, we let the machine stop and wait for 30 minutes. This is to avoid the excess heat that may affect the powder during the ball milling process. The collision between the balls and the inner surface will generate heat and raise the temperature of the ball mill jar. After eight hours ball milling, we can collect the Si-Ge powder and it is ready for sintering.

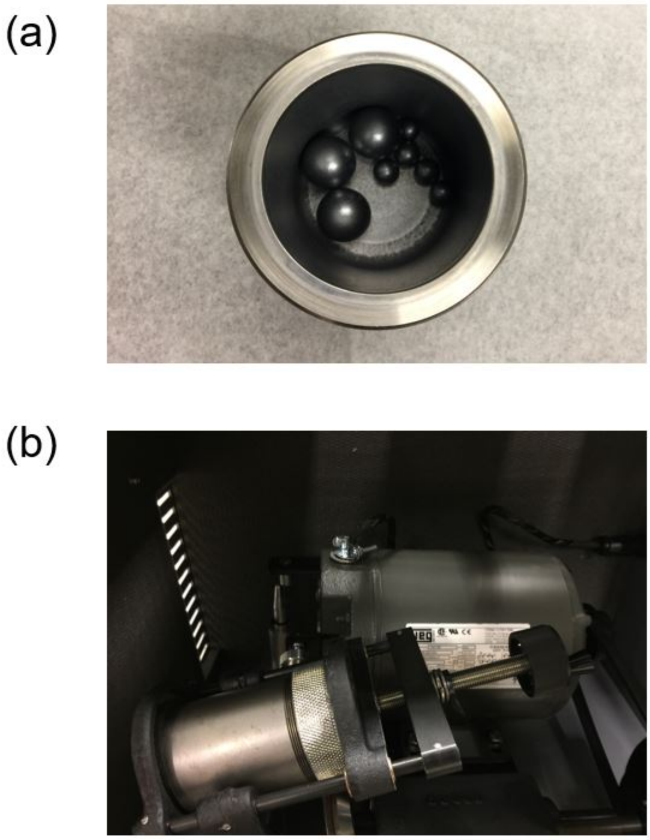

Figure 2.3: (a) Ball mill jar with steel balls inside it (b) Set-up of the jar in the ball mill machine

2.1.2 Inprocess

As we have the alloy powder ready, here comes to the stage that we need to compact the powder into a solid disk. The spark plasma sintering technique is applied to fulfill the task.

Spark plasma sintering system

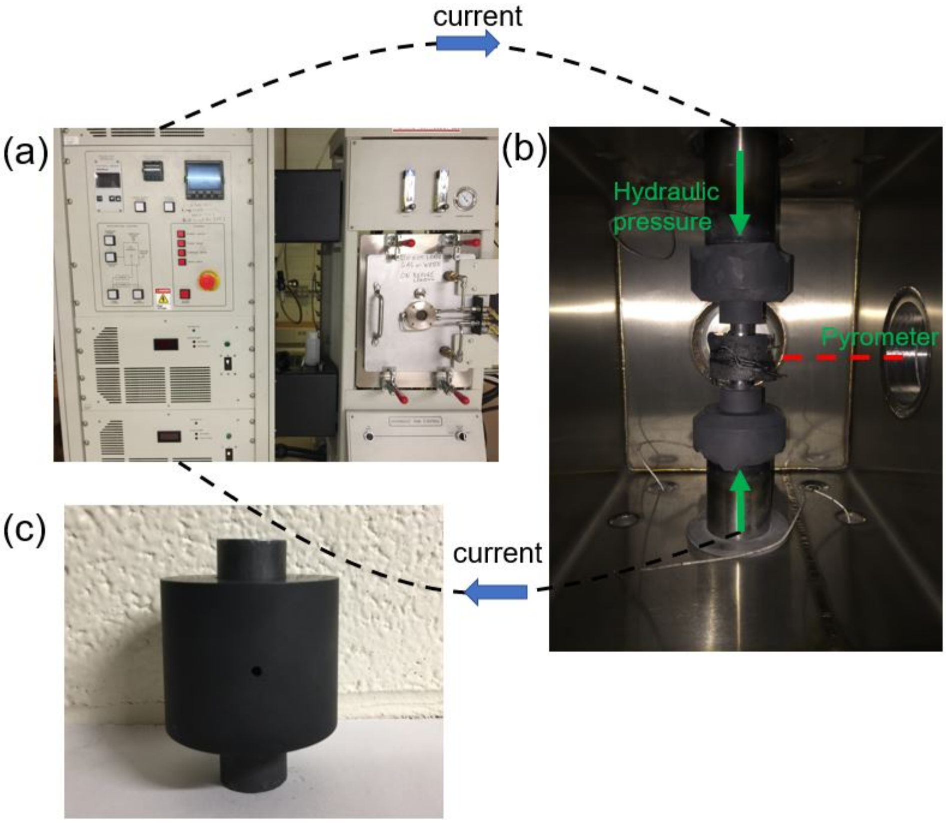

Figure 2.4: (a) The SPS power boxes and the SPS chamber (b) The inner structure of the SPS chamber (c) A typical graphite die with two graphite punches

Spark plasma sintering is a sintering technique with electrical current and mechanical pressure participated in the process [29].

Figure 2.4 (a) shows the SPS power boxes and the external appearance of the SPS chamber. Before the sintering process, we put the alloy powder inside a graphite die (Figure 2.4 (c)) and then place the die in the SPS chamber. The chamber is then vacuumed and backfilled with argon. The graphite die, graphite punches, and the graphite blocks are lined up as shown in Figure 2.4 (b). The mechanical pressure is applied in the vertical direction. During the sintering process, the electrical current goes through the graphite die directly. As the current increases, the temperature inside the die rises. With the help of both the pressure and the heat, the powder inside the die forms bond with each other and finally becomes a solid disk. Compared with conventional hot press technique, SPS heats the sample internally rather than externally. It makes the heating rate to be high and less time to solidify the sample inside the graphite die. Since the time during the SPS process is not long, we have less particle growth during the sintering process which can benefit the mechanical properties [30].

In order to achieve the theoretical density of the alloy, we usually need to set the SPS temperature to be 80% to 90% of the melting points of the alloy. For undoped Bi-Sb alloys, the SPS condition is 240 °C, 50 MPa for 15 mins. For p-type doped Bi-Sb alloys, since the solubility of the dopants Ge, Sn, and Pb is low in the Bi-Sb matrix, we apply a “high pressure low temperature (HPLT)” SPS condition. Together with the melt spinning technique which avoids the diffuse of the dopants during cooling, this special SPS condition can help prevent the precipitates of the dopants during heating and successfully make the dopants stay embedded in the alloy matrix.

The main SPS set-up difference between the Bi-Sb alloy and the Si-Ge alloy is that the Bi-Sb alloy has a low melting point, and we should set low SPS temperature and use the thermocouple to measure the temperature during sintering. While for the Si-Ge alloy which has a higher melting point, we need to set high SPS temperature and use the pyrometer to detect the temperature change of the alloy powder. The melting points and the atomic radii of the main chemical elements used in the experiments are listed in Table 2.1. The atomic radii will be used to help explain the doping efficiency in later chapters.

The detailed SPS conditions for Bi-Sb and Si-Ge are shown in Table 2.2 and Table 2.3. The SPS conditions for Bi-Sb will be mentioned again in Chapter 3.

Chemical element	Melting point	Atomic radius
Bi	271.5 °C	156 pm
Sb	630.63 °C	140 pm
Ge	938.25 °C	122 pm
Sn	231.93 °C	140 pm
Pb	327.46 °C	175 pm
Ni	1455 °C	124 pm
Fe	1538 °C	126 pm
Mn	1246 °C	127 pm
Pt	1768.3 °C	139 pm
Te	449.51 °C	140 pm
Si	1414 °C	111 pm
Mo	2623 °C	139 pm
B	2076 °C	90 pm
P	590 °C	107 pm (covalent radius)

Table 2.1: Melting points and atomic radii of the chemical elements used in the experiments

Bi-Sb	SPS conditions
Trivial SPS	240°C (50 MPa) 15 mins
HPLT	RT (500 MPa) 10 mins, 150°C (50 MPa) 5 mins
Post High-pressure	240°C (50 MPa) 15 mins, RT (500 MPa) 2 hours

Table 2.2: Different SPS conditions for sintering Bi-Sb alloys (HPLT represents 'high pressure low temperature' and RT represents 'room temperature')

	SPS conditions
Si-Ge	900°C (50 MPa) 15 mins, 1050°C (50 MPa) 5 mins
Si-Mo	900°C (50 MPa) 15 mins, 1150°C (50 MPa) 5 mins

Table 2.3: SPS conditions for sintering Si-Ge and Si-Mo alloys

2.1.3 Postprocess

With the help of the spark plasma sintering, we can get a solid alloy disk. But the surface of the disk is covered with a layer of graphite foil which prevents the direct contact between the sample and the graphite punches during the SPS process. We need to cut the disk into a rectangular bar and clean its surface to perform further measurements.

Cutting

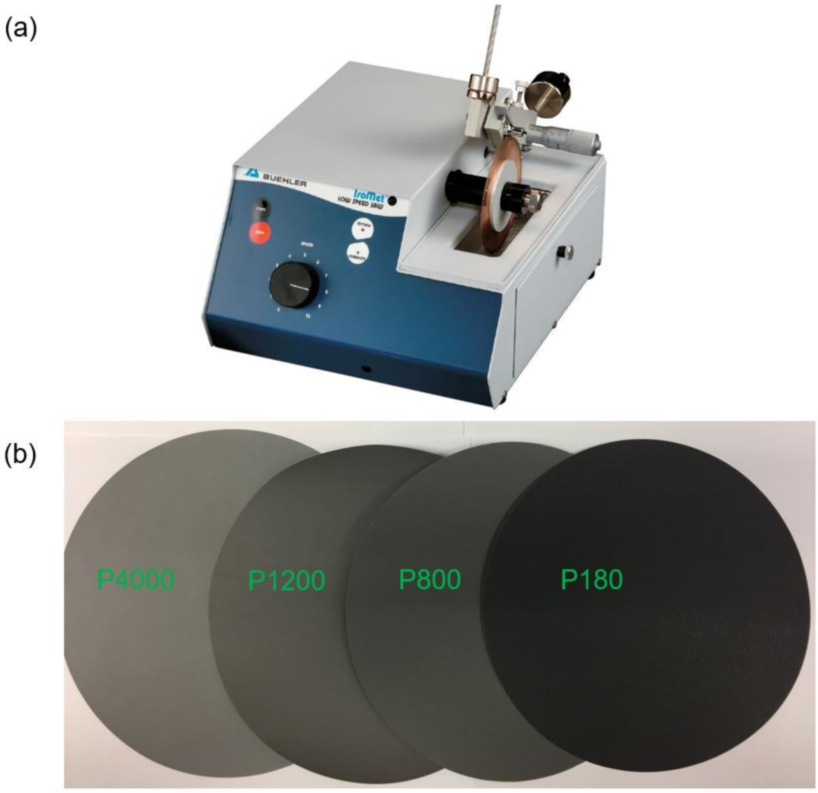

Figure 2.5: (a) The low speed precision sectioning saw (b) The grinding papers with different grit sizes

A low speed precision sectioning saw (Figure 2.5 (a)) is used to cut the samples. First, we stick the sample onto an aluminum or steel bar with the glue. Then we mount the bar on the saw and adjust its position to be cut through. The cutting time depends on the material and the cutting blade that we use. For Bi-Sb, it takes about 20 minutes to finish the cutting and for Si-Ge, it takes about 1 hour. As we finish the two cuts in parallel, we can remove the bar from the diamond saw and put the sample with bar into a beaker with acetone in it. Then we put the beaker into an ultrasonic cleaner and let the oscillation of water and acetone help remove the glue between the sample and the bar and make them separated.

Polishing

After we finish the cutting, we need to polish the surface of the sample to remove the graphite foil and get a metallic shiny surface which is important in characterizing the transport properties later. We select the appropriate SiC sandpapers (Figure 2.5 (b)) and start polishing from using the rough sandpaper (grit size: P180) to smooth sandpaper (grit size: P4000). To prepare for the scanning electron microscope and electron backscatter diffraction, we need to polish the sample further. The polishing cloths and crystalline diamond suspensions are used to polish the surface of the sample.

2.2 Sample characterization methods

As we finish all the synthesis work, we can start to characterize the properties of the samples. The characterization can be separated into two parts: the first part is about the sample phase, the grain topography and the sample composition; the second part is mainly about the transport property measurement.

2.2.1 Single phase and sample homogeneity check

Since different elements and alloys have different X-ray diffraction patterns, it is standard to check the sample phase with the X-ray diffraction method. For the homogeneity of the sample, it will be good if we can find the distribution of different elemental particles on the surface of the sample. The mapping and the line scan function of the energy-dispersive spectroscopy can do the work and we perform the functions on a scanning electron microscope.

X-ray diffraction

We use the PANalyticalX'Pert pro MPD instrument to perform the X-ray diffraction on our samples. Figure 2.6 shows an example of the XRD pattern of the undoped Bi-Sb alloy.

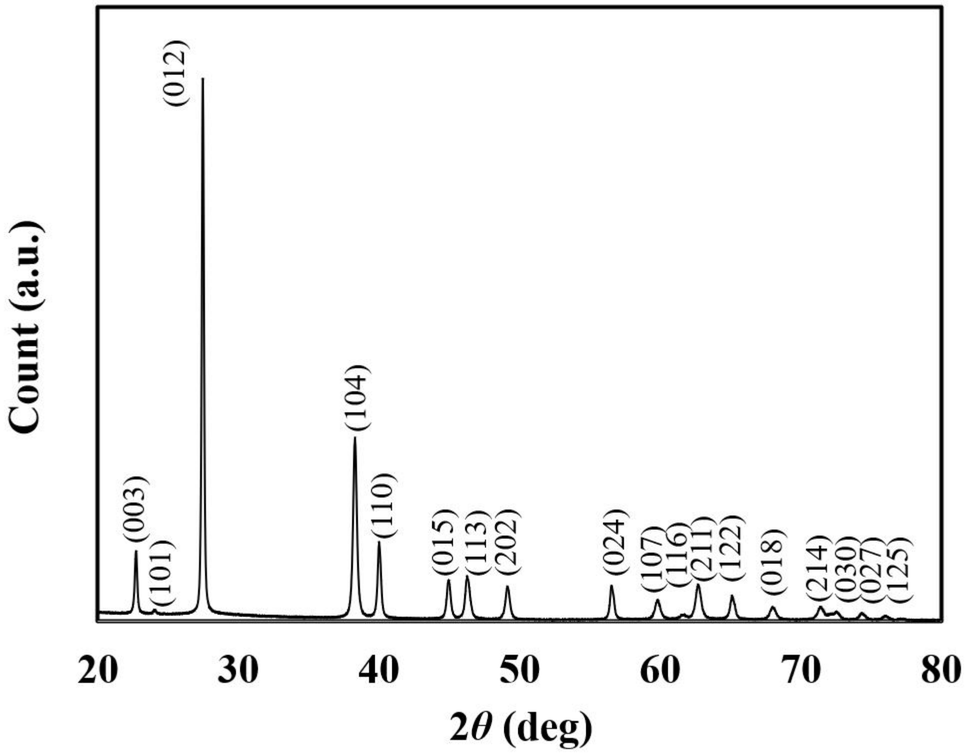

Figure 2.6: The XRD pattern of undoped $Bi_{85}Sb_{15}$

Scanning electron microscope and energy-dispersive spectroscopy

FEI Quanta LV200 and FEI Quanta 650 instrument are used to get the scanning electron microscope (SEM) images and the energy-dispersive spectroscopy (EDS) results. Figure 2.7 and Figure 2.8 show the examples of the SEM surface image and EDS mapping result of the undoped Bi-Sb alloy.

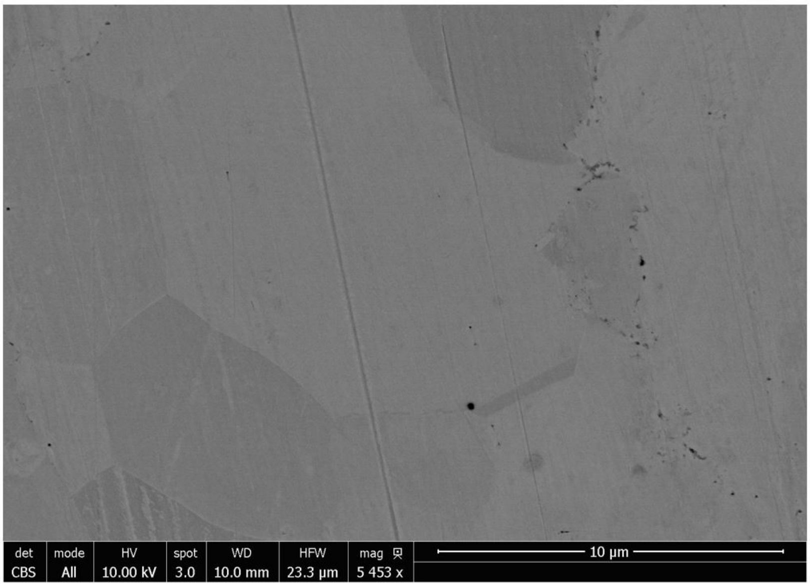

Figure 2.7: The SEM surface image of undoped $Bi_{85}Sb_{15}$

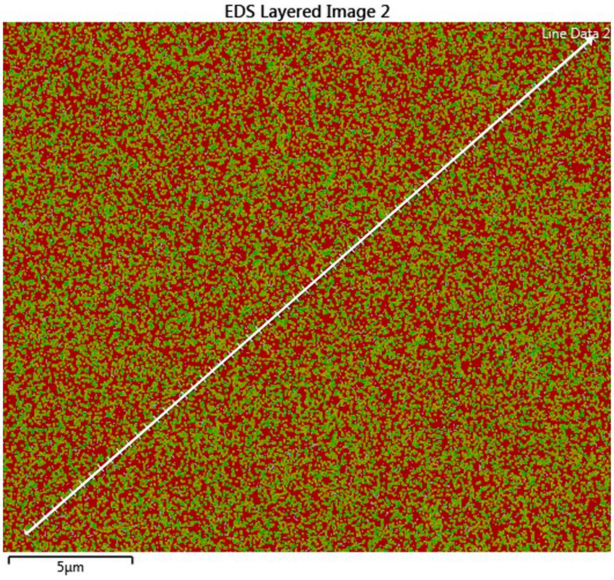

Figure 2.8: The EDS mapping image of undoped $Bi_{85}Sb_{15}$

2.2.2 Transport property measurement

The transport properties include the resistivity, the Seebeck coefficient, the Hall coefficient, and the thermal conductivity.

As we discussed in the section of Seebeck effect, we need to perform the transport property measurement using a four-probe method with 2 potential/temperature probes and 2 current leads. This set-up can avoid the contact effect between the sample and the electrodes. In both the physical properties measurement system (PPMS) and ZEM-3 system, this method takes the place. The low temperature measurements are performed on PPMS for Bi-Sb samples while the high temperature measurements are performed on ZEM-3 for Si-Ge samples. Let's introduce the PPMS first.

Physical properties measurement system

Figure 2.9: The PPMS helium chamber and the operating computers

The Quantum Design physical properties measurement system (PPMS) is an equipment that has lots of measurement options including the electrical transport option (ETO), the vibrating sample magnetometer (VSM), and the thermal

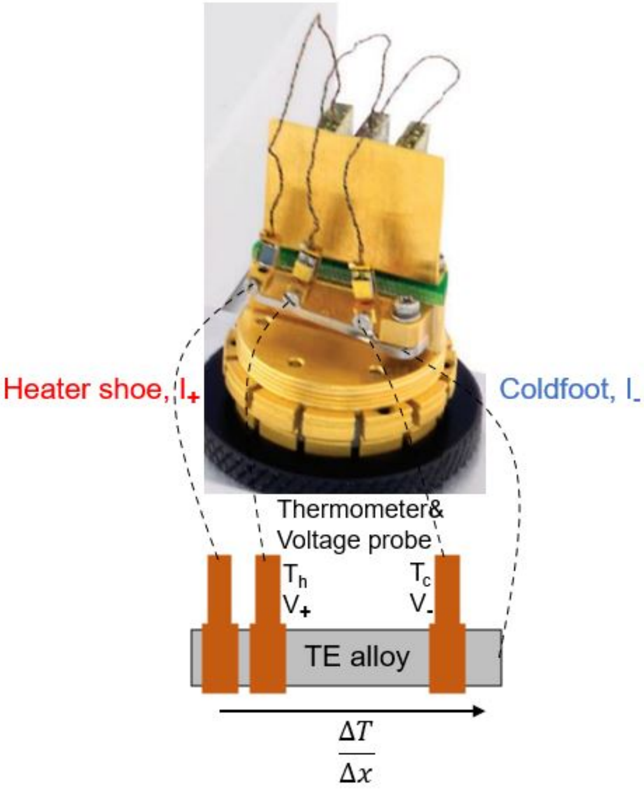

Figure 2.10: The PPMS sample puck and the set-up diagram of the TE alloy on the puck

transport option (TTO). We mainly use the thermal transport option (TTO) to measure the resistivity and the Seebeck coefficient of the sample. The measurement range of temperature is from 1.8 K to 400 K. Figure 2.9 shows the appearance of PPMS.

There is a chamber that we can fill in the liquid helium to decrease the environment temperature during the measurement. The sample is connected on a sample puck using the four-probe method as shown in Figure 2.10 and inserted into a separated space in the chamber. When the measurement goes on, the space where the sample sit in is at high vacuum. A thermal pulse is applied to the sample and the corresponding temperature and voltage signals are recorded [31]. The Seebeck coefficient would be calculated automatically using algorithms developed for the thermal circuit. After the thermal measurement starts at one temperature point, the resistivity measurement goes on immediately at the same temperature point.

Versalab system and Hall coefficient measurement

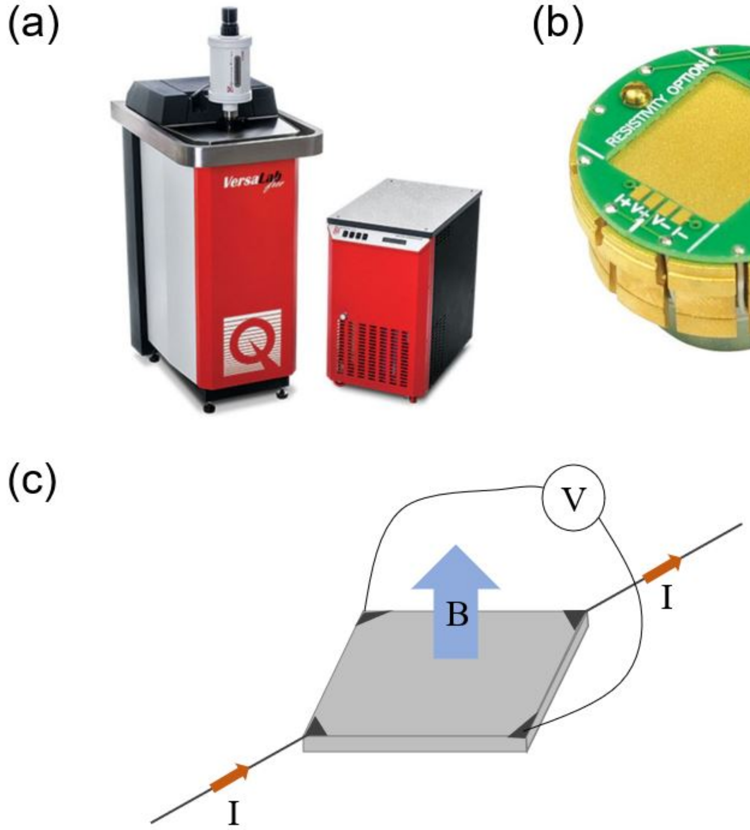

Figure 2.11: (a) The Versalab machine (b) The resistivity and the Hall coefficient sample puck (c) The Van der Pauw method of measuring the Hall coefficient

Versalab is also an equipment made by Quantum Design (Figure 2.11 (a)). It is similar to PPMS. The difference is that Versalab is more portable, and easy to move compared to PPMS. Besides, the lower bound of temperature in the measurement is 50 K for Versalab and we do not need to fill the liquid helium for Versalab since a helium compressor can recycle the helium there. Here we use Versalab mainly for the Hall coefficient measurement.

The Hall effect is well known. When an electrical current goes along the length direction of a sample and the magnetic field is perpendicular to the $width * length$ plane, the path of the charge carriers becomes curved because of the magnetic force. An electric field will be built along the width direction. At the steady state, the electric field becomes strong enough to balance the magnetic force.

By measuring the Hall voltage V_H and the thickness of the sample t, we can calculate the Hall coefficient using the following formula:

$$R_H = \frac{V_H t}{IB} \tag{2.1}$$

where I is the electrical current and B is the magnetic field.

The single channel Hall coefficient R_H can be written as:

$$R_H = \frac{1}{ne} \tag{2.2}$$

where n is the carrier concentration and e is the unit charge. With the Hall coefficient, we can calculate the carrier concentration in the alloy.

To perform the Hall coefficient measurement, we follow the Van der Pauw method [32]. We need to prepare the sample to be a thin square shape plate (∼0.25 mm). Then we put it on a sample puck (Figure 2.11 (b)) and connect four leads onto it (Figure 2.11 (c)). The two current leads are set at the two diagonal corners and the two voltage leads are set at the two antidiagonal corners. The direction of the magnetic field is perpendicular to the plane of the sample plate during the measurement.

ZEM-3 system

ZEM-3 (Figure 2.12 (a)) is designed and produced by the ULVAC company. It can be used to measure the resistivity and the Seebeck coefficient of samples at high temperature. The upper bound for the temperature is 1000 °C.

As we have a good rectangular cuboid, we need to measure the width and depth of the sample. The requirements for the dimensions of the sample are: it should be 2 to 4 mm square (width and depth) or diameter and 5 to 22 mm in length.

Then we mount the sample on the stage following the four-probe method as shown in Figure 2.12 (b). We let the two ends of the sample connecting to the upper and lower electrodes on the sample stage and two probe thermocouples

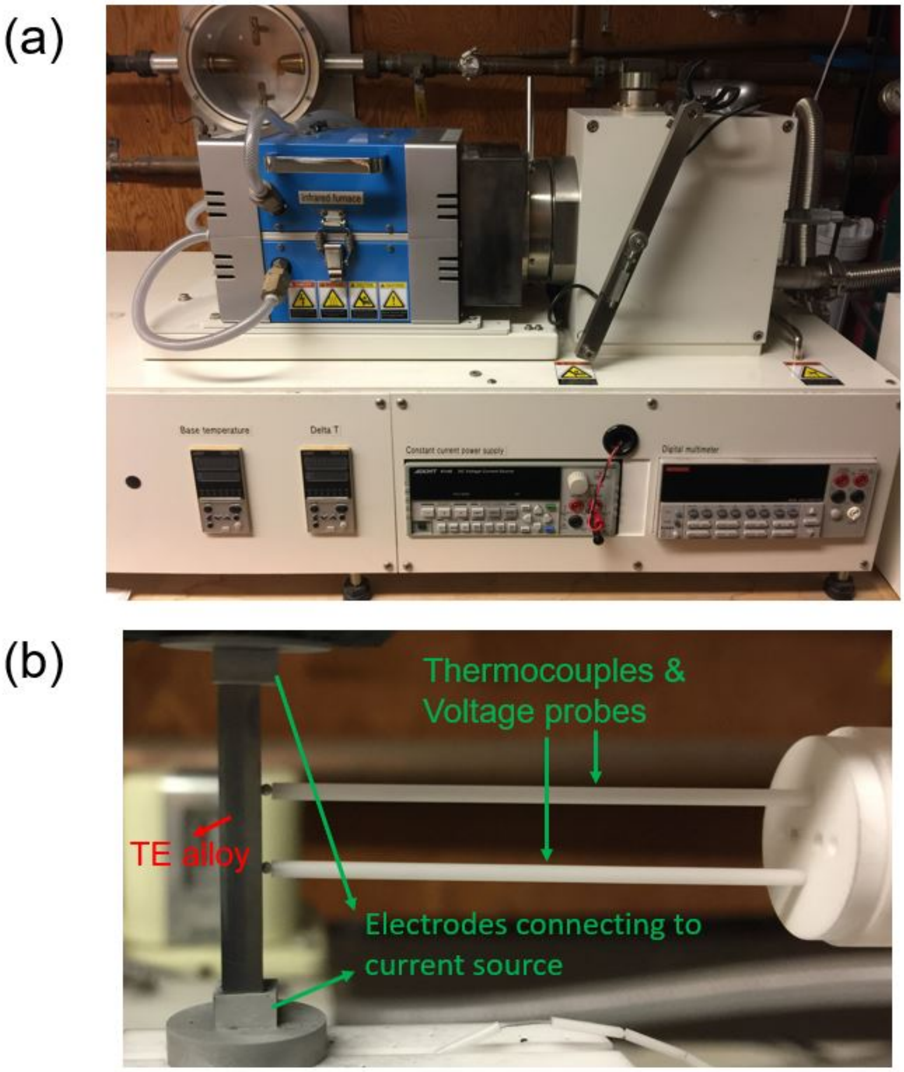

Figure 2.12: (a) The ZEM-3 machine (b) The set-up of the sample and the thermocouples on ZEM-3

connecting at the middle part of the side face on the sample. We want to avoid the direct contact between the sample and the electrodes, and the thermocouples. So, small graphite pieces will be put between the sample and the electrodes, also the probe thermocouples in the real measurement. We then vacuum the chamber and backfill the helium gas into the chamber. The measurement is performed under the low pressure helium atmosphere.

If the set-up is correct, we should get a linear V-I plot showing the ohmic feature of the sample as we turn on the machine and start the program.

Hot disk method

We have used the hot disk method (also known as the transient plane source technique) to measure the thermal conductivity of the Bi-Sb samples [18]. Two identical SPSed disk samples are used in the measurement. The liquid nitrogen works as the cold stage and the heat source inside a sensor is set between the two samples. Compared to other thermal conductivity measurement methods, the main advantage of the hot disk method is that it measures the absolute value of the thermal conductivity. We don't need to know the thermal diffusivity and the heat capacity of the material to calculate the thermal conductivity in the hot disk method.

Chapter 3

P-type doping effects in Bi-Sb alloys

The background information about Bi-Sb alloys and the related research are introduced in this chapter. After that, we start to discuss the experimental results of our p-type doped Bi-Sb. The X-ray diffraction (XRD) patterns and the scanning electron microscope (SEM) images of the Bi-Sb samples are presented. The transport properties of Ge, Sn, and Pb doped Bi-Sb are measured. We develop a "high pressure low temperature (HPLT)" sintering method to effectively increase the doping level of Ge and doping efficiency of Pb in Bi-Sb. The Hall coefficient and the doping efficiency are discussed with the idea of substitutional acceptors and interstitial donors [33]. Besides, several strategies to enhance the thermoelectric (TE) properties of p-type Bi-Sb are discussed in later sections. Finally, we compare the power factor of the samples made using different strategies. With the thermal conductivities measured using hot disk method, we calculate the figure of merit zT and compare the values with referenced p-type Bi-Sb results. The sample with the composition $Bi_{88}Sb_{12}Ni_1Pb_{0.5}$ is found to have the highest zT ($\sim$ 0.13 peaks at 200 K) in the temperature range 130 K $\sim$ 210 K.

3.1 Background information about Bi-Sb alloys

The TE properties of Bi-Sb have been studied for more than 60 years [34]–[37]. Researchers have studied samples' transport behaviors with and without magnetic field. The strong magneto TE effects have been discovered in this system [36], [38]. For six decades, the figure of merit zT of this system has little enhancement. Yet it is still the best n-type TE material at cryogenic temperature (below 150 K). This system not only has decent TE performance, but also possesses very interesting electronic properties. It is discovered to be a topological insulator [39]. At certain composition, the resistivity of this system rises fast as temperature decreases which shows a strong semiconducting behavior. Yet pure bismuth and pure antimony are semi-metals in which the conduction band overlaps with the valence band. But as we put those two elements together, the relative positions of the bands shift as the alloy composition changes and that leads to a transition from semi-metal to semiconductor. The details will be discussed in the following sections.

3.1.1 Structure and electronic band properties

Bismuth and antimony both have the rhombohedral crystal structure. Their lattice parameters are similar to each other which makes it possible for them to mix into a solid solution no matter what the alloy composition is [40]. Bismuth and antimony are both semi-metals in which the valence band is overlapped with the conduction band. The valence band and the conduction band of bismuth are labeled as the T hole band and L_s electron band. The valence band and the conduction band of antimony are labeled as the H hole band and L_a electron band. The bands parameters are listed in Table 3.1.

These parameters are useful when modelling the transport properties of our p-type doped Bi-Sb samples. As we can see that the effective mass of the L_s electron band is very small, which leads to a high electron mobility in bismuth

Carriers	$m_{1'}$ (m_e)	$m_{2'}$ (m_e)	$m_{3'}$ (m_e)	N_V
Bismuth				
L_s	0.00119	0.266	0.00228	3
T	0.064	0.064	0.69	1
Antimony				
L_a	0.0093	1.14	0.088	3
H	0.068	0.92	0.050	6

Table 3.1: Band parameters for Bi and Sb at 4.2 K [41]

element and Bi-Sb alloy.

The band structure of the alloy shows a very interesting behavior when we change the alloy compositions. Figure 3.1 shows the variation of the bands in Bi-Sb alloys. Let's start from the bismuth side and see what happens after we keep adding antimony into the system.

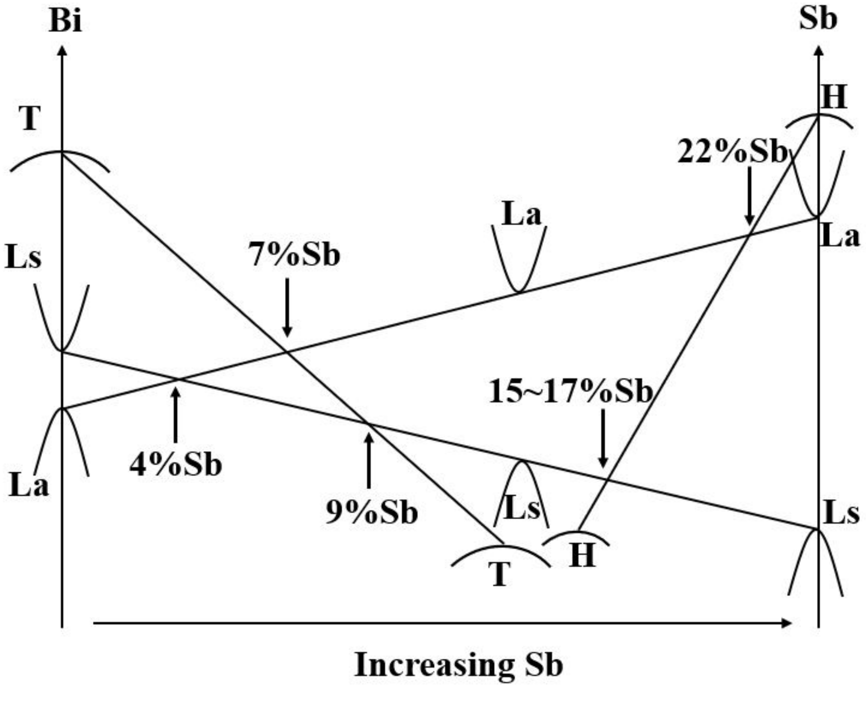

Figure 3.1: Band diagram of Bi-Sb as changing the alloy compositions [37], [42]

For the alloy composition $Bi_{1-x}Sb_x$, when x is less than 0.04, the alloy behaves similarly to bismuth with a smaller overlap between the T hole band and the L_s electron band. At $x \approx 0.04$, the L_s electron band and the L_a electron band are inverted. When x increases to 0.07, the T hole band is no longer overlapped with the electron band and the alloy transforms from a semi-metal into a semiconductor. This feature continues until x reaches to 0.22. At that point, the H hole band rises to the top of the electron band and the overlapping between the valence band and the conduction band is back. The alloy turns back to be semi-metallic and this feature continues as we increase x towards 1 which represents the pure antimony state. To summarize the key point, the $Bi_{1-x}Sb_x$ alloy becomes to a narrow gap (less than 30 meV) semiconductor when x is in the range $0.07 < x < 0.22$. The maximum band gap happens in the range $0.15 < x < 0.17$.

3.1.2 Previous TE research on Bi-Sb alloys

In this section, we review the synthesis method and the previous research on n-type and p-type Bi-Sb alloys. This leads to the path to our own study on p-type doping effects in Bi-Sb.

Synthesis of single crystal and polycrystalline Bi-Sb

In considering synthesizing the Bi-Sb alloys, one of the most important things is to avoid the segregation effect. People have applied many methods, such as the single pass zone-leveling technique [36], the traveling heater method [42], and the Bridgeman technique [43] to grow single crystals for Bi-Sb. The low growth rate of the single crystal is helpful to get homogeneous samples. Compared with the single crystal, polycrystalline samples have better mechanical properties. It is safer to deal with polycrystalline samples since there is a less chance to break them during the experiments. The powder metallurgy has been applied to produce polycrystalline Bi-Sb samples. People utilize the mechanical alloy method, such as the ball milling [44], to break the bismuth particle and antimony particle into powder and mix them together. With the help of hot press, polycrystalline Bi-Sb sample can be successfully produced. Here we have used the melt spinning technique and the spark plasma sintering method to produce the Bi-Sb alloys and the details are shown in Chapter 2. It tends out to be a clean way to get the alloy powder for synthesizing the polycrystalline Bi-Sb samples.

N-type Bi-Sb related research

Many studies have been done on single crystal Bi-Sb alloys [34], [36]–[38], [45]–[47]. Undoped Bi-Sb alloy is n-type in which the electron channel dominates the transport properties. Here we take Yim and Amith's results [36] as the reference point as they showed comprehensive data of transport properties along the two crystalline directions of undoped Bi-Sb. One is parallel to the triagonal axis in the crystal structure and the other one is in the perpendicular plane to the triagonal axis. The figure of merit zT measured in parallel to the triagonal axis is about 0.55 while in the perpendicular plane is 0.4.

Our group has studied the polycrystalline undoped Bi-Sb [18]. We find that compared with the single crystal sample, the polycrystalline sample shows higher resistivity and higher Seebeck coefficient. The single crystal sample has a higher power factor below 200 K due to its lower resistivity. However, with the help of the melt spinning and the spark plasma sintering, we make the sample with fine grains of micron size and that leads to a stronger grain boundary scattering which significantly decreases the thermal conductivity. As a result, the polycrystalline sample benefits from the lower thermal conductivity and reaches a zT peak near 0.6 in the temperature range 100 K $\sim$ 150 K.

P-type Bi-Sb related research

Bismuth and antimony are group 15 elements and they have 5 valence electrons. Ge, Sn, and Pb are group 14 elements and it turns out that they work as acceptors in Bi-Sb matrix. After adding Ge/Sn/Pb into Bi-Sb alloy, the alloy transforms from n-type to p-type. The Seebeck coefficient and the Hall coefficient change the sign as temperature rises. Let's see what has been done on Ge/Sn/Pb doped Bi-Sb in previous studies.

Polycrystalline $Bi_{85}Sb_{15-x}Ge_x$ (x = 0, 0.5, 1, 1.5, 2) samples are made and characterized in the work [44]. As the Ge content increases, the range of the positive Seebeck coefficient increases. The alloy composition $Bi_{85}Sb_{13}Ge_2$ shows maximum zT of 0.07 at 140 K. The Hall coefficient is positive below 200 K in $Bi_{85}Sb_{13}Ge_2$. The segregation of Ge is pointed out by the authors since the carrier concentration of the $Bi_{85}Sb_{13.5}Ge_{1.5}$ sample is very close to that of $Bi_{85}Sb_{13}Ge_2$ sample.

For Sn doped Bi-Sb, researches have been done for both the single crystal and polycrystalline samples. In the work [43], people vary the Sb content from 12 at% to 37 at% in single crystal samples and 50 at% to 90 at% in polycrystalline samples. The doped Sn content is kept at 0.75 at%. By varying the Sb content, the relative positions of the bands change. The T hole band, H hole band and the L_s hole band all have a chance to contribute to the transport depending on the alloy compositions. They report that the multiple valence bands are doped and contribute to the transport to help enhance the zT to 0.13 at 240 K for a sample with 22.9 at% Sb.

In another Sn doped Bi-Sb work [48], researchers keep the Sn content less than 5 at% and vary the Sb content in the range 7∼10 at% and 18∼20 at% as those are the extreme regions to show the semiconducting behavior. They find that Sn largely decreases the thermal conductivity (from $\sim 5\,WK^{-1}m^{-1}$ to $\sim 3\,WK^{-1}m^{-1}$ in the temperature range 100 $\sim$ 200 K) of the alloy and that leads to a zT peak of 0.08 at 200 K for the sample $Bi_{88.5}Sb_{7.5}Sn_4$.

$(Bi_{88}Sb_{12})_{100-x}M_x$ ($M = Pb,\ Sn$; $x = 0.005 \sim 3$) alloys are studied in the work [49]. All doped samples show positive Seebeck coefficient when temperature is below 150 K. The segregation of Pb and Sn in the samples are observed at high Pb/Sn doping levels.

In the work [50], $Bi_{85}Sb_{15-x}Pb_x$ ($x = 0,\ 0.5,\ 1,\ 2,\ 3$) samples are made using the ball milling and SPS method. An impurity phase Pb_7Bi_3 is found in the samples when $x > 1$. The optimum zT value of 0.12 is found in the sample $Bi_{85}Sb_{14}Pb_1$ at 190 K.

As we can see from the previous studies, people have tried to put Ge, Sn, and Pb into Bi-Sb system. However, the solubility of those elements in Bi-Sb is quite low. Segregation happens at high doping levels. It's important to find a way to avoid the segregation effect and improve the doping efficiency of the dopants in the system. Here we have applied the “high pressure low temperature (HPLT)” method to input more dopants into the alloy system without much segregation and studied the doped alloys' transport properties.

3.2 X-ray diffraction and scanning electron microscope results

We have measured the X-ray diffraction patterns of the Ge, Sn and Pb doped samples. The results are shown in Figure 3.2. It shows the XRD patterns of undoped $Bi_{85}Sb_{15}$, Ge doped $Bi_{85}Sb_{15}Ge_x$ ($x = 5$, 10, 15), Pb-doped $Bi_{85}Sb_{15}Pb_{0.5}$, and Sn doped $Bi_{85}Sb_{15}Sn_x(x = 0.5, 5)$ samples. The Ge and Pb doped samples are made using the HPLT method while the Sn samples are made with the trivial SPS condition. The SPS conditions are shown in Table 2.2. We have compared the XRD patterns of those samples with the patterns of pure Ge/Sn/Pb and the binary alloys composed of Bi/Sb and Ge/Sn/Pb. Second phase is not detected in the samples except for $Bi_{85}Sb_{15}Sn_5$. Three extra peaks can be observed in the XRD pattern of $Bi_{85}Sb_{15}Sn_5$ and they are corresponding to the phase of Sn-Sb alloy [51]. The blue triangles point to the positions where three main peaks of the Sn-Sb phase locate. It is worth noting that the patterns of the high amount Ge samples (Ge5, Ge10, and Ge15) are clean. We do not find any signal for precipitated Ge in those samples.

We have performed SEM and EDS to study the grain size and the homogeneity of the Bi-Sb samples. Here we can see the SEM images of the well-polished surface of Bi-Sb alloy in Figure 3.3. (a)(b)(c)(d) are the different spots on the surface. They all show clear grain boundaries and the grain size is several microns on average.

Figure 3.4 are the electron backscatter diffraction (EBSD) images. The

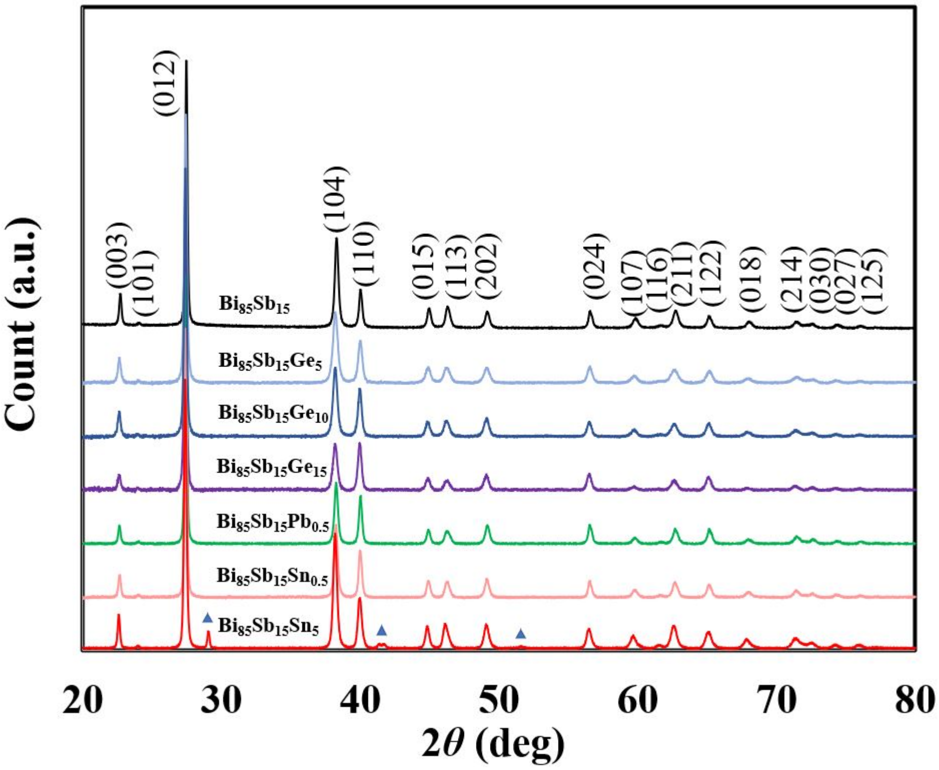

Figure 3.2: XRD patterns of Ge, Sn, and Pb doped Bi-Sb

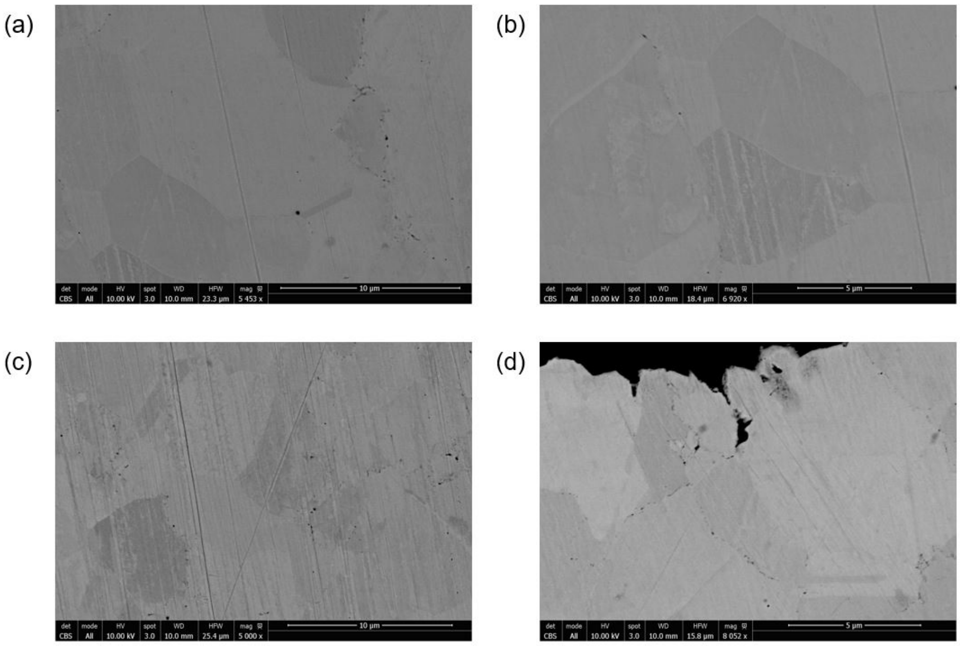

Figure 3.3: SEM images showing the grains on the surface of undoped Bi-Sb

different color shows the grains with different crystal orientations. (a)(b) are two different spots on the sample surface. The black dots and lines are the polishing scratches on the sample.

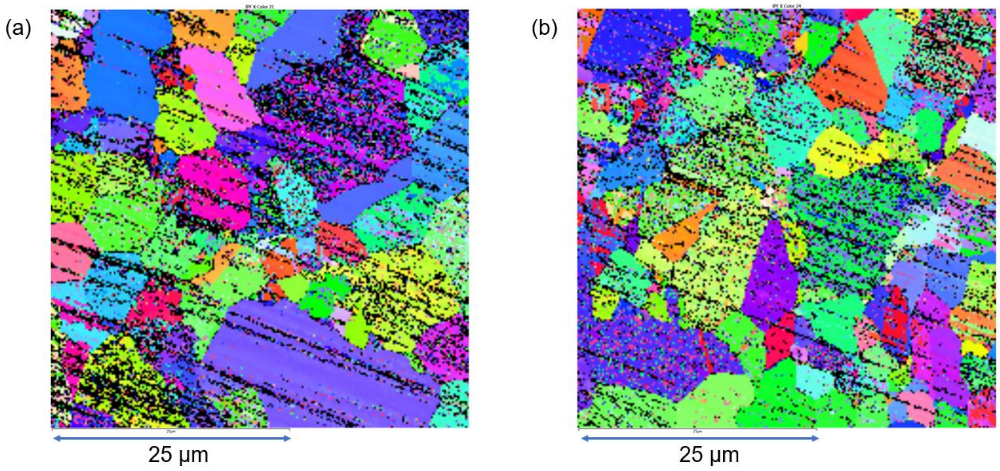

Figure 3.4: Electron backscatter diffraction (EBSD) images of undoped Bi-Sb

Figure 3.5 are the SEM images of the sample's cross section. Again, we can see the grains of micron size in the image.

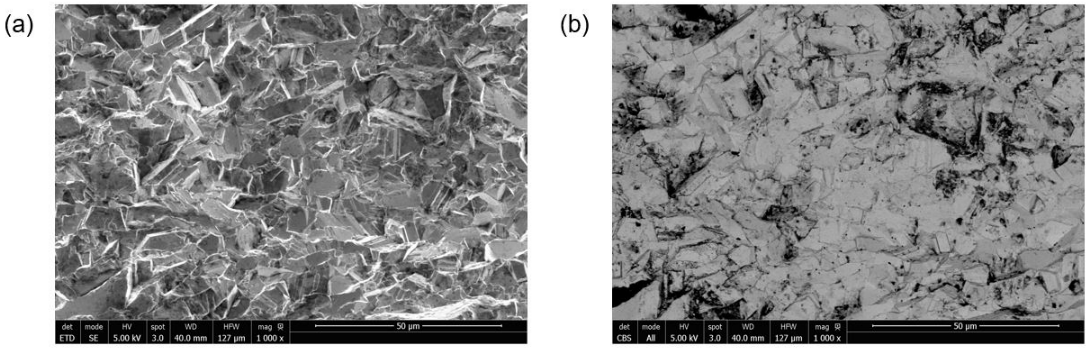

Figure 3.5: SEM images of the cross section of undoped Bi-Sb

We have compared the homogeneity of the as-cast ingot and the sample made using the melt spinning (MS) + the spark plasmon sintering (SPS). The mapping and line scan results (Figure 3.6 and Figure 3.7) clearly show that the MS+SPS sample is much more homogeneous than the as-cast ingot. The average fluctuation of the particles' distribution is within 3 at%.

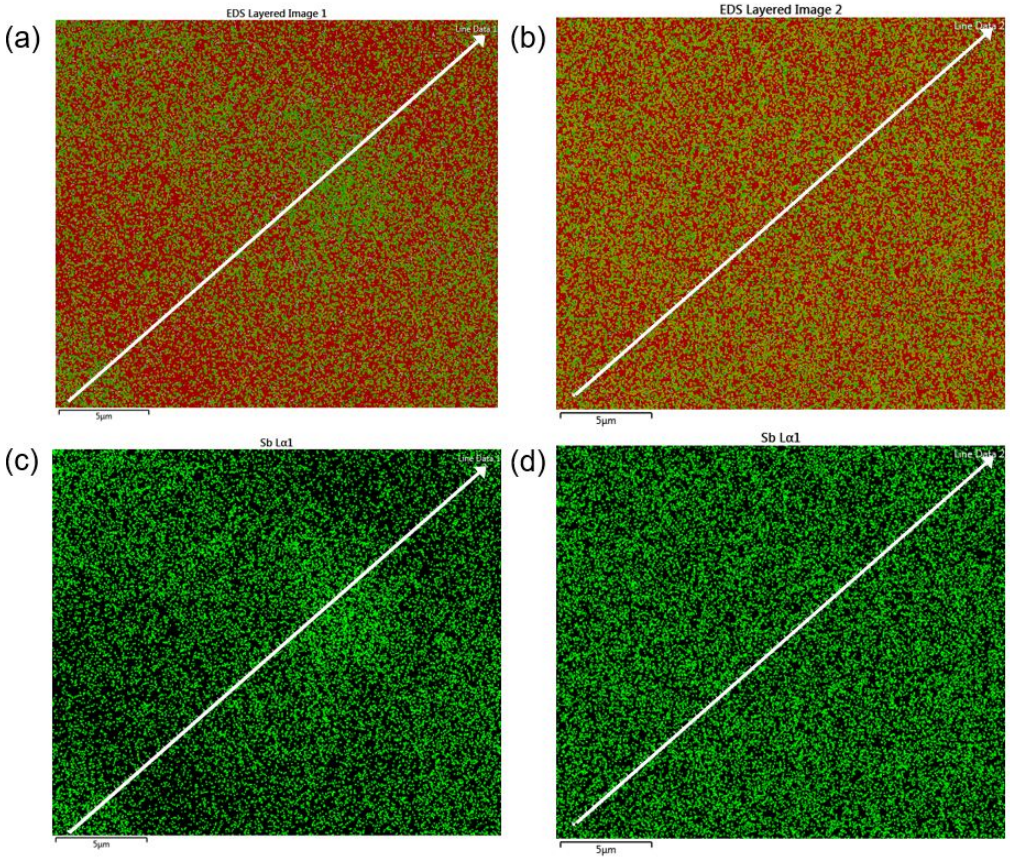

Figure 3.6: EDS mapping: (a) showing the distribution of Bi and Sb in the as-cast ingot; (b) showing the distribution of Bi and Sb in the MS+SPS disk; (c) showing the distribution of Sb in the as-cast ingot; (d) showing the distribution of Sb in the MS+SPS disk

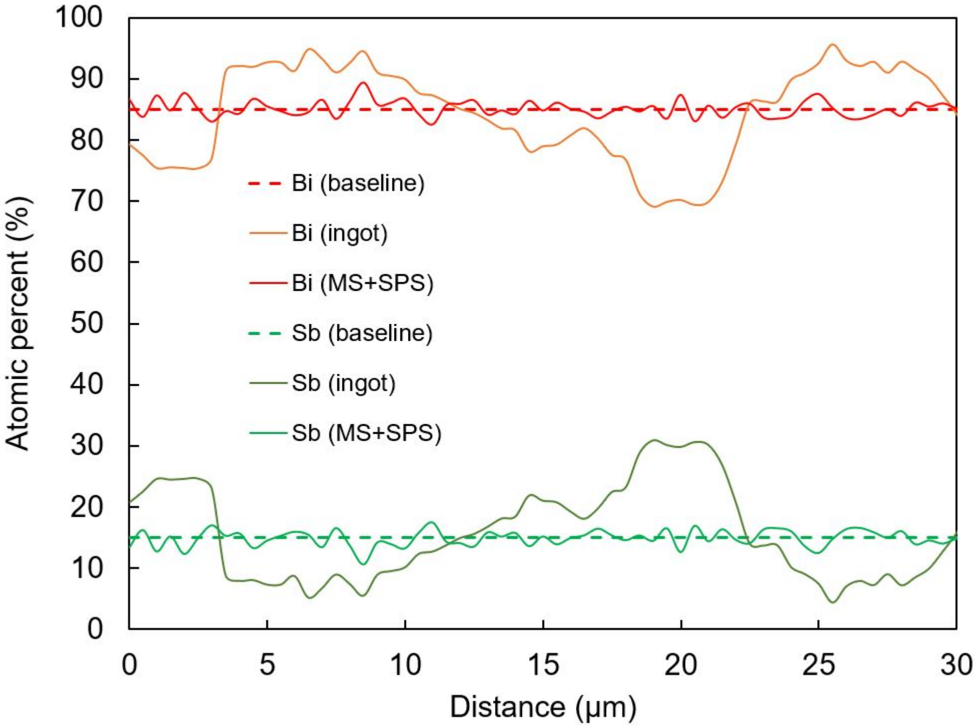

Figure 3.7: The EDS line scan results of the as-cast Bi-Sb ingot and the MS+SPS Bi-Sb disk

3.3 Resistivity, Seebeck coefficient, and Hall coefficient results of pure Ge, Sn, and Pb doped Bi-Sb

To set the benchmark, we have studied the transport properties of pure Ge, Sn, and Pb doped Bi-Sb ($Bi_{85}Sb_{15}(Ge, Sn, Pb)_x$) first. The solubilities of Sn, Pb and Ge in Bi-Sb alloy are known to range from ~ 3 to ~ 0.5 to zero atomic percent, respectively. With the help of the melt spinning technique and the spark plasma sintering, we can successfully dope Ge, Sn, and Pb into Bi-Sb. Furthermore, we apply the "high pressure low temperature (HPLT)" method to increase the doping level of Ge and doping efficiency of Pb in Bi-Sb.

3.3.1 Ge doped Bi-Sb

Among Ge, Sn, and Pb, Ge has the lowest solubility (∼0 at%) in Bi-Sb. The resistivity and the Seebeck results of the samples made using the trivial SPS condition and the HPLT method are shown in Figure 3.8 and Figure 3.9. It can be seen that after increasing the Ge content up to Ge2, the resistivity and the Seebeck of the trivial Ge doped samples don't change much if we keep adding more Ge into the system. The Ge particles are saturated in the alloy and the doping level is capped to a certain extent. The resistivities of those samples are relatively high. After we apply the HPLT method, we can see that the resistivities drop significantly by comparing the results of Ge0.1 & Ge0.1 (HPLT), and Ge2 & Ge2 (HPLT) samples. This indicates an increase of the carrier concentration in the alloy and we will discuss about it in detail in the section of the Hall coefficient.

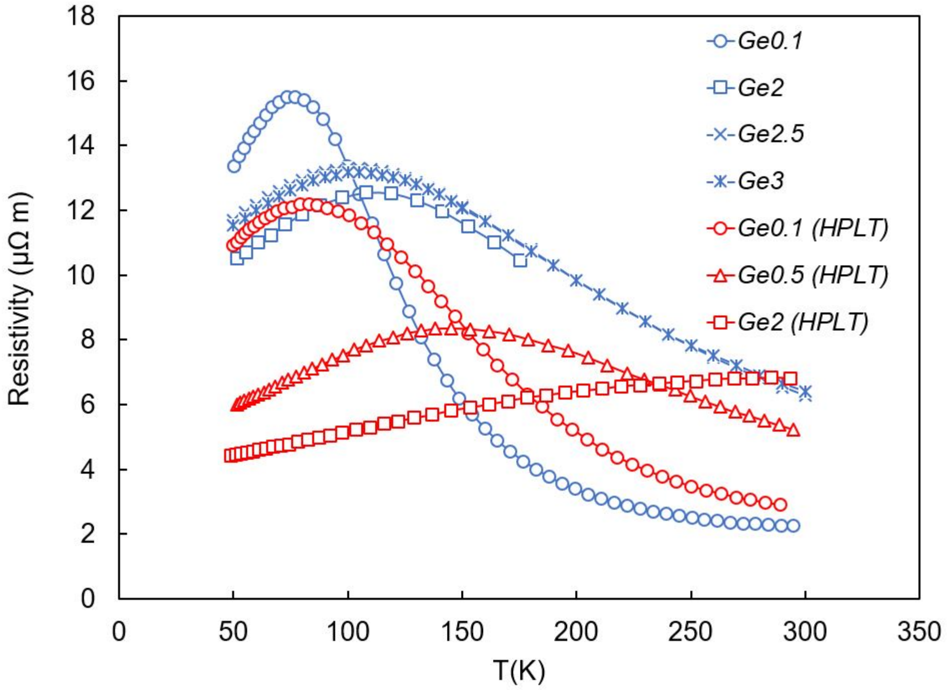

Figure 3.8: Resistivity of Ge doped $Bi_{85}Sb_{15}$ samples

In the resistivity graph and the Seebeck graph, we can consistently find the turning point feature for all the samples. This is because the band gap of Bi-Sb system is very small (10 ∼ 24 meV [34], [37], [42], [52]) and the electron

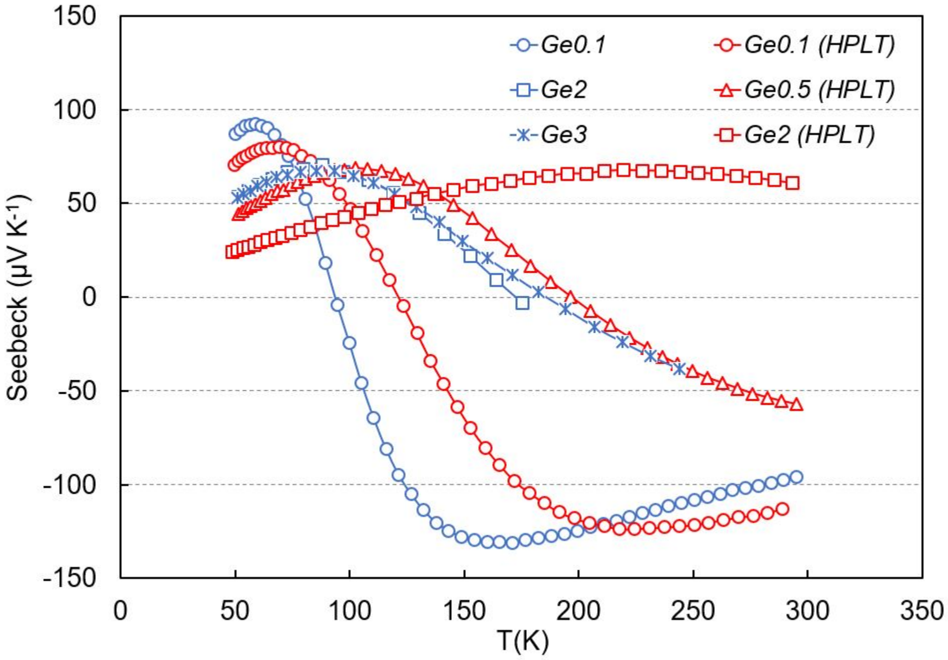

Figure 3.9: Seebeck of Ge doped $Bi_{85}Sb_{15}$ samples

mobility of this system is relatively high [40]. With such a small band gap and high electron mobility, the electron channel is easily excited as the temperature rises and contributes to the transport. This leads to the decrease of the resistivity and the Seebeck at relatively low temperature. So, the turning point (peak) on the resistivity and the Seebeck curves appears. Moreover, as we increase the Ge content, the peak of the resistivity and the Seebeck shifts to higher temperature and the positive Seebeck range broadens.

Next, we input more Ge into Bi-Sb using the HPLT method and see if Ge would be saturated in the matrix in this case. The resistivity and the Seebeck results are shown in Figure 3.10 and Figure 3.11.

Interestingly, the resistivity and the Seebeck become larger as we keep increasing the Ge content. The resistivity and the Seebeck curves tend to be more metallic. They increase linearly in a broad temperature range until the electron channel becomes strong enough to curl the curve. The Ge particles are not saturated. The resistivity increases at first from Ge5 to Ge2, and then decreases a little from Ge5 to Ge10, finally increases again from Ge10 to Ge15. The increasing and decreasing of the resistivity are determined by how adding Ge would affect

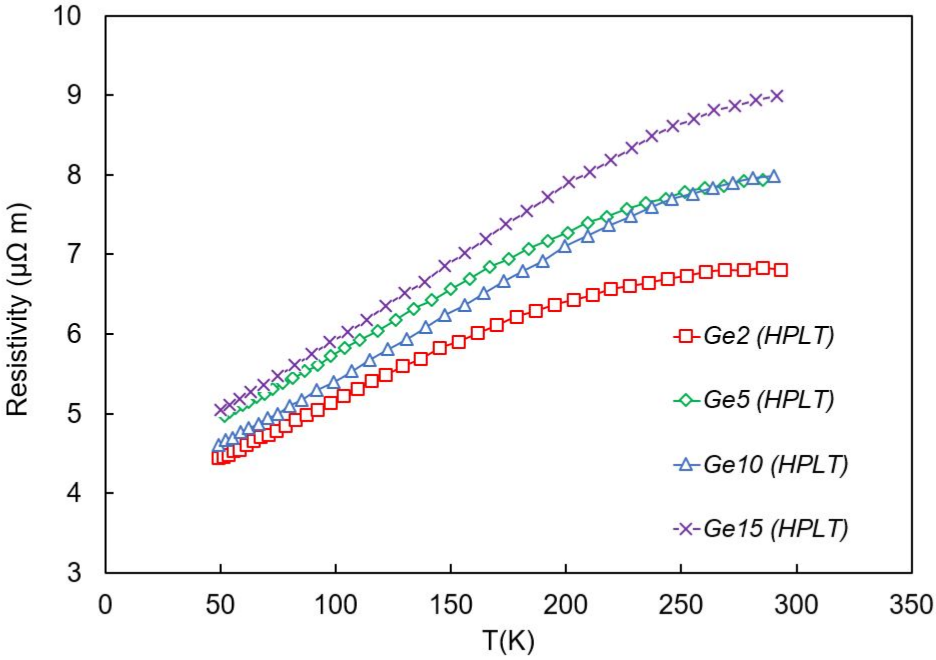

Figure 3.10: Resistivity of $Bi_{85}Sb_{15}$ samples doped with high content of Ge (2∼15)

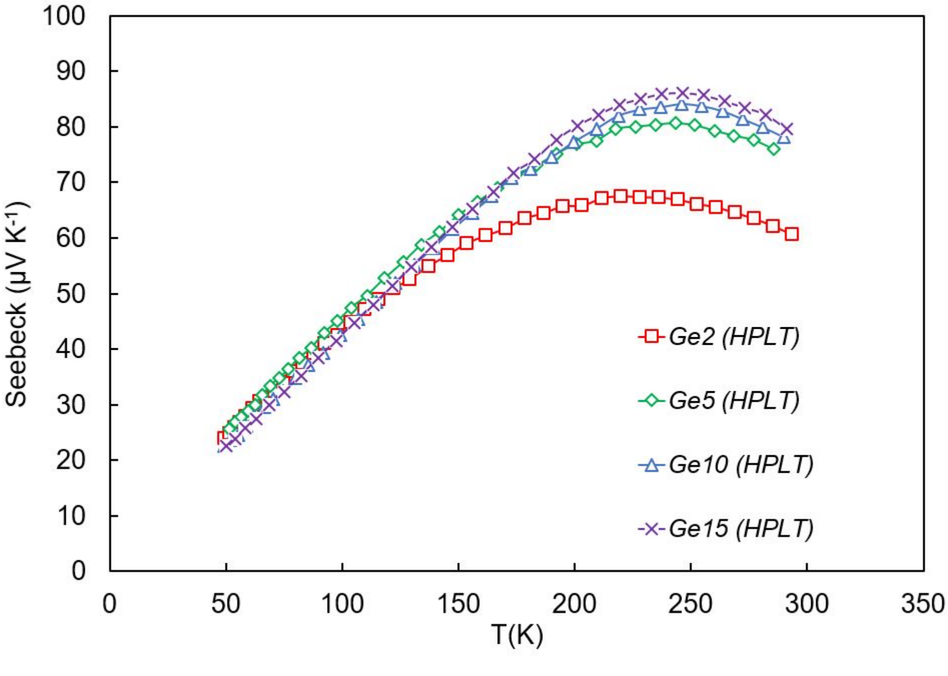

Figure 3.11: Seebeck of $Bi_{85}Sb_{15}$ samples doped with high content of Ge (2∼15)

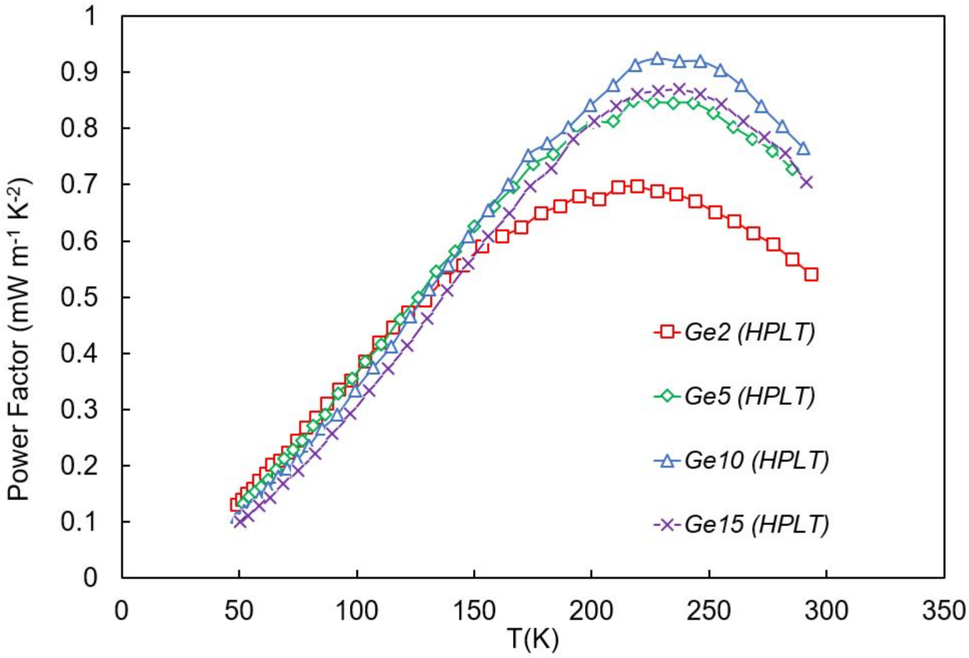

Figure 3.12: Power factor of $Bi_{85}Sb_{15}$ samples doped with high content of Ge (2∼15)

the carrier mobility and carrier concentration in the samples. If it decreases more of the mobility, then resistivity increases. If it increases more of the carrier concentration, then resistivity decreases. The Seebeck curve shows a more continuous change with respect to the Ge content. As we keep adding more Ge into the system, the Seebeck peak rises. We calculate the power factor of those samples, the results are shown in Figure 3.12. We can find that Ge10 sample has the highest power factor above 150 K. Its peak value is $0.92\, mWm^{-1}K^{-2}$ at around 230 K.

We use the SEM and EDS to study the Ge distribution in Bi-Sb samples doped with high content of Ge. Figure 3.13 shows the EDS spectrum result of the Ge10 sample. Spectrum 5 shows the atomic ratios (%) of Bi, Sb, and Ge are (77.3, 14.0, 8.7). Spectrum 6 shows the ratios as (77.9, 13.1, 9.1). Those values are close to the expected value (77.3, 13.6, 9.1).

Figure 3.14 shows the EDS mapping results of the Ge15 sample. We don't see any obvious nonuniform distribution of Ge particles. Ge atoms are distributed homogeneously in Bi-Sb solid solution in micro-scale based on the uniform density of bright blue dots shown in the EDS mapping and the respective atomic ratios

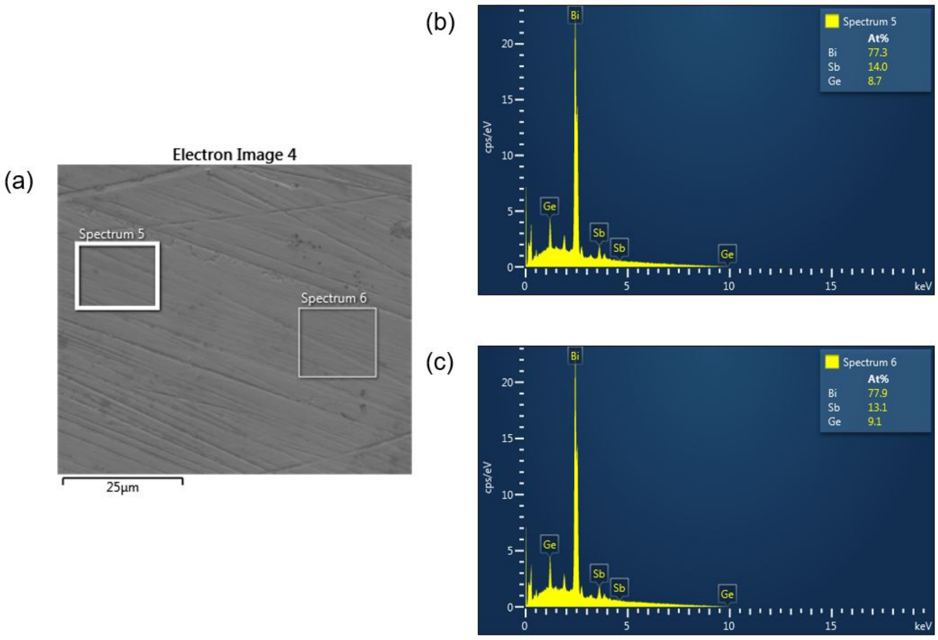

Figure 3.13: SEM image and EDS spectrum of $Bi_{85}Sb_{15}Ge_{10}$

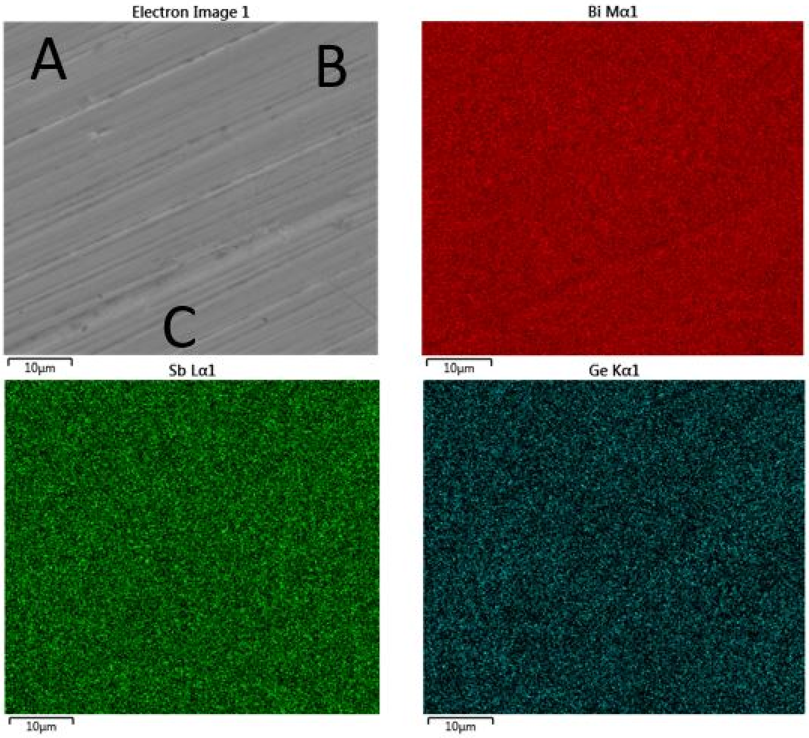

Figure 3.14: SEM image and EDS mapping of $Bi_{85}Sb_{15}Ge_{15}$

of Bi, Sb and Ge at different spots on the sample. We choose the several regions to measure the Ge content and the measured element distributions are all close to the expected composition values. The scale of the electron image is 10 μm. The atomic ratios (%) of Bi, Sb and Ge are (73.6, 13.0, 13.4), (73.8, 13.1, 13.1), (73.8, 12.6, 13.6) at point A, B and C, respectively, which are close to the expected value (74, 13, 13). Red mapping: Bi; green mapping: Sb; blue mapping: Ge.

3.3.2 Sn doped Bi-Sb

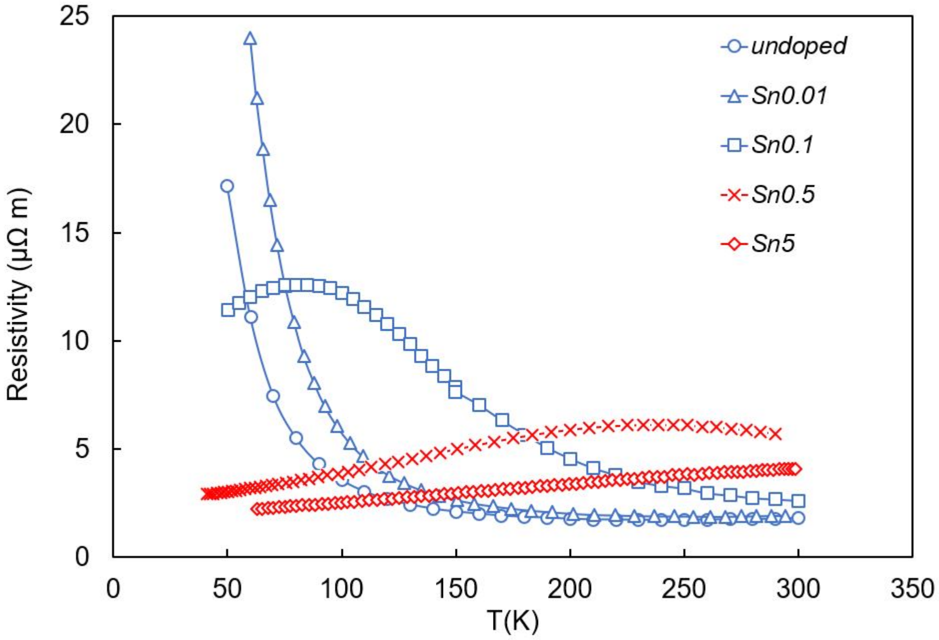

Figure 3.15: Resistivity of $Bi_{85}Sb_{15}$ samples doped with Sn

Sn has a higher solubility ($\sim$ 3 at%) in Bi-Sb than Ge and Pb. It has been better studied than Ge and Pb since it's easier to dope Sn into the system. The best figure of merit zT in the system of p-type Bi-Sb is found to be the single crystal Sn doped Bi-Sb which shows a zT of 0.13 at 230 K [43]. We have measured the transport properties of Sn doped Bi-Sb ranges from Sn0.01 to Sn5 made using the trivial SPS condition. The results are shown in Figure 3.15 and Figure 3.16.

The resistivity shifts up first as we add Sn into the system, and then it shifts down. This corresponds to the transition behavior from n-type semiconductor to p-type semiconductor. Adding p-type dopants moves the chemical potential

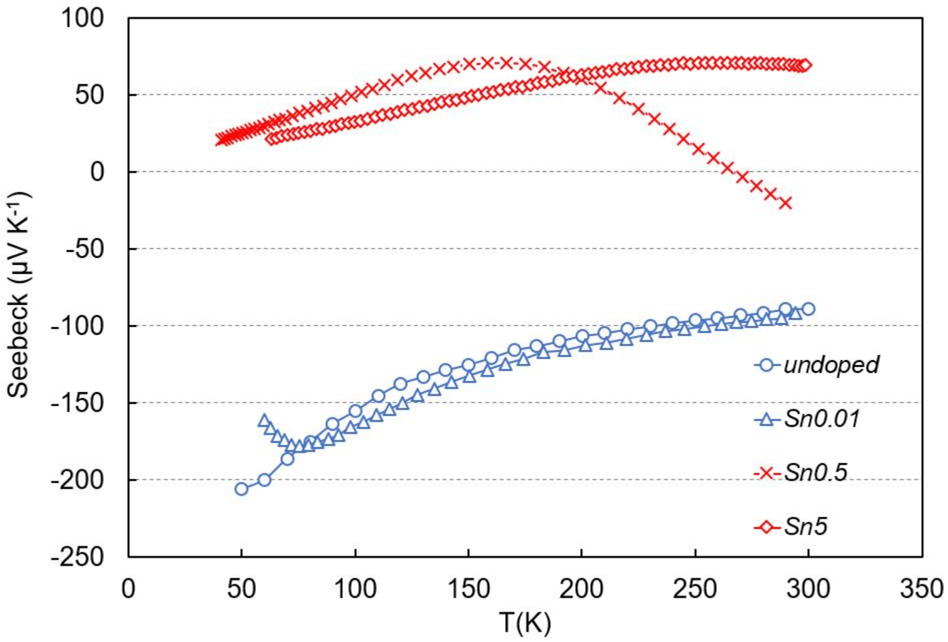

Figure 3.16: Seebeck of $Bi_{85}Sb_{15}$ samples doped with Sn

towards the valence band. The dopants in the matrix increase the carrier scattering rate. Those two factors have influence on the carrier concentration and the carrier mobility. As a result, the resistivity changes. The major charge carriers are electrons in the n-type samples. Due to the constraint of the charge neutrality, adding p-type dopants would decrease the electron concentration. Because of the enhanced scattering, the electron mobility decreases too which leads to a larger resistivity. After adding the p-type dopants to a certain amount, the major charge carriers in the system become to holes. The hole concentration increases if we keep adding p-type dopants and this can lead to a lower resistivity.

We detect the Sn-Sb phase in Sn5 sample as we discussed in the section of the X-ray diffraction patterns. The viscosity of the Sn5 doped Bi-Sb molten alloy is higher compared with lower amount of Sn doped alloys. This becomes an obstacle to produce melt-spun ribbons with high quality. This also happens for Pb doped samples. When the Pb content increases, the viscosity of the molten alloy increases. We cannot get good melt-spun ribbons for those samples. If the ribbon quality is not good, second phase usually appears in the sample.

The Sn doped samples show a strong metallic behavior at relatively low temperature (Sn0.5, below 150 K; Sn5, below 250 K). Similar to Ge, adding more Sn to the system shift the resistivity peak and the Seebeck peak to higher temperature and broaden the range of the positive Seebeck.

3.3.3 Pb doped Bi-Sb

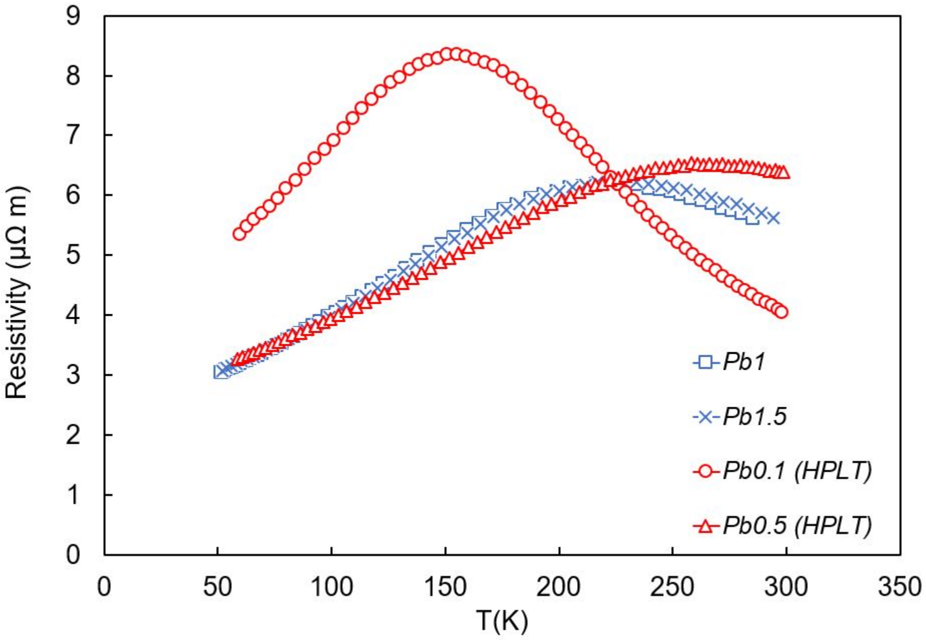

Figure 3.17: Resistivity of $Bi_{85}Sb_{15}$ samples doped with Pb

The solubility of Pb ($\sim$ 0.5 at %) is higher than Ge and less than Sn in Bi-Sb. Figure 3.17 and Figure 3.18 show the resistivity and the Seebeck of Pb doped samples. The samples made using the trivial SPS condition show the similar saturation effect as the Ge doped samples. The Pb1 and Pb1.5 samples do not have much difference on resistivity and Seebeck. After we apply the HPLT method, we can find that the Pb0.5 (HPLT) shows a more p-type behavior than Pb1 and Pb1.5 which indicates that doping becomes more effective with the HPLT method. Adding lower amount of Pb with the HPLT method shows higher Seebeck than higher amount of Pb doped samples made using the trivial SPS condition. The Seebeck peak value rises and the range of the positive Seebeck broadens. It is consistent with the Ge results that the HPLT method is helpful on doping low solubility elements in Bi-Sb.

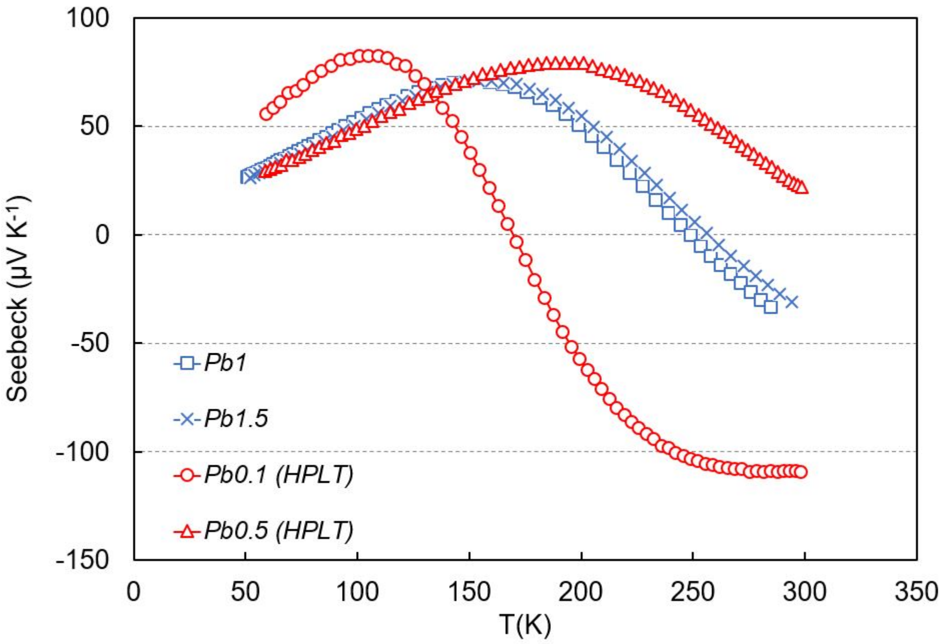

Figure 3.18: Seebeck of $Bi_{85}Sb_{15}$ samples doped with Pb

The molten high amount Pb doped sample has a high viscosity and we cannot get ribbons with good quality for the sample. Also, considering the toxicity of Pb, we do not add as much Pb as Ge and Sn in Bi-Sb.

3.3.4 Undoped Bi-Sb made using the HPLT method

It's important to see if the HPLT method affects the undoped Bi-Sb and the results are shown in Figure 3.19 and Figure 3.20. It is confirmed that the resistivity and the Seebeck doesn't change much after we apply the HPLT method to undoped Bi-Sb which indicates that this method mainly involves the doping process in Bi-Sb rather than Bi-Sb itself.

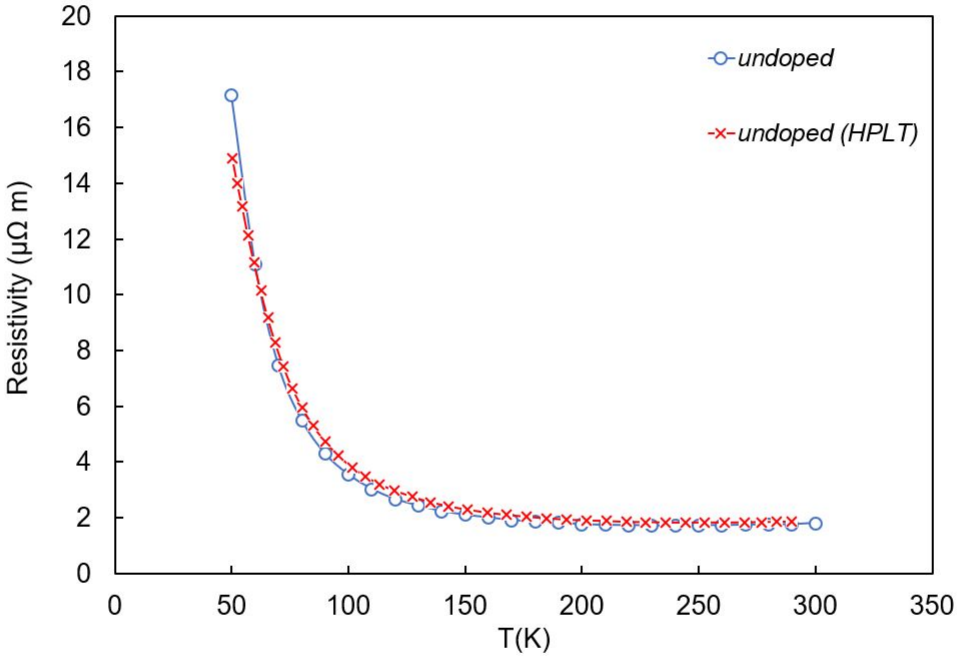

Figure 3.19: Resistivity comparison between trivial undoped and HPLT undoped $Bi_{85}Sb_{15}$ samples

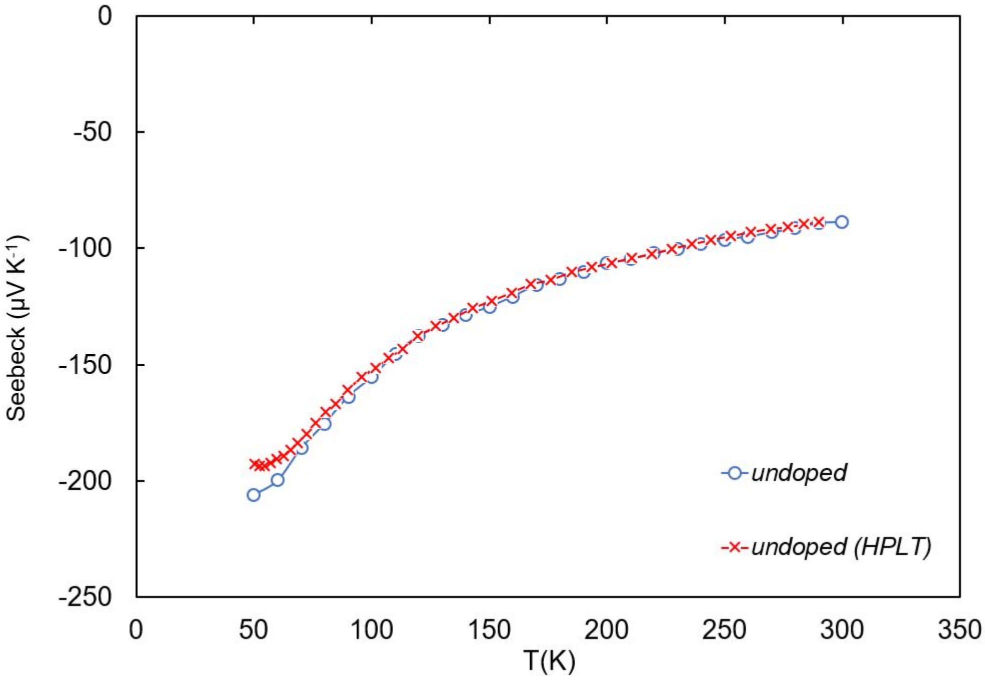

Figure 3.20: Seebeck comparison between trivial undoped and HPLT undoped $Bi_{85}Sb_{15}$ samples

3.3.5 Power factor of Ge, Sn and Pb doped Bi-Sb

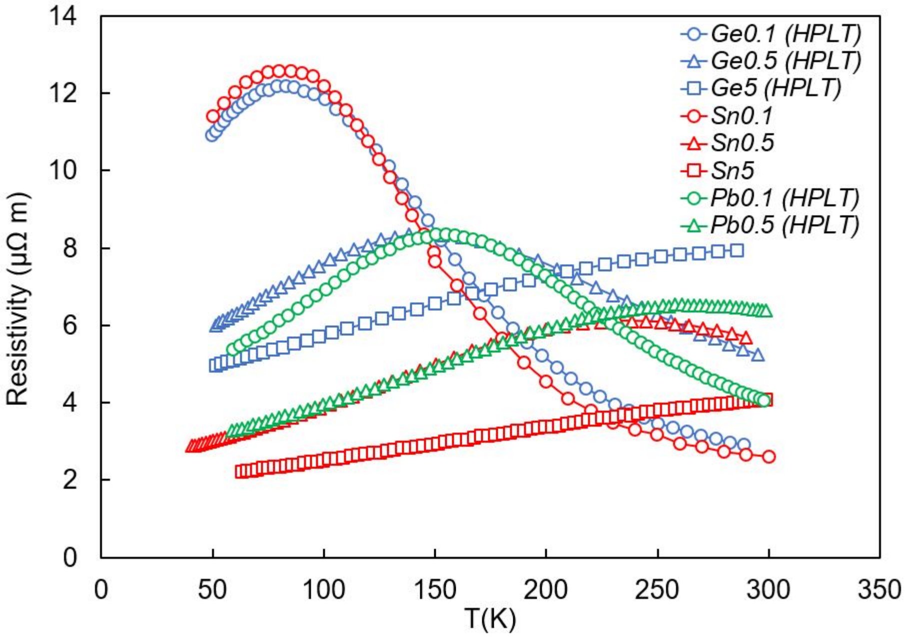

Figure 3.21: Resistivity of $Bi_{85}Sb_{15}$ samples doped with Ge, Sn, and Pb

We plot the Ge, Sn, and Pb results together in Figure 3.21, Figure 3.22, and Figure 3.23 to make comparison between the samples with different kinds of dopants. In the power factor (PF) plot, the rising part after the turning point at PF = 0 corresponds to the n-type region. We only focus on the p-type region which is before the turning point.

The highest Seebeck value is around 80 $\mu V K^{-1}$ and several different samples possess this value including Ge0.1 (HPLT) at 70 K, Pb0.1 (HPLT) at 110 K, Pb0.5 (HPLT) at 180 K, and Ge5 (HPLT) at 230 K.

It can be seen that Pb0.5 (HPLT) has the highest power factor ($\sim 1.1\, mW m^{-1} K^{-2}$) between 120 K and 180 K. Sn0.5 is also of interest because of its decent power factor ($\sim 1.0\, mW m^{-1} K^{-2}$) and its low toxicity compared to Pb. Although Sn5 sample has the highest power factor, it peaks around 250 K. In the temperature region below 200 K, it's not as good as Sn0.5 and Pb0.5 (HPLT) samples.

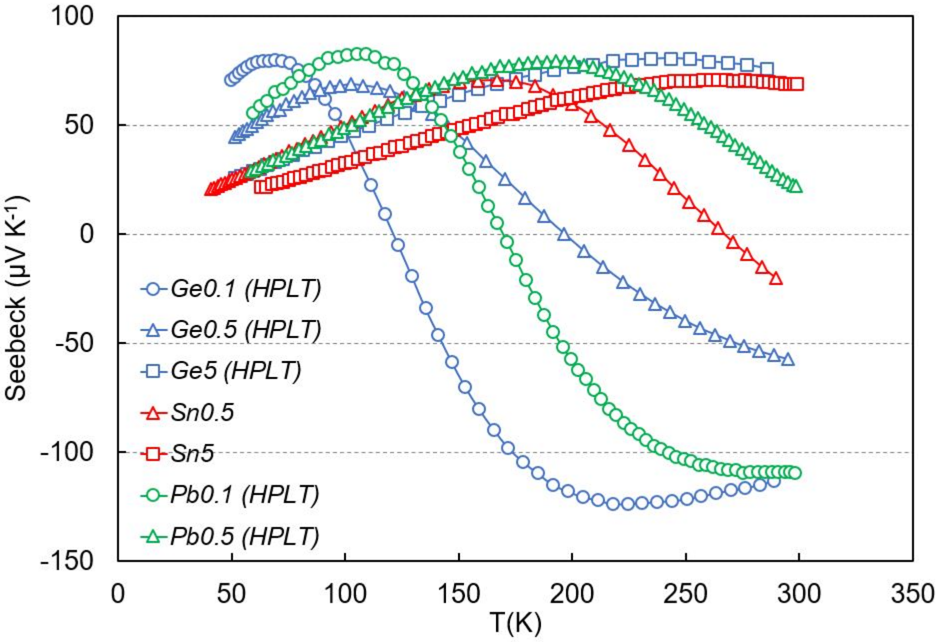

Figure 3.22: Seebeck of $Bi_{85}Sb_{15}$ samples doped with Ge, Sn, and Pb

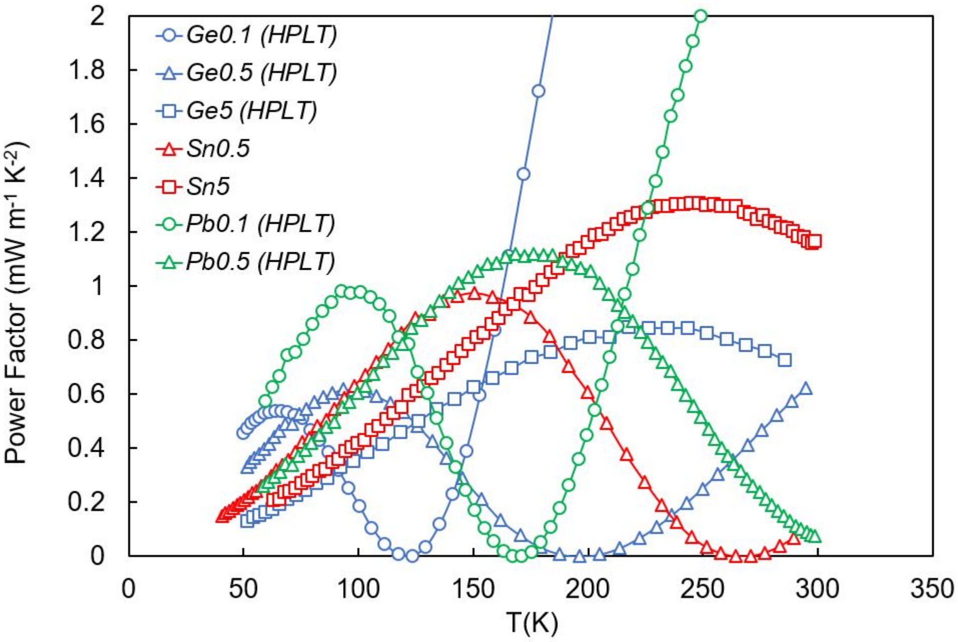

Figure 3.23: Power factor of $Bi_{85}Sb_{15}$ samples doped with Ge, Sn, and Pb

3.3.6 Hall coefficient and the doping efficiency of Ge, Sn, and Pb in Bi-Sb

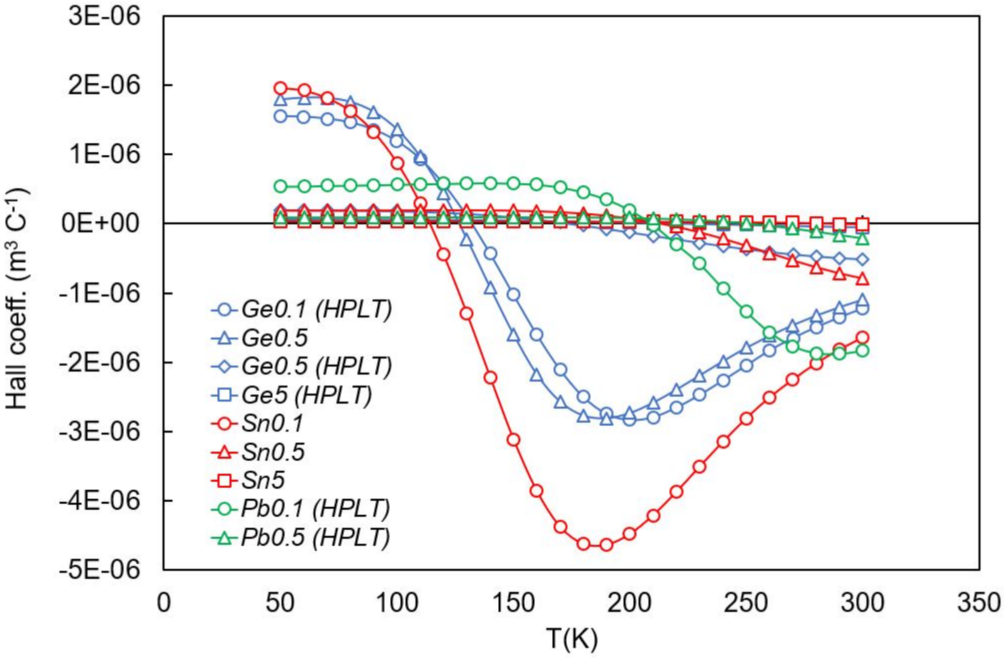

Figure 3.24: Hall coefficient of $Bi_{85}Sb_{15}$ samples doped with Ge, Sn, and Pb in linear scale

We plot the Hall coefficient and the carrier concentration of Ge, Sn, and Pb doped Bi-Sb samples in linear scale (Figure 3.24 and Figure 3.25) and logarithmic scale (Figure 3.26 and Figure 3.27). The Hall coefficients of those samples are measured from room temperature down to 50 K. The carrier concentration is calculated using the single band approximation Equation 3.1. The hole concentrations are constant for most of the samples below 100 K at which the hole channel dominates the transport behavior. The discrete points on curves represent the turning points of sign. After that turning point, the Hall coefficient changes the sign which means the major carriers in the alloy change from holes to electrons. The increased value of the carrier concentration doesn't represent the real increase of the hole concentrations. Rather it should be interpreted as the competition between the hole channel and the electron channel which leads to a smaller Hall coefficient. If using the single band Hall formula, we then calculate a large carrier concentration value.

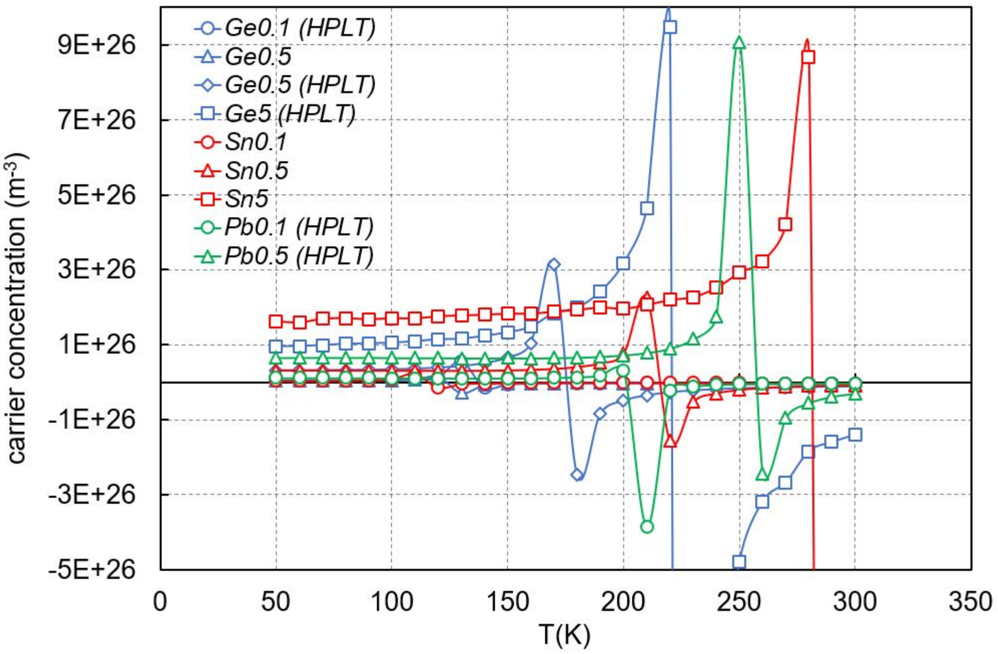

Figure 3.25: Carrier concentration of $Bi_{85}Sb_{15}$ samples doped with Ge, Sn, and Pb in linear scale

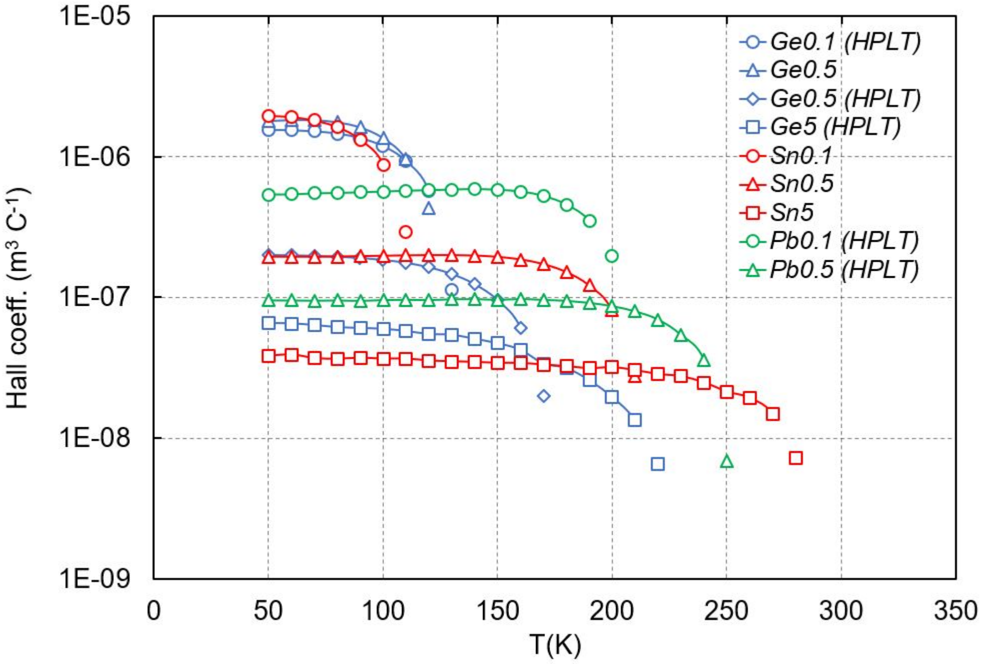

Figure 3.26: Hall coefficient of $Bi_{85}Sb_{15}$ samples doped with Ge, Sn, and Pb in logarithmic scale

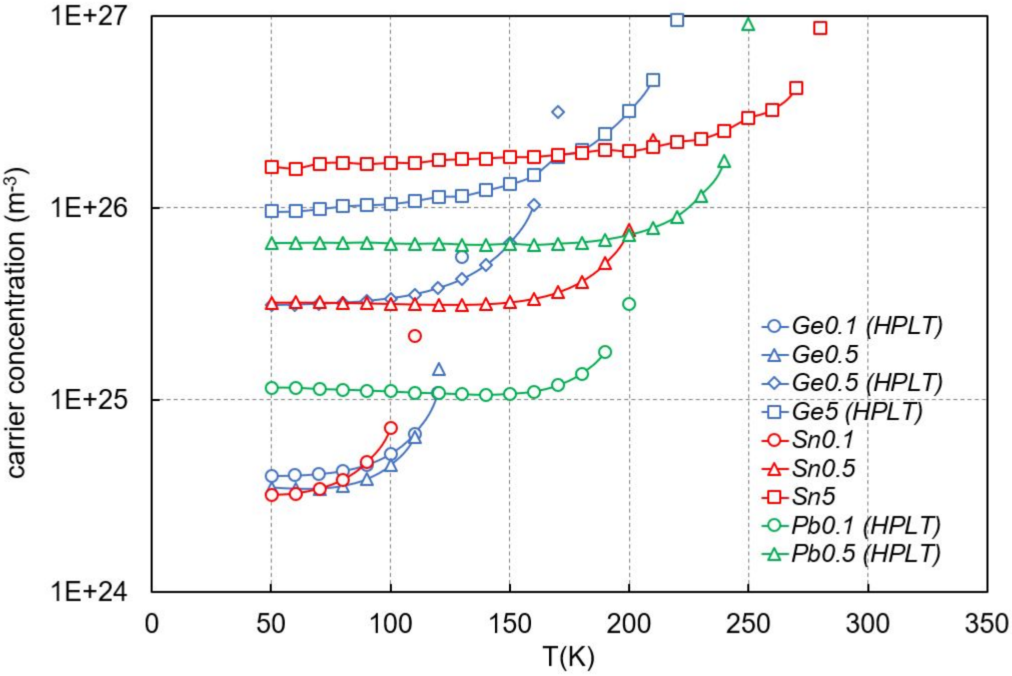

Figure 3.27: Carrier concentration of $Bi_{85}Sb_{15}$ samples doped with Ge, Sn, and Pb in logarithmic scale

$$R_H \approx \frac{1}{ep} \tag{3.1}$$

where R_H is the Hall coefficient, e is the unit charge, and p is the hole concentration.

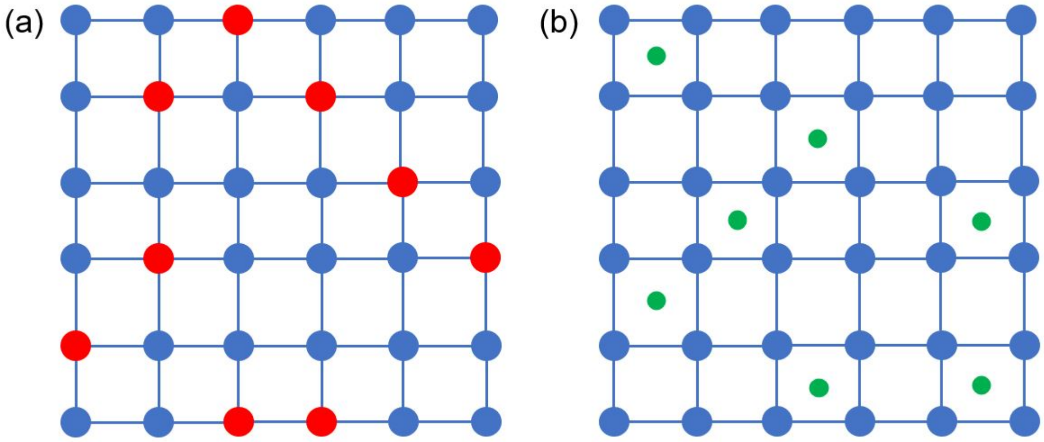

Figure 3.28: The blue circles represent alloy matrix. (a) The red circles represent substitutional dopants. (b) The green circles represent interstitial dopants.

We can make the assumption that each Ge/Sn/Pb atom in Bi-Sb matrix either be a substitutional acceptor or an interstitial donor and then calculate the doping efficiency. Figure 3.28 shows the diagram of substitutional occupation and interstitial occupation in an alloy matrix. The doping efficiency is defined below [53]:

$$\eta_{doping} = \frac{p}{N_a^-} \tag{3.2}$$

where p is the hole concentration and N_a^- is the acceptor concentration. The Ge/Sn/Pb doping efficiency are calculated and shown in Table 3.2.

	$Ge_{0.1}$	$Ge_{0.5}$	Ge_5	$Sn_{0.1}$	$Sn_{0.5}$	Sn_5	$Pb_{0.1}$	$Pb_{0.5}$
Doping efficiency (%)	24.7	35.7	12.7	20.0	36.7	21.0	57.7	63.1

Table 3.2: The doping efficiency of the doped $Bi_{85}Sb_{15}(Ge, Sn, Pb)_x$ samples.

The doping efficiency of Ge is comparable to Sn when the content of Ge and Sn is low. When we increase the Ge and Sn to Ge5 and Sn5, we can see that the doping efficiency decreases. This can be explained with the local clustering of the dopant atoms. If the dopant atoms cluster together in the Bi-Sb matrix, they do not effectively occupy the substitutional sites or interstitial sites in the matrix. This leads to a lower doping efficiency. The doping efficiency of Pb is the highest among Ge, Sn, and Pb. We can see that the carrier concentration of Pb0.1 sample is larger than Ge0.1 and Sn0.1 samples. The same is true for Pb0.5 sample compared to Ge0.5 and Sn0.5 samples. It can be explained using the atomic radius and interstitial and substitutional sites. The atomic radii of Bi, Sb, Ge, Sn, and Pb are 156 pm, 140 pm, 122 pm, 140 pm, and 175 pm respectively. We can find that the Pb atom has the largest atomic radius among all the elements considered above. So, it has a larger possibility to occupy the substitutional sites rather than go into the interstitial sites. This leads to a higher hole doping efficiency for Pb since we can have more substitutional acceptors in Pb doped samples. The atomic radii can also help explain why we can input much Ge into the Bi-Sb alloy. Since the atomic radii of Ge is significantly smaller than Bi and Sb, there are enough space for Ge particles to go into the Bi-Sb matrix.

3.4 Strategies to enhance the thermoelectric performance of p-type Bi-Sb

In this section, we discuss several strategies that we apply to improve the power factor of p-type Bi-Sb alloys. All the samples discussed in this section are made using the HPLT method except for pure Sn doped samples and the post high-pressure samples.

3.4.1 Ge + Pb/Sn codoped Bi-Sb

We are interested in the high content Ge doped samples since it is an innovative work. Because Pb has a higher doping efficiency than Ge, we decide to codope some Pb with Ge and see if the TE properties can be enhanced.

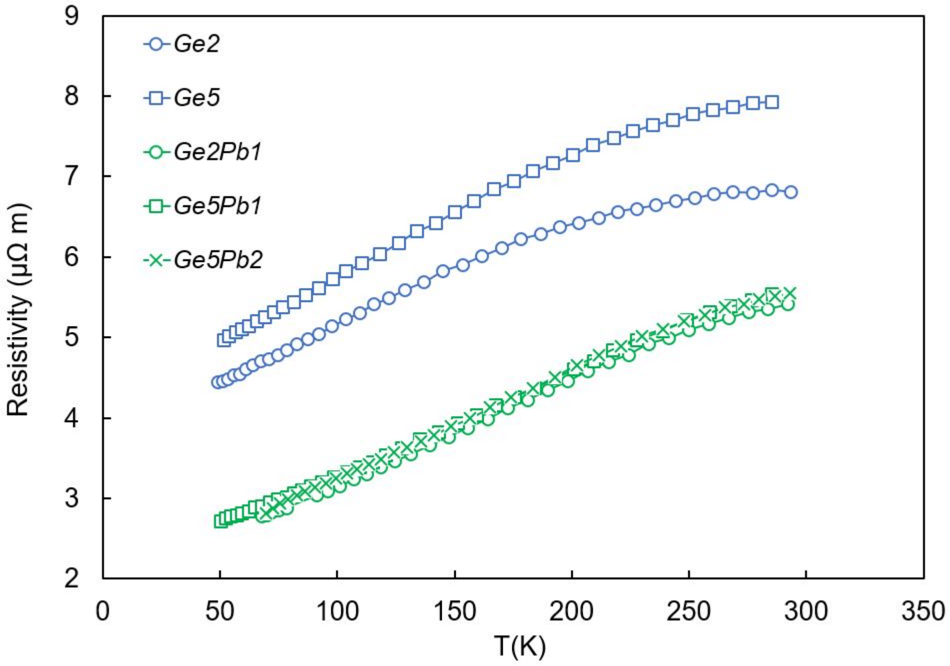

Figure 3.29: Resistivity of $Bi_{85}Sb_{15}$ samples codoped with Ge and Pb

As Figure 3.29, Figure 3.30, and Figure 3.31 show, Pb can significantly decrease the resistivity and broaden the positive Seebeck range. At low temperature,

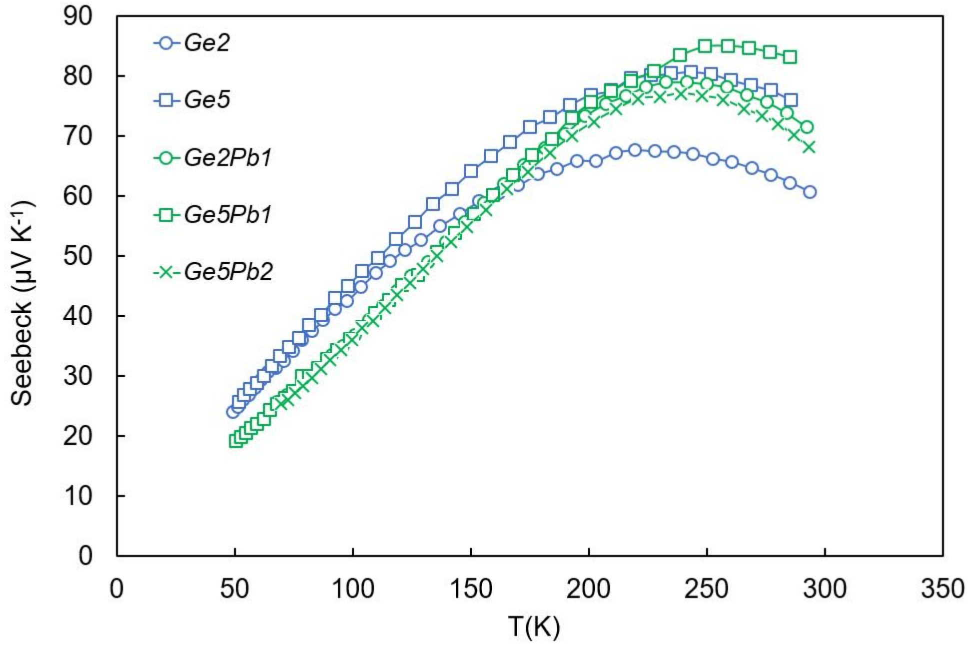

Figure 3.30: Seebeck of $Bi_{85}Sb_{15}$ samples codoped with Ge and Pb

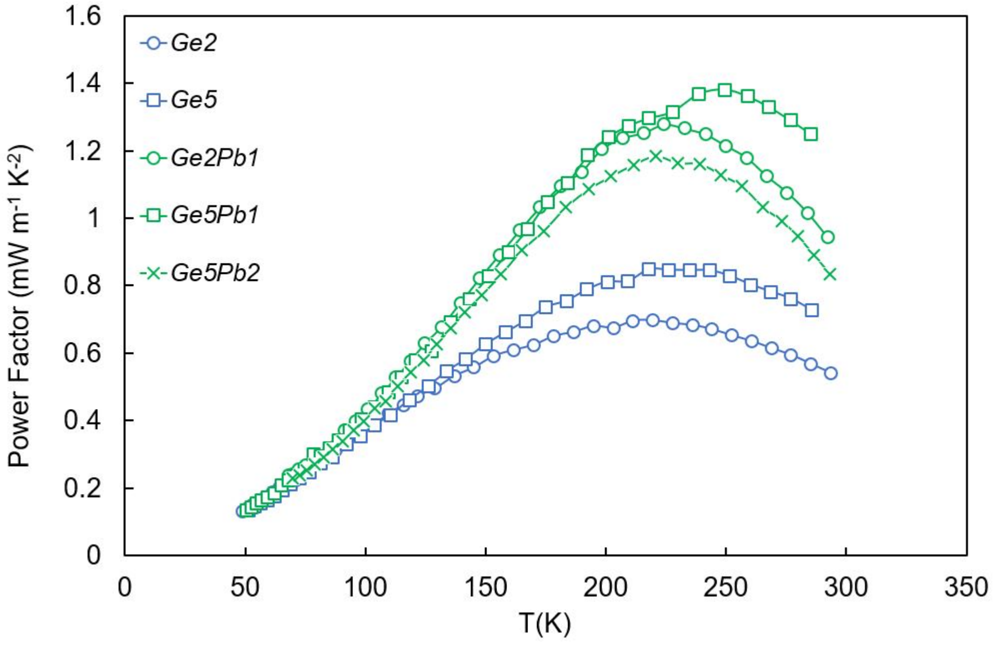

Figure 3.31: Power factor of $Bi_{85}Sb_{15}$ samples codoped with Ge and Pb

the Seebeck decreases because of the higher carrier concentration. This can be explained using Equation 1.8. The power factor benefits from the low resistivity. Ge5Pb1 sample has the highest power factor 1.38 $mWm^{-1}K^{-2}$ around 250 K.

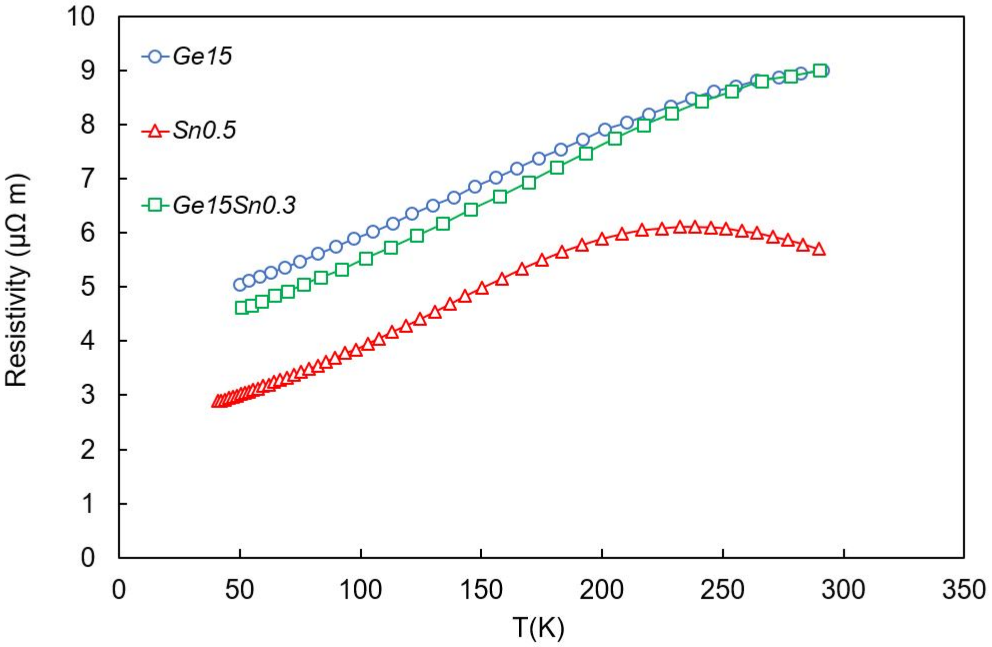

Figure 3.32: Resistivity of $Bi_{85}Sb_{15}$ samples codoped with Ge and Sn

Figure 3.32, Figure 3.33, and Figure 3.34 show the results of Bi-Sb codoped with Ge15 and a little amount of Sn. We are interested in the properties of Ge15 sample. A little amount of Sn is added into the system in order to optimize its resistivity. After adding Sn, the resistivity decreases a little and the Seebeck increases a little which leads to an enhanced power factor. The maximum of the power factor of Ge15Sn0.3 sample is about 1 $mWm^{-1}K^{-2}$ at 230 K. This is an interesting effect because we expect the resistivity to decrease and also the Seebeck to decrease a little due to the increase of the carrier concentration after adding Sn. But the Seebeck increases instead, this indicate that a little amount of Sn can affect the density of states effective masses of $Bi_{85}Sb_{15}Ge_{15}$ system and also change the carrier concentration. A lot of Ge particles go into the interstitial sites which leaves space for Sn to take the substitutional sites and work as acceptors.

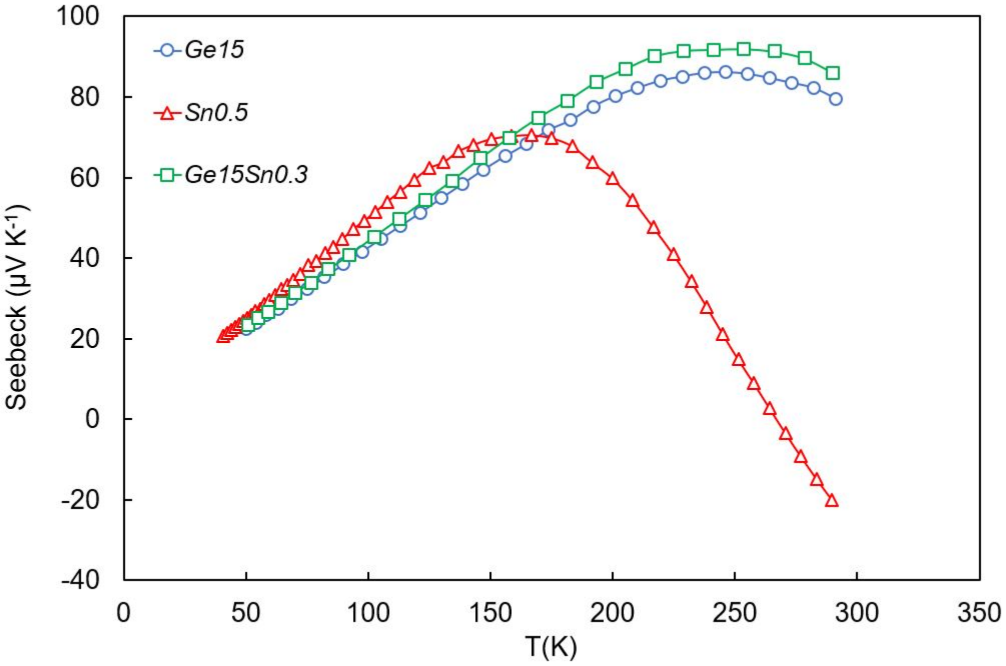

Figure 3.33: Seebeck of $Bi_{85}Sb_{15}$ samples codoped with Ge and Sn

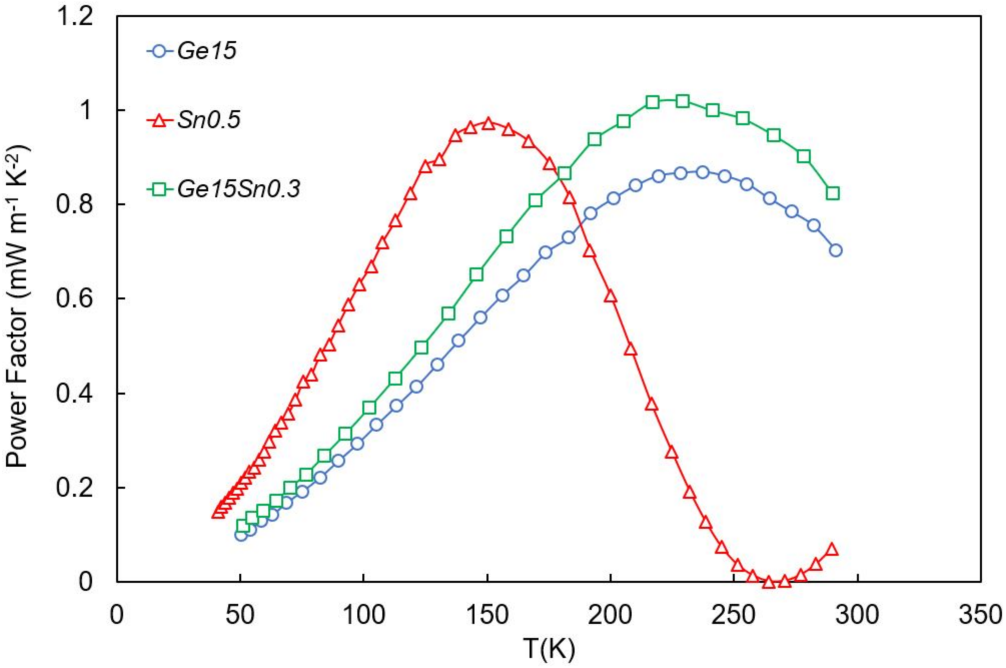

Figure 3.34: Power factor of $Bi_{85}Sb_{15}$ samples codoped with Ge and Sn

3.4.2 Transition metal + Sn/Pb codoping effects

In this subsection and the next subsection, we discuss the codoping effects of transition metals and Te with Sn/Pb in Bi-Sb alloys. We are inspired to put transition metals/Te with Sn/Pb in Bi-Sb by the doping effects of pure Ni/Te in Bi-Sb. Figure 3.35 and Figure 3.36 show the resistivity and the carrier concentration of the Ni doped Bi-Sb and the Te doped Bi-Sb samples. We find that both Ni and Te are n-type dopants while Te is much more effective than Ni. The Te doped Bi-Sb shows a metallic behavior and its carrier concentration is several orders higher than Ni doped and undoped Bi-Sb. Knowing the resistivity and the carrier concentration, we can calculate the electron mobility of the sample. We find that the mobility decreases a lot in Ni/Te doped samples compared with undoped Bi-Sb. This is a useful information. We observe that the Seebeck of the p-type Bi-Sb samples crashes when temperature rises and that is because of the participation of the electron channel in the transport. If we can weaken the electron channel, then there is a chance that the Seebeck can last to higher temperature. By putting Ni/other transition metals/Te in p-type Bi-Sb samples, we can test the idea.

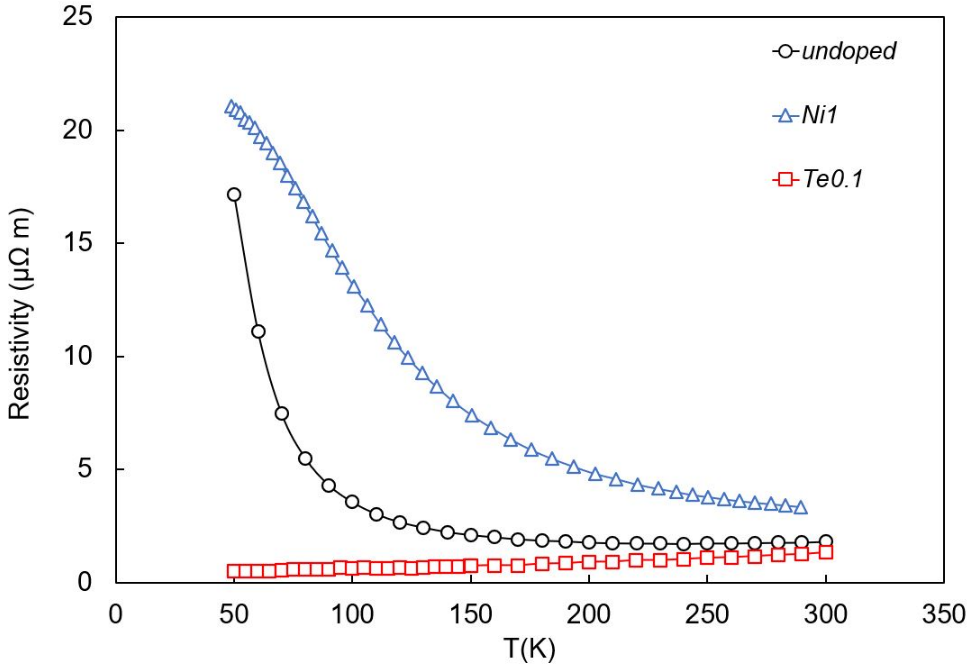

Figure 3.35: Resistivity of $Bi_{85}Sb_{15}$ samples doped with Ni or Te

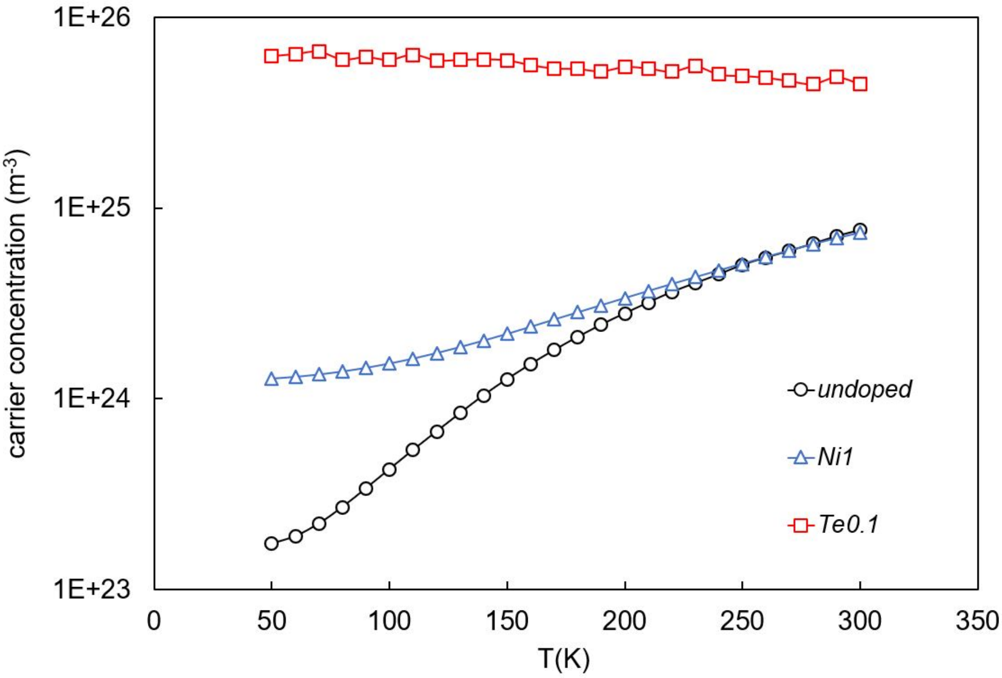

Figure 3.36: Carrier concentration of $Bi_{85}Sb_{15}$ samples doped with Ni or Te

Transition metal + Sn codoping effects

Figure 3.37 and Figure 3.38 show the results of Ni+Sn and Pt+Sn codoped Bi-Sb samples.

We find that adding Ni or Pt increases the resistivity, Seebeck coefficient of the samples. We measure the Hall coefficient and calculate the carrier concentration of Ni1Sn0.5 sample. Interestingly, adding Ni increases the hole concentration compared with Sn0.5 sample as shown in Figure 3.39. This can be explained as following: The atomic radius of Ni is 124 pm while the atomic radii of Bi, Sb, and Sn are 156 pm, 140 pm, and 140 pm, respectively. Since the radius of Ni is smaller than Bi, Sb, and Sn, Ni tends to occupy the interstitial sites. Thus, there is less chance for Sn to occupy the interstitial sites. Compared with pure Sn doped Bi-Sb samples, more Sn atoms may occupy the substitutional sites in Ni-Sn codoped Bi-Sb samples and work as acceptors.

The power factors are calculated and shown in Figure 3.40. Ni1Sn0.5 sample shows the highest power factor, around 1.21 $mWm^{-1}K^{-2}$ at 180 K. It's benefited from the enhanced Seebeck. The resistivity of the Pt-Sn codoped sample is too

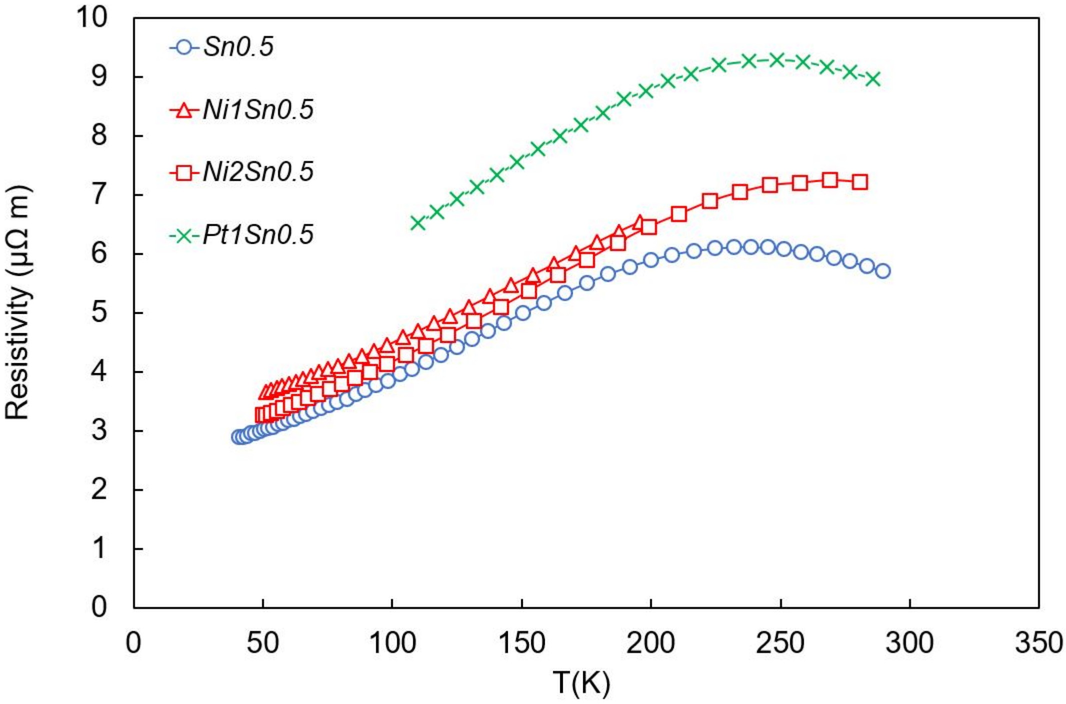

Figure 3.37: Resistivity of $Bi_{85}Sb_{15}$ samples codoped with transition metals and Sn

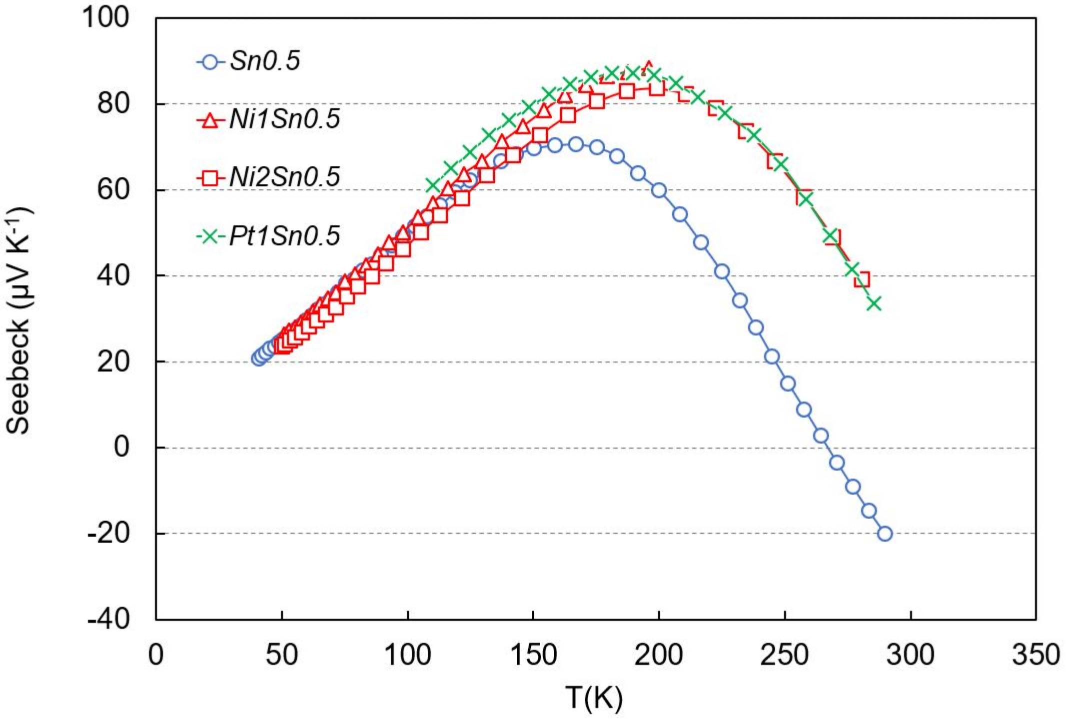

Figure 3.38: Seebeck of $Bi_{85}Sb_{15}$ samples codoped with transition metals and Sn

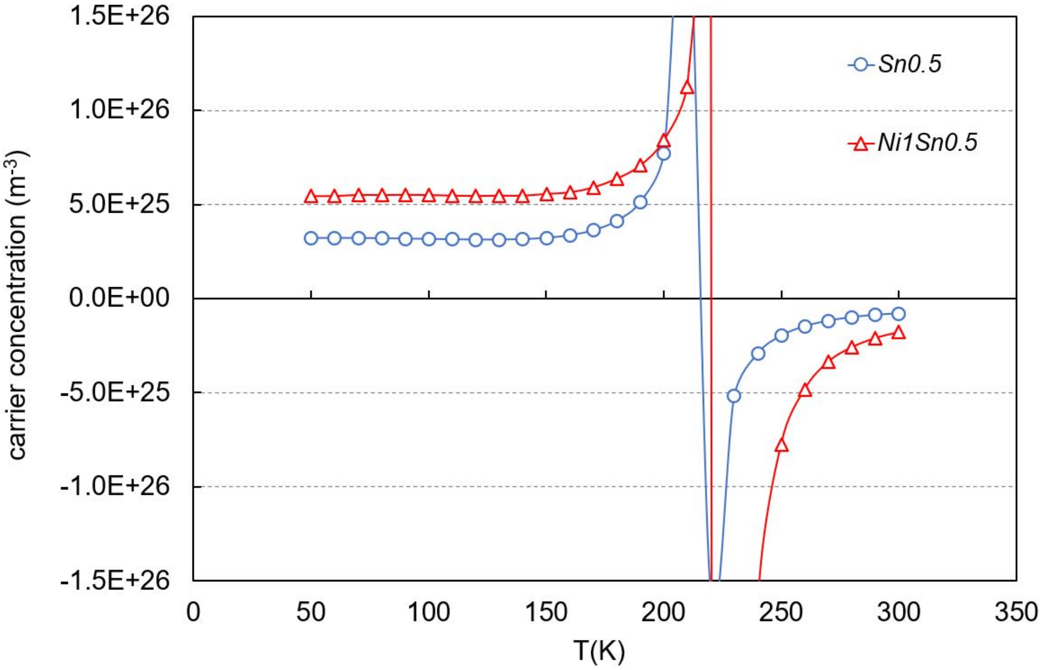

Figure 3.39: Carrier concentration of $Bi_{85}Sb_{15}$ samples codoped with Ni and Sn

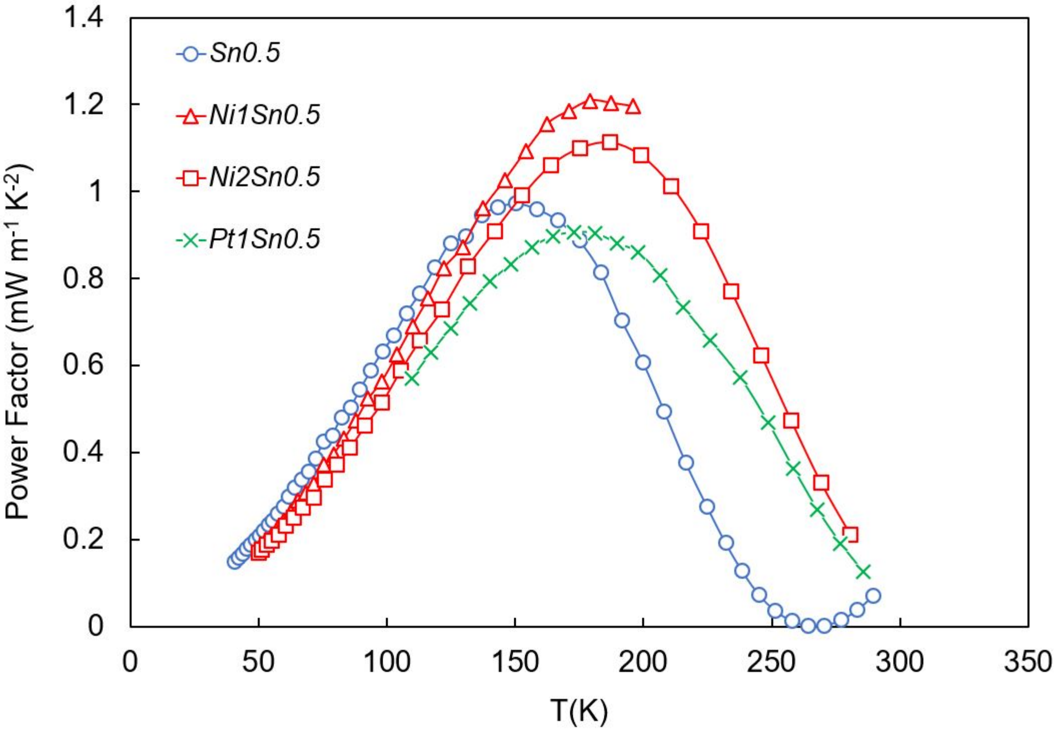

Figure 3.40: Power factor of $Bi_{85}Sb_{15}$ samples codoped with transition metals and Sn

high which ruins the power factor.

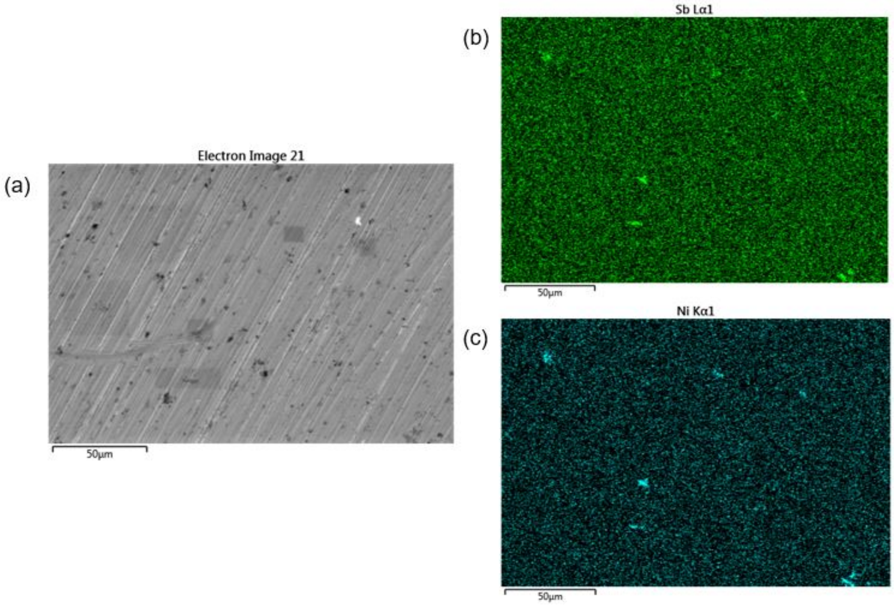

Figure 3.41: SEM image and EDS mapping of a Bi-Sb sample doped with Ni2

Ni seems to be promising to enhance the TE performance of p-type Bi-Sb. However, adding too much Ni increases the viscosity of the molten alloy during the melt spinning process and this leads to the Ni-Sb phase. We can see the SEM/EDS results in Figure 3.41. Ni-Sb particles can be clearly seen in the mapping images. The second phase lowers down the effectiveness of Ni and we find that the power factor of Ni2Sn0.5 sample is smaller than that of Ni1Sn0.5.

Transition metal + Pb codoping effects

Pb is codoped with Ni, Fe, and Mn in Bi-Sb samples. The results are shown in Figure 3.42, Figure 3.43, and Figure 3.44. The changing trend of the resistivity and the Seebeck are similar to what happens in the transition metals+Sn codoped samples. We can observe a trend that the high resistivity corresponds to the high Seebeck. This can be explained with the carrier concentration. When the resistivity is high, the carrier concentration is relatively low and that leads to the relatively high Seebeck.

Adding Ni, Fe, and Mn raises the resistivity and the Seebeck of Pb doped Bi-Sb samples. The resistivity and the Seebeck shift up much more for Fe1Pb0.5

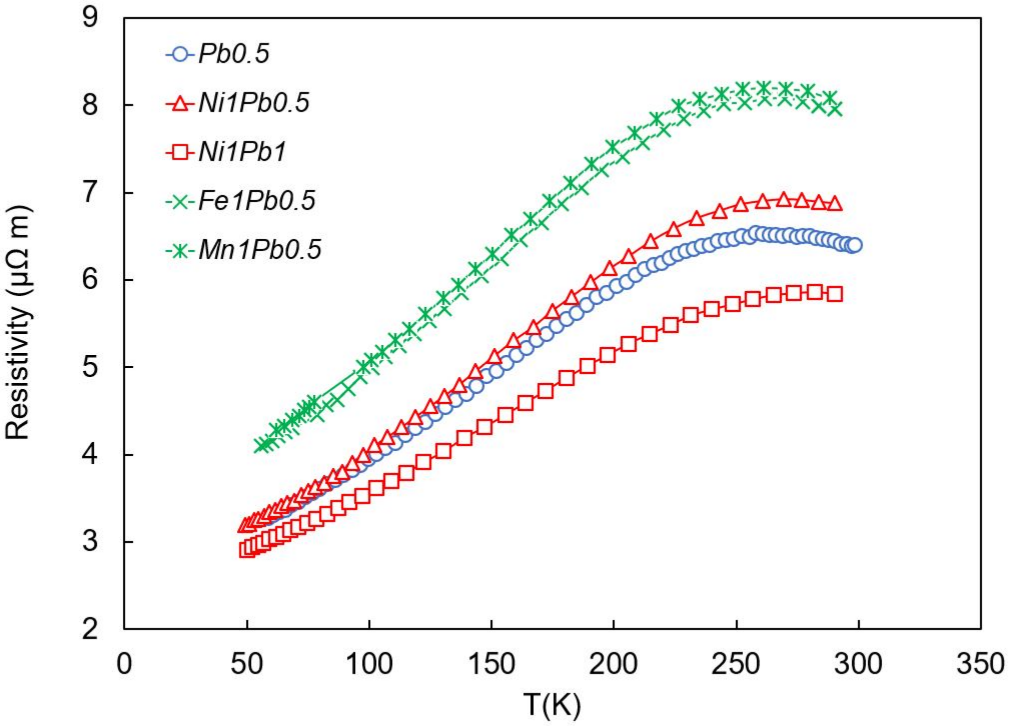

Figure 3.42: Resistivity of $Bi_{85}Sb_{15}$ samples codoped with transition metals and Pb

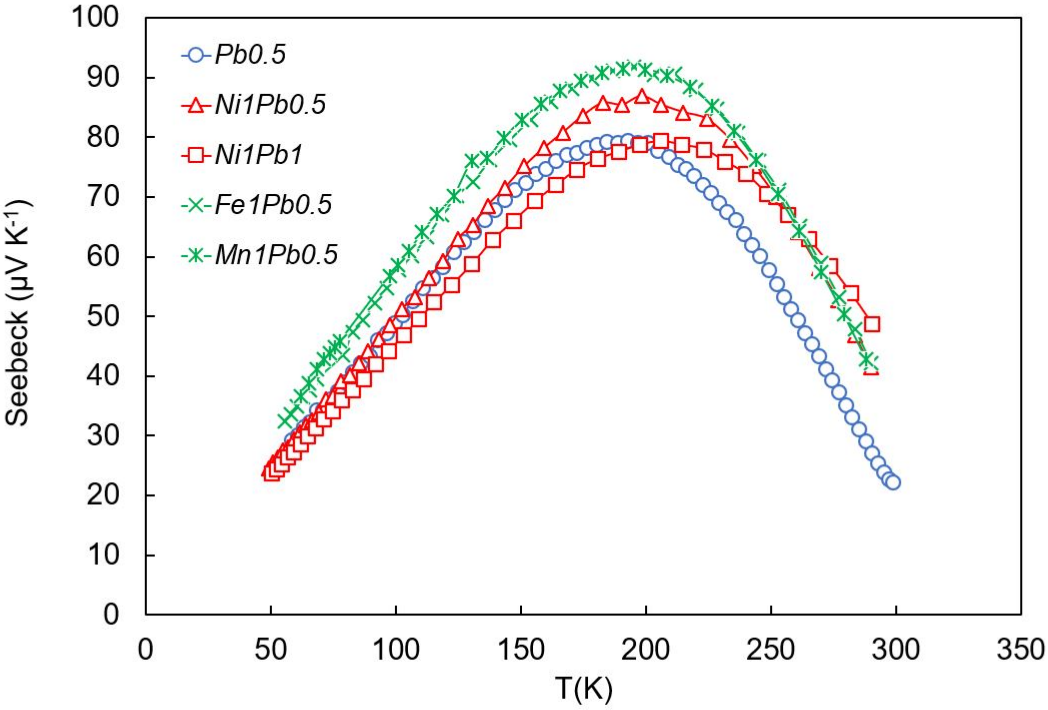

Figure 3.43: Seebeck of $Bi_{85}Sb_{15}$ samples codoped with transition metals and Pb

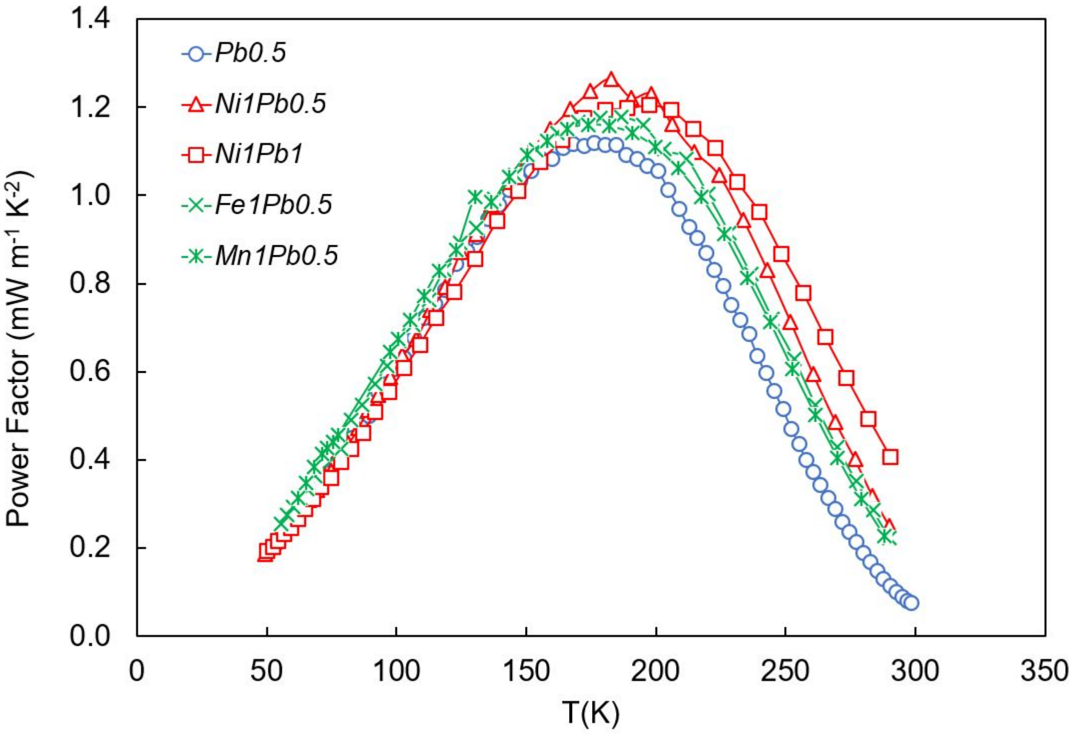

Figure 3.44: Power factor of $Bi_{85}Sb_{15}$ samples codoped with transition metals and Pb

and Mn1Pb0.5 samples than Ni1Pb0.5 sample. This means that adding Fe or Mn effectively decreases the hole mobility. Ni is quite different. The resistivities of the Pb0.5 and Ni1Pb0.5 samples are close to each other below 150 K. The Ni1Pb0.5 then extends the rising trend of resistivity and Seebeck above 150 K which indicates that adding Ni delays the participation of electron channel in the transport. As a result, Ni1Pb0.5 shows the highest power factor among those samples. The value is about $1.26\,mWm^{-1}K^{-2}$ at 180 K.

We can find the similar transition metal effects in Sn doped and Pb doped Bi-Sb alloys. Adding the transition metal particles increase the resistivity and the Seebeck of the samples. Based on the discussion on Ni1Sn0.5 and Ni1Pb0.5 samples, these effects can be attributed to the influence of the transition metal particles on the charge carrier mobilities. The transition metal particles enhance the scattering and decrease both the electron mobility and hole mobility which causes the increase of the resistivity. But the electron mobility would decrease more than the hole mobility especially for Ni codoped samples, so that the Seebeck can keep increasing to higher temperature.

Different Bi-Sb compositions doped with Ni1Pb0.5

As we discussed in the background information of Bi-Sb, changing Bi-Sb compositions affects the band structures. We change the Bi-Sb compositions and dope it with Ni1Pb0.5 and see what happens in the samples with different Bi-Sb compositions.

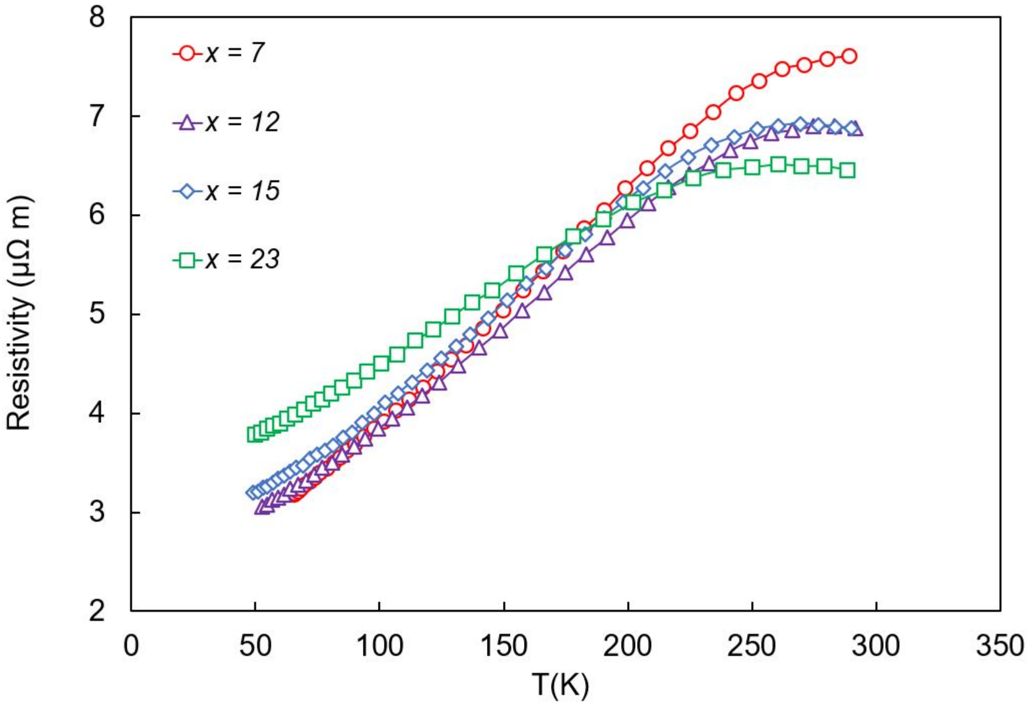

Figure 3.45: Resistivity of $Bi_{100-x}Sb_x$ samples codoped with Ni1Pb0.5

Figure 3.45, Figure 3.46, and Figure 3.47 show the results. It shows that $Bi_{88}Sb_{12}Ni_1Pb_{0.5}$ has the highest power factor around 1.4 $mWm^{-1}K^{-2}$ at 190 K. The Seebeck coefficient of $Bi_{77}Sb_{23}Ni_1Pb_{0.5}$ and $Bi_{93}Sb_7Ni_1Pb_{0.5}$ are not good and lead to a lower power factor.

In the band diagram of Bi-Sb, we know that it has the largest band gap around Sb15. At around Sb7 and Sb23, the band gap closes. This is where the semimetal-to-semiconductor transition happens. It confirms that we can get a larger p-type Seebeck at a relatively larger band gap and for Ni1Pb0.5 doped sample the best Bi-Sb composition is $Bi_{88}Sb_{12}$. In a sample with a larger band

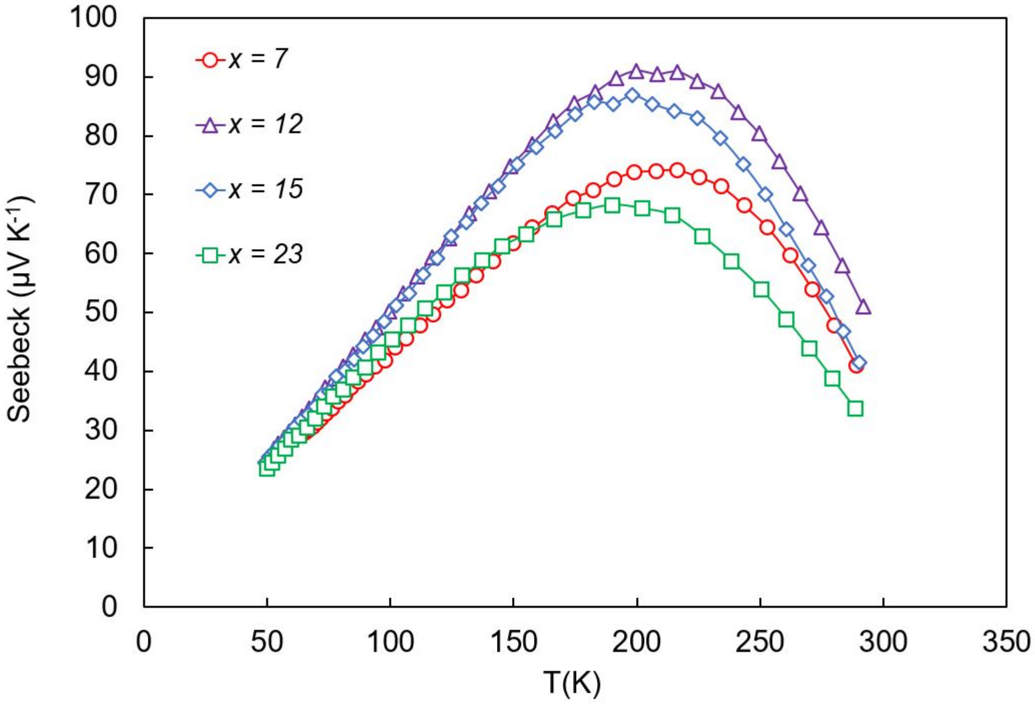

Figure 3.46: Seebeck of $Bi_{100-x}Sb_x$ samples codoped with Ni1Pb0.5

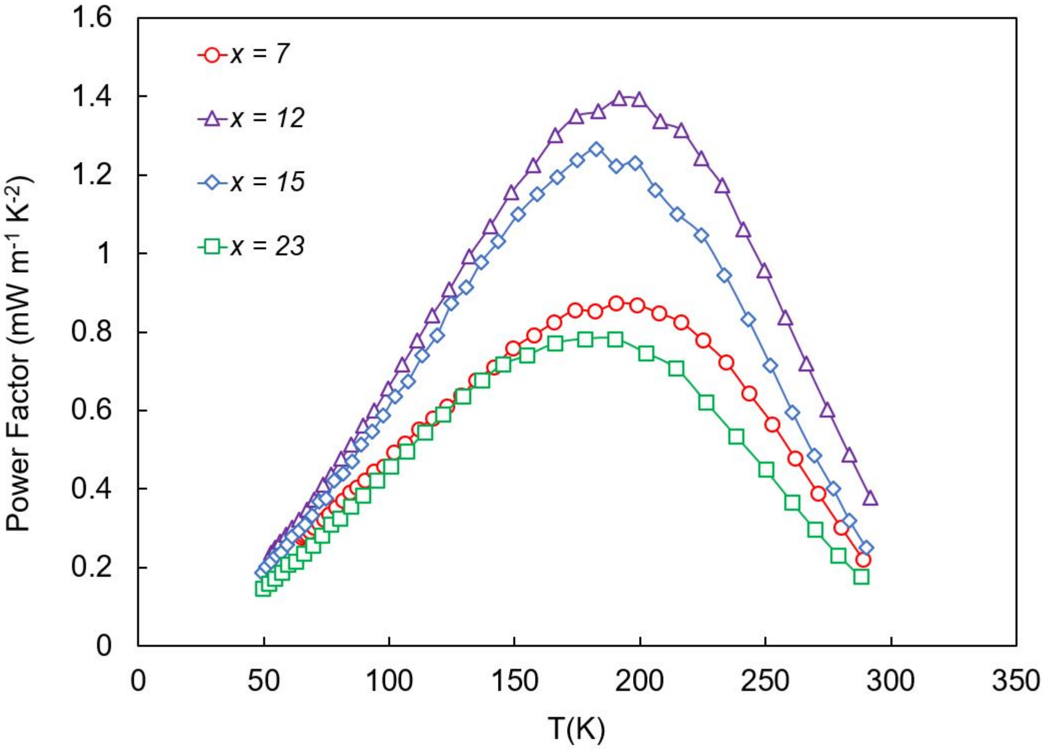

Figure 3.47: Power factor of $Bi_{100-x}Sb_x$ samples codoped with Ni1Pb0.5

gap, we need to raise to a higher temperature to excite the electron channel. This is good for our case because we are interested in the low temperature region and we don't want the electron channel to participate in the transport.

3.4.3 Te + Sn/Pb codoping effects

Te is an element of valence 6 and it works as an effective n-type dopant in Bi-Sb alloy.

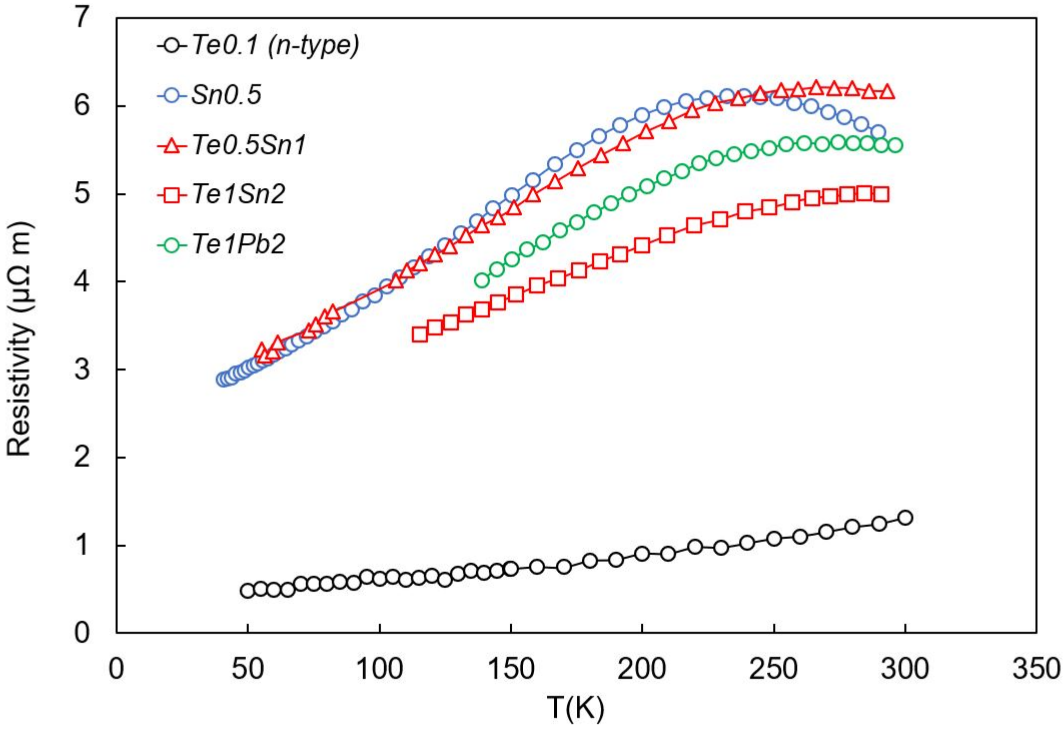

Figure 3.48: Resistivity of $Bi_{85}Sb_{15}$ samples codoped with Te and Sn/Pb

In p-type samples, adding Te moves the chemical potential towards to the conduction band and leads to a higher resistivity. So, we need to add more Sn to counter the effect. Adding Te is expected to effectively decrease the electron mobility and then increase the p-type Seebeck. The results are shown in Figure 3.48, Figure 3.49, and Figure 3.50.

Compared with Sn0.5 sample, the resistivity and the Seebeck curves of Te0.5Sn1 sample show the similar trend, but shift to higher temperature. The Seebeck is enhanced above 170 K. If we keep increasing Te and Sn to Te1Sn2, the

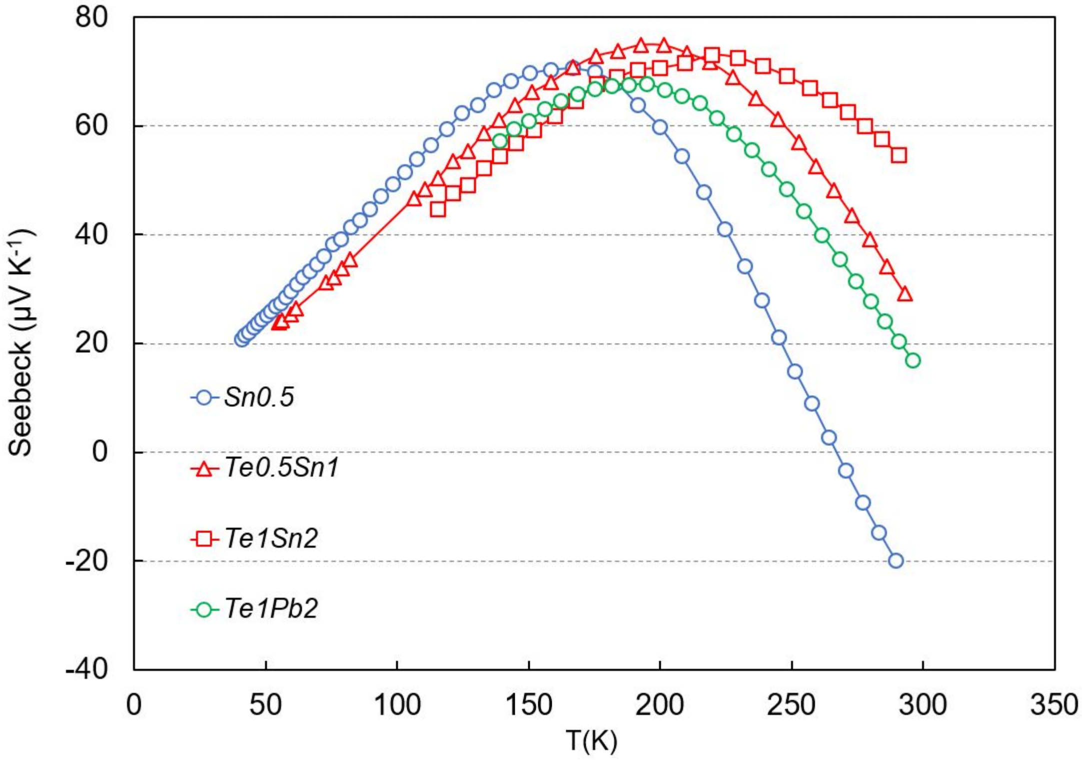

Figure 3.49: Seebeck of $Bi_{85}Sb_{15}$ samples codoped with Te and Sn/Pb

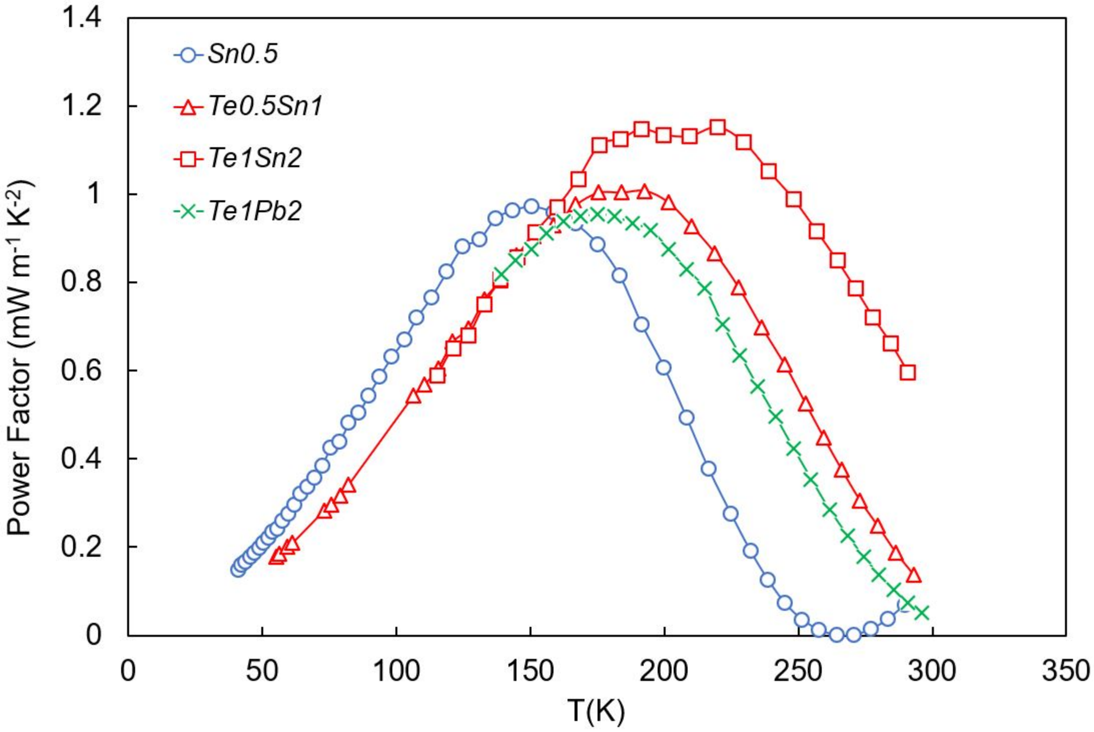

Figure 3.50: Power factor of $Bi_{85}Sb_{15}$ samples codoped with Te and Sn/Pb

resistivity of the sample decreases while the Seebeck curve keeps shifting to higher temeparture.

Te1Sn2 sample has the best power factor among those samples due to its low resistivity. Its power factor is above 1 in the temperature range between 160 K and 250 K.

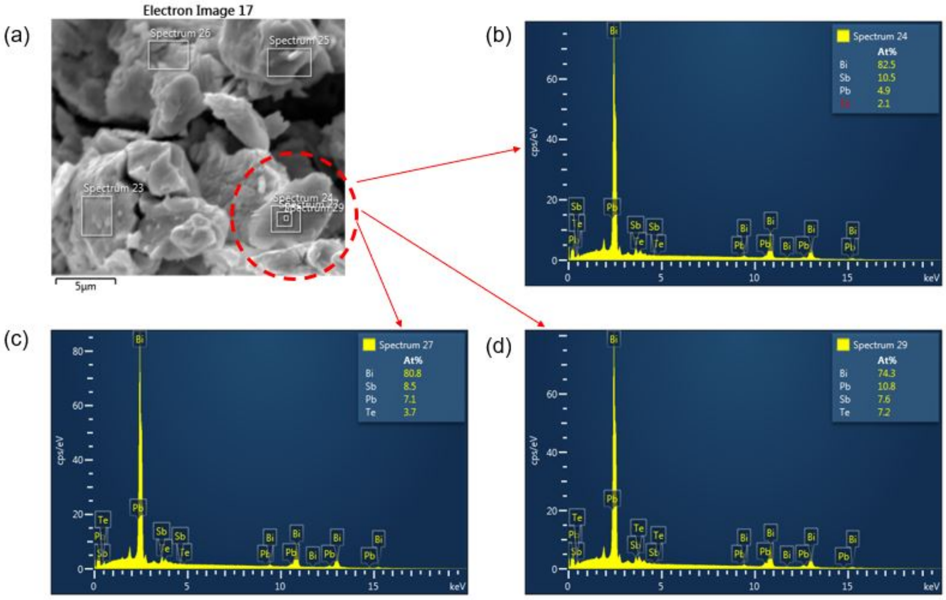

Figure 3.51: SEM image and EDS spectrum of $Bi_{85}Sb_{15}Te_1Pb_2$

We expect that replacing Sn with Pb will further decrease the resistivity since the doping efficiency of Pb is higher than Sn in Bi-Sb. However, this doesn't happen. We have tested the sample with EDS, the result is shown in Figure 3.51. It's possible that the PbTe phase leads to the result as we detect some PbTe cluster in the sample. We can see that at certain point, the Pb and Te content are much higher than expected which indicates the PbTe phase exists there.

Similar to the case of Ni, we cannot add too much Te into the system. Otherwise, we may get second phase such as SnTe or PbTe.

3.4.4 Post high-pressure effects

The post high-pressure effects were studied in the earlier stage of the research. The high-pressure was being applied after the sintering process. So, it is different from the HPLT method. The detailed SPS condition can be found in Table 2.2. The power factor of the p-type sample can be enhanced by applying the post high-pressure.

Post high-pressure effect in n-type Bi-Sb

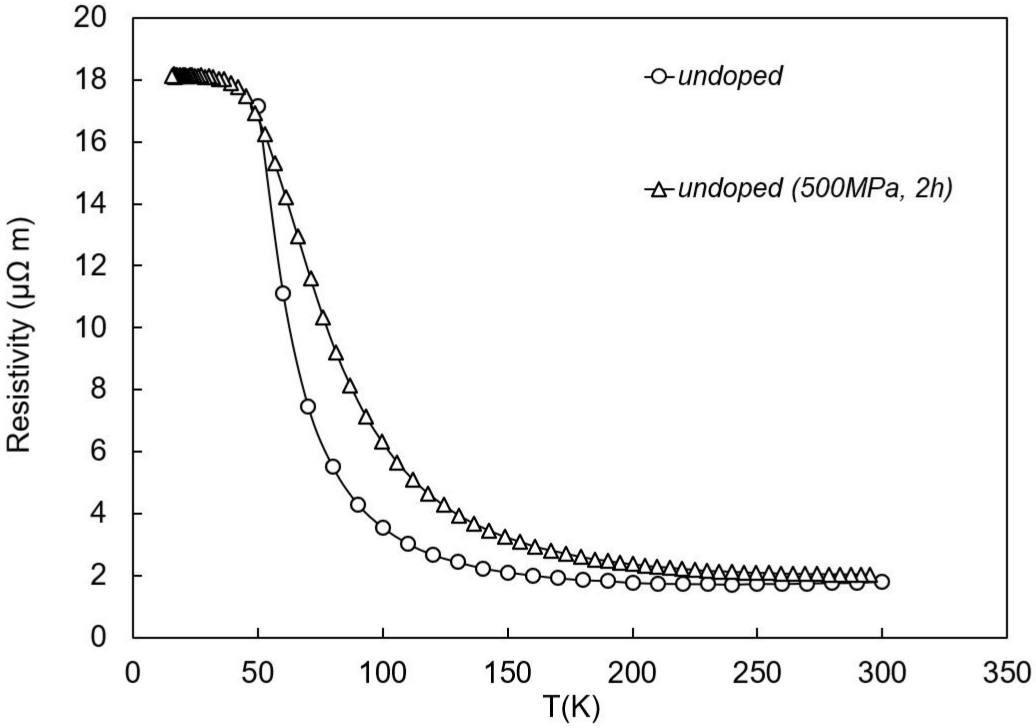

Figure 3.52: Resistivity of undoped post-high-pressure $Bi_{85}Sb_{15}$ sample

Let's see the post high-pressure effect in undoped Bi-Sb first. Figure 3.52, Figure 3.53, and Figure 3.54 show the resistivity, the Seebeck, and the carrier concentration of undoped Bi-Sb made with the post high-pressure. Compared with the undoped Bi-Sb made using the trivial SPS condition, the post high-pressure increases the resistivity, the Seebeck and the carrier concentration of the sample, and the electron mobility significantly decreases.

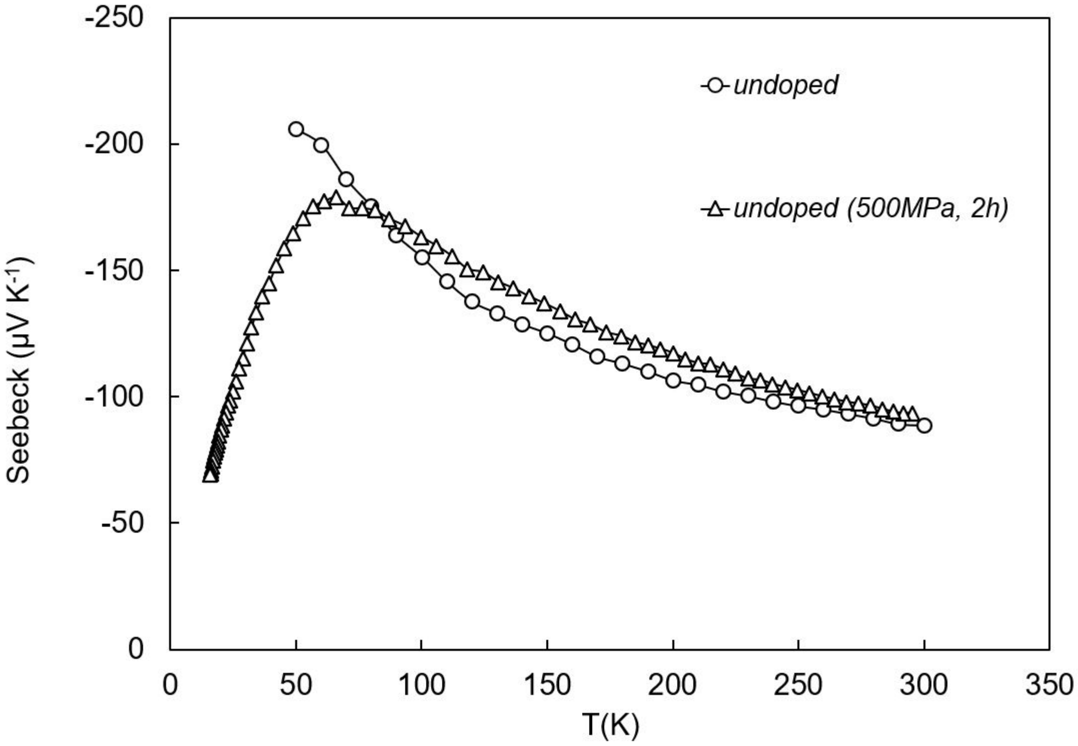

Figure 3.53: Seebeck of undoped post-high-pressure $Bi_{85}Sb_{15}$ sample

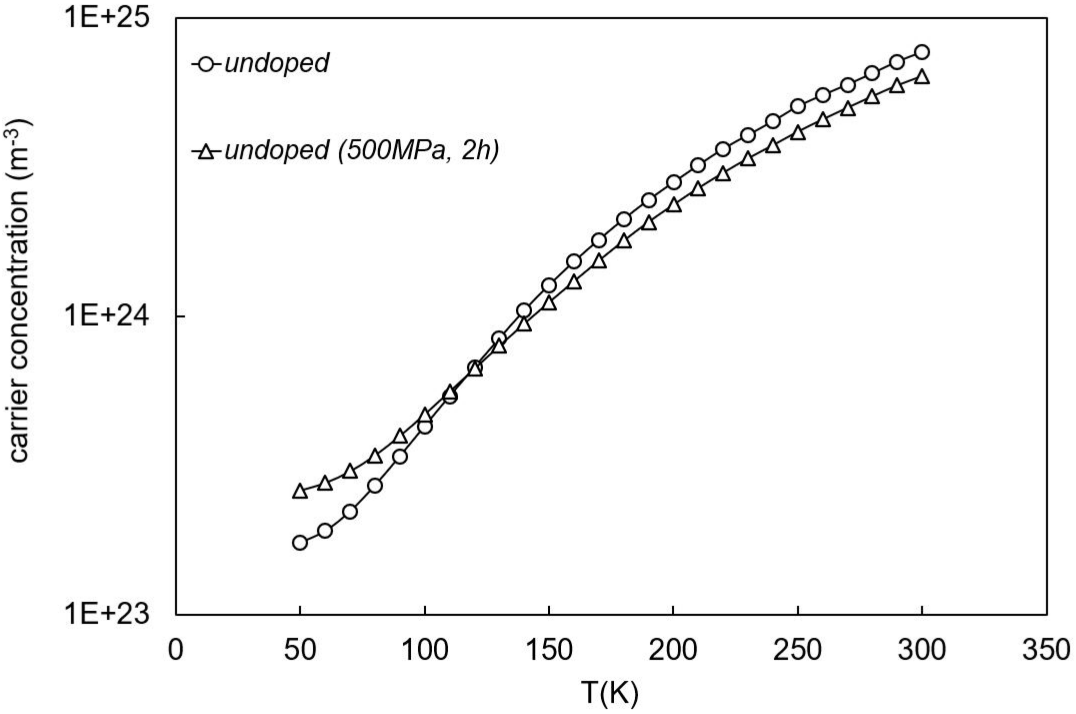

Figure 3.54: Carrier concentration of undoped post-high-pressure $Bi_{85}Sb_{15}$ sample

Post high-pressure effect in p-type Bi-Sb

The samples are not made using the HPLT method and the doping efficiency is not the key here. The resistivity, the Seebeck and the power factor of the p-type post high-pressure Bi-Sb samples are shown in Figure 3.55, Figure 3.56, and Figure 3.57. Because of the decreased electron mobility, the Seebeck increases and so the power factor. If we look at the Hall coefficient and the carrier concentration of the Ge2Pb1 samples in Figure 3.58 and Figure 3.59, we can find that the post high-pressure has little effect on the hole concentration at lower temperature. Moreover, the hole mobility is not affected much by the post high-pressure because the resistivity is not affected much by the post high-pressure. However, it shifts the transition temperature from p-type to n-type to higher temperature. The equation of the two channel Hall coefficient is written as:

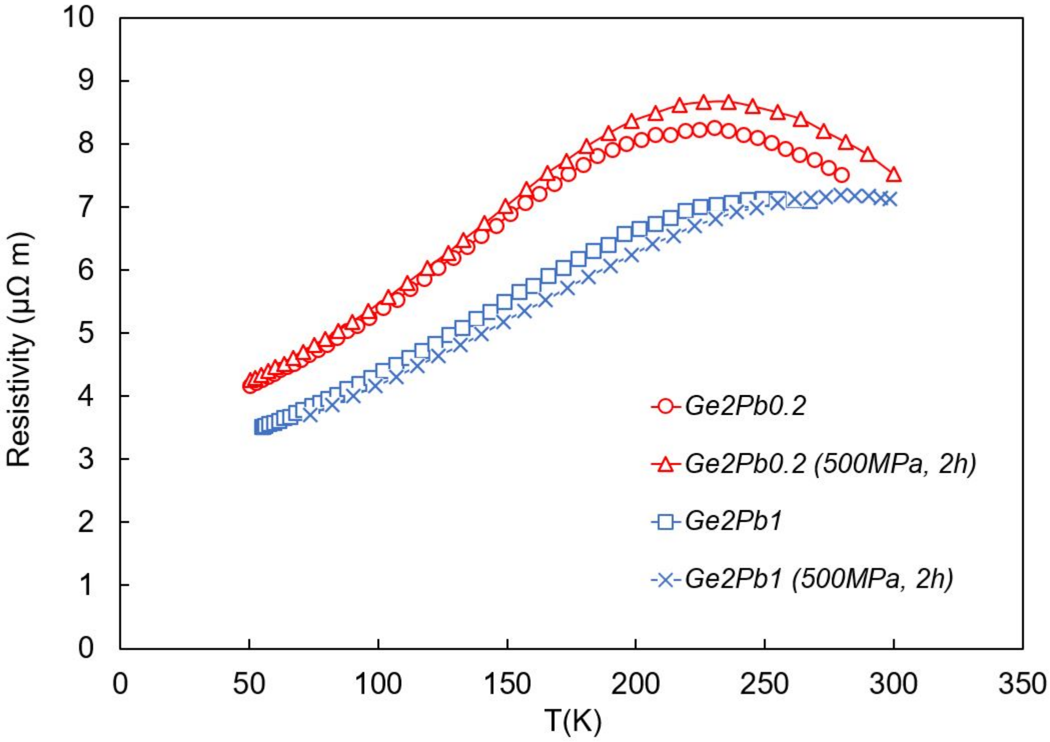

Figure 3.55: Resistivity of Ge+Pb codoped post-high-pressure $Bi_{85}Sb_{15}$ samples

$$R_H = \frac{(p\mu_p^2 - n\mu_n^2)}{e\,(p\mu_p + n\mu_n)^2} = \frac{p - nb^2}{e(p+nb)^2} \tag{3.3}$$

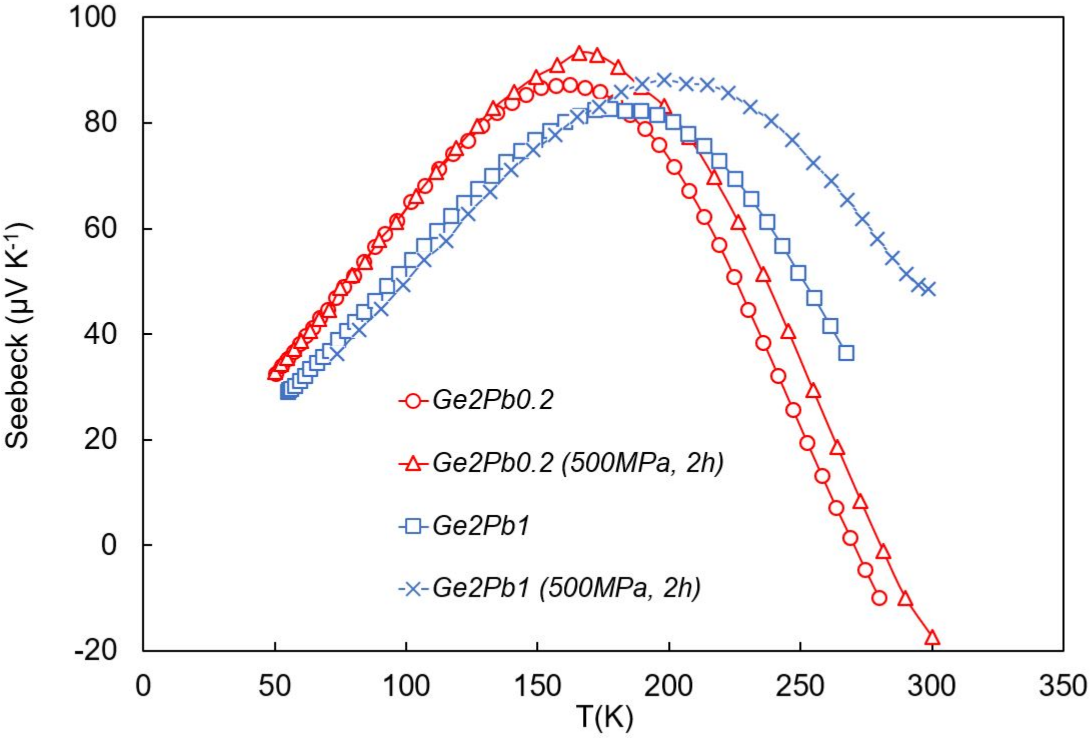

Figure 3.56: Seebeck of Ge+Pb codoped post-high-pressure $Bi_{85}Sb_{15}$ samples

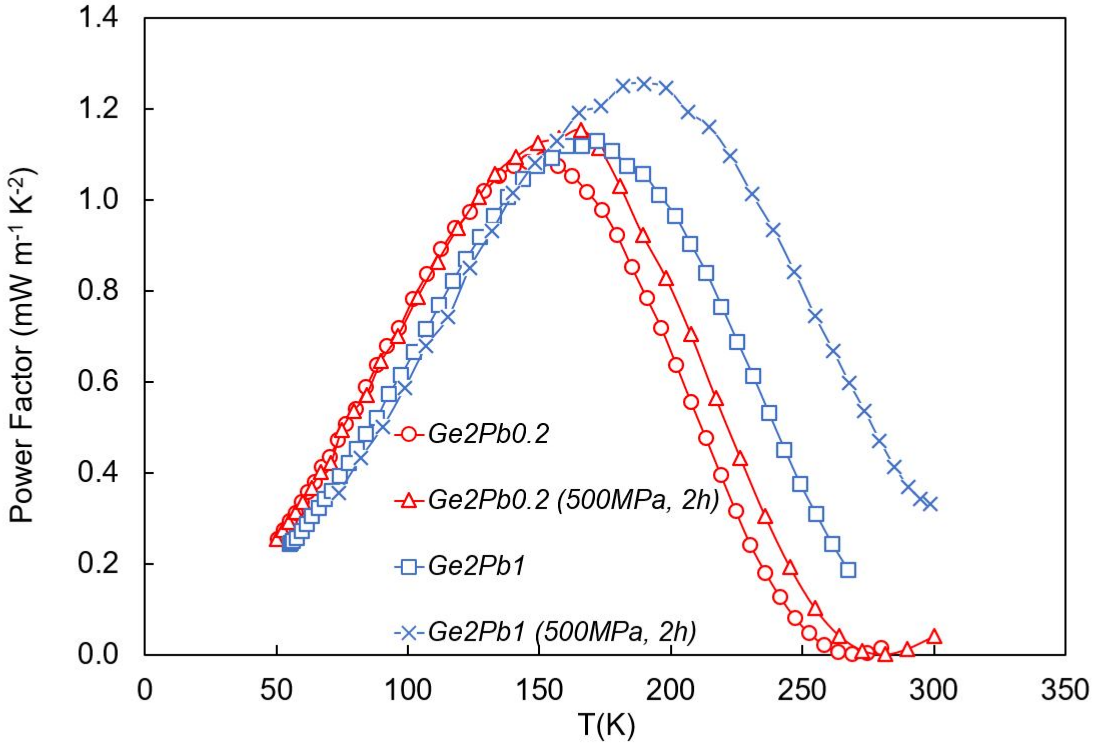

Figure 3.57: Power factor of Ge+Pb codoped post-high-pressure $Bi_{85}Sb_{15}$ samples

where n and μ_n are the electron concentration and the electron mobility, p and μ_p are the hole concentration and the hole mobility, and b is ratio of the electron mobility and the hole mobility $\frac{\mu_n}{\mu_p}$.

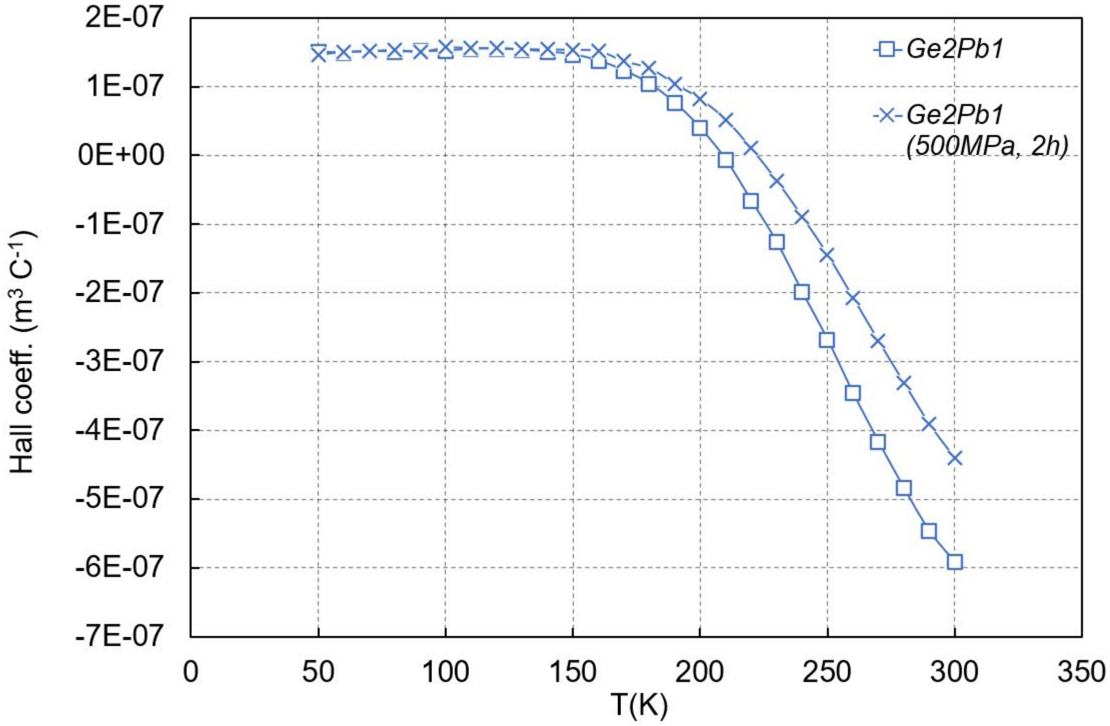

Figure 3.58: Hall coefficient of Ge2Pb1 codoped post-high-pressure $Bi_{85}Sb_{15}$ samples

Since we know that the post high-pressure increases the electron concentration, so the only explanation for the shift of the transition temperature is the decreased ratio of the electron mobility to the hole mobility b.

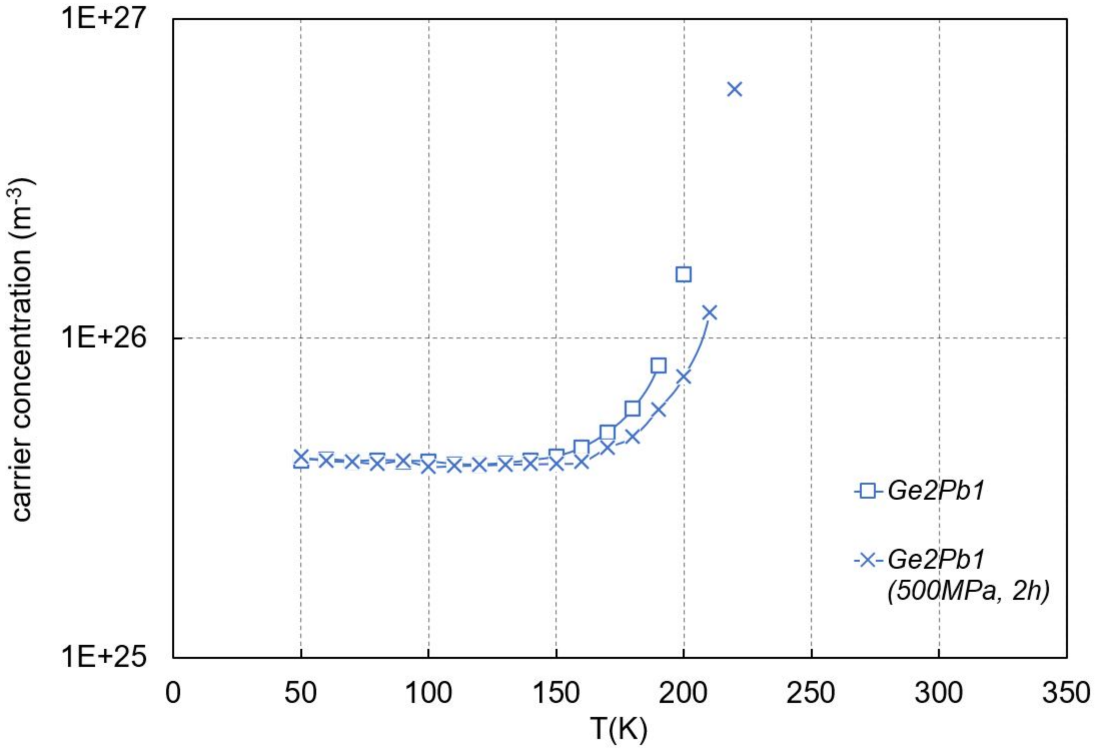

Figure 3.59: Carrier concentration of Ge2Pb1 codoped post-high-pressure $Bi_{85}Sb_{15}$ samples

3.4.5 Carrier mobility

We calculate the carrier mobility of the Bi-Sb samples at low temperature (50 K $\sim$ 60 K). The n-type results are shown in Table 3.3 while the p-type results are shown in Table 3.4.

We can clearly find that the hole mobility of the p-type samples is about two orders smaller than than the electron mobility of the undoped $Bi_{85}Sb_{15}$. This is due to the large difference between the effective masses of the conduction band and the valence band in Bi-Sb.

As we discussed in the previous sections, adding Ni/Te or apply the post high-pressure would decrease the electron mobility. This makes it possible to improve the TE properties of p-type Bi-Sb.

Continuously adding p-type dopants would decrease the hole mobility because of the increase of the scattering in the samples.

Sample	Carrier mobility $(cm^2V^{-1}s^{-1})$
undoped $Bi_{85}Sb_{15}$	20946 $(\sim 50K)$
$Bi_{85}Sb_{15}Ni_1$	2318 $(\sim 50K)$
$Bi_{85}Sb_{15}Te_{0.1}$	2044 $(\sim 50K)$
undoped $Bi_{85}Sb_{15}$ (500MPa, 2h)	14125 $(\sim 50K)$

Table 3.3: The carrier mobility comparison between n-type undoped $Bi_{85}Sb_{15}$, undoped $Bi_{85}Sb_{15}$ with post high-pressure, and Ni/Te doped $Bi_{85}Sb_{15}$

Sample	Carrier mobility $(cm^2V^{-1}s^{-1})$
$Bi_{85}Sb_{15}Ge_{0.5}$	335 $(\sim 50K)$
$Bi_{85}Sb_{15}Ge_5$	131 $(\sim 50K)$
$Bi_{85}Sb_{15}Sn_{0.5}$	643 $(\sim 50K)$
$Bi_{85}Sb_{15}Sn_5$	176 $(\sim 60K)$
$Bi_{85}Sb_{15}Pb_{0.1}$	1007 $(\sim 60K)$
$Bi_{85}Sb_{15}Pb_{0.5}$	289 $(\sim 60K)$

Table 3.4: The carrier mobility comparison between p-type Ge/Sn/Pb doped $Bi_{85}Sb_{15}$ samples

3.5 Power factor, thermal conductivity, and zT

We plot the highest power factor of the samples made using different strategies in Figure 3.60. It can be seen that the best three samples which have the highest power factor in the temperature range 150 K to 200 K are $Bi_{88}Sb_{12}Ni_1Pb_{0.5}$, $Bi_{85}Sb_{15}Ge_2Pb_1$ (500MPa, 2h) and $Bi_{85}Sb_{15}Ni_1Sn_{0.5}$. Although the sample $Bi_{85}Sb_{15}Ge_5Pb_1$ has a good power factor as $1.38\,mWm^{-1}K^{-2}$ at 250 K, it's not as good as the other samples below 200 K.

The thermal conductivity measured using the hot disk method is shown in Figure 3.61. We have used the value to calculate the figure of merit zT for $Bi_{85}Sb_{15}Ge_{15}Sn_{0.3}$ and $Bi_{88}Sb_{12}Ni_1Pb_{0.5}$.

The zT comparison has been made between our samples and several reference results [43], [44], [48], [50] in Figure 3.62. It can be seen that zT of $Bi_{85}Sb_{15}Ge_{15}Sn_{0.3}$ sample is significantly higher than the pure Ge ($Bi_{85}Sb_{13}Ge_2$) and pure Sn ($Bi_{88.5}Sb_{7.5}Sn_4$) doped polycrystalline results. zT of $Bi_{88}Sb_{12}Ni_1Pb_{0.5}$ is also larger than the reference $Bi_{85}Sb_{14}Pb_1$ result. It's better than the Sn doped single crystal result $Bi_{77.1}Sb_{22.9}Sn_{0.75}$ below 210 K.

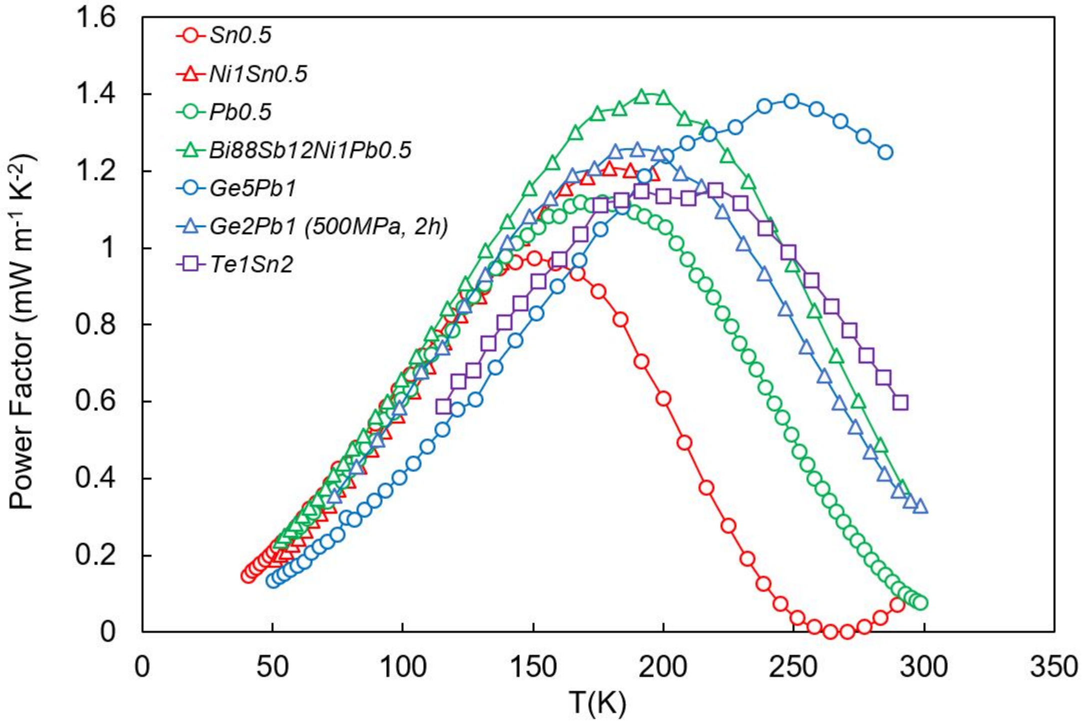

Figure 3.60: Power factor comparison between the p-type Bi-Sb samples made using different strategies.

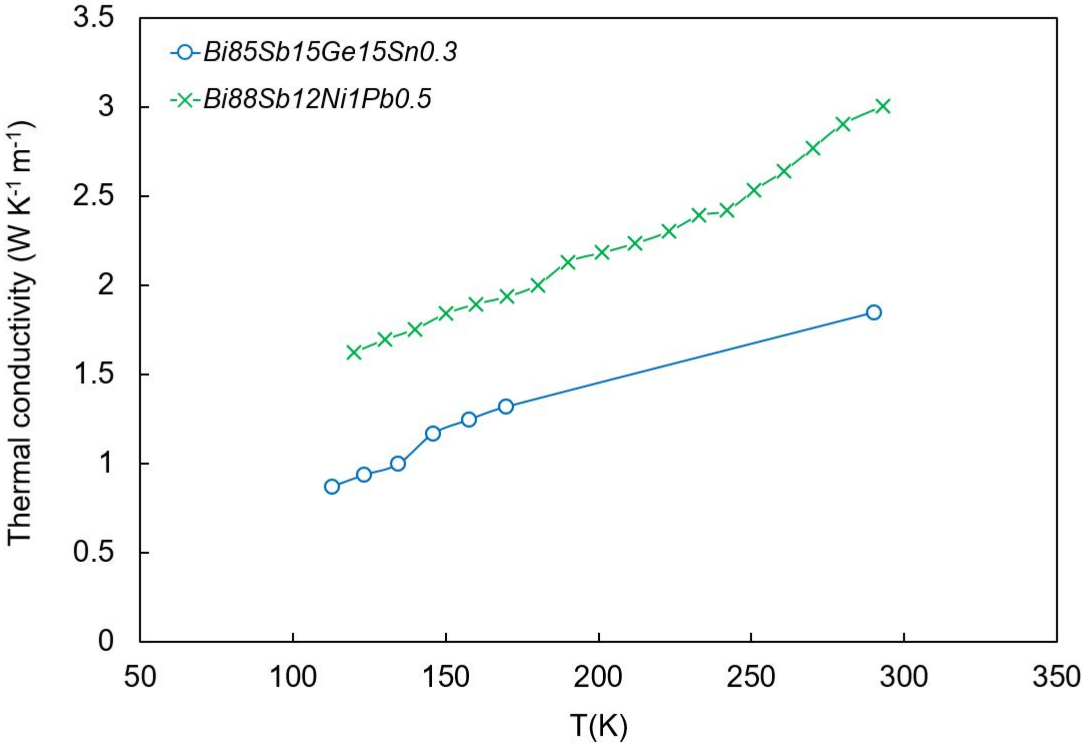

Figure 3.61: The thermal conductivity results of $Bi_{85}Sb_{15}Ge_{15}Sn_{0.3}$ and $Bi_{88}Sb_{12}$ $Ni_1Pb_{0.5}$ measured with hot disk method

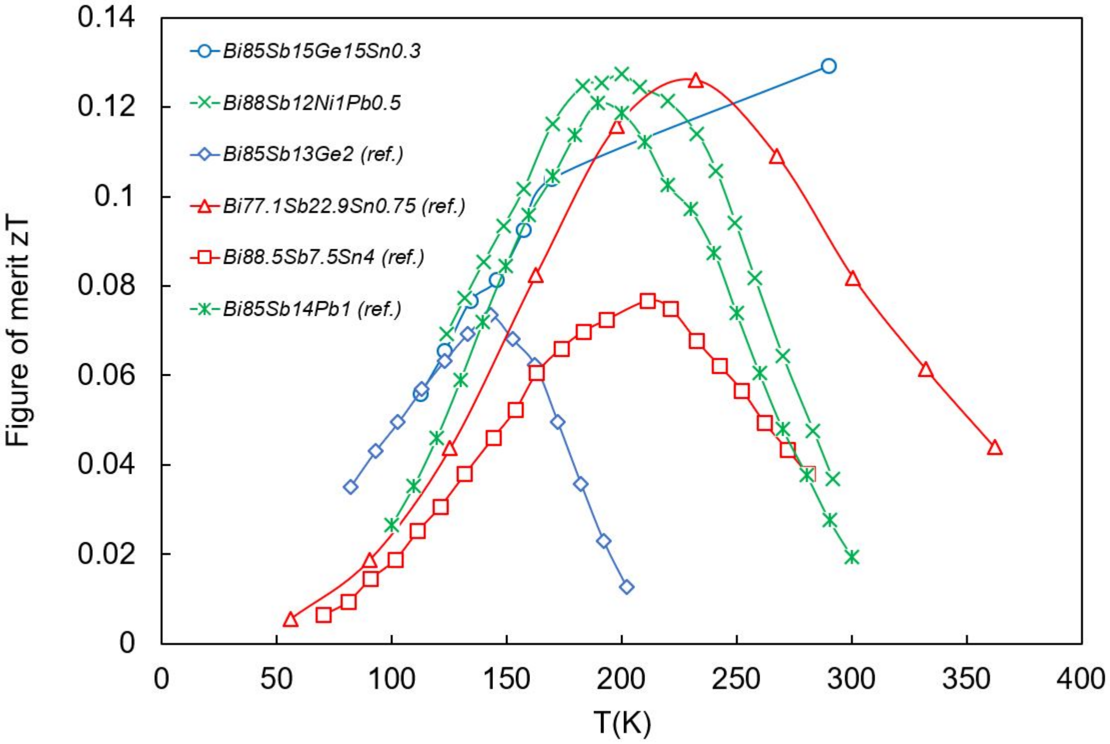

Figure 3.62: The figure of merit zT comparison with p-type Bi-Sb references

Compared with the zT of p-type $CsBi_4Te_6$ ($\sim$ 0.8 at 200 K) [54] and the zT of commercial p-type $Bi_{2-x}Sb_xTe_3$ ($\sim$ 0.5 at 200 K) [55], the zT of p-type Bi-Sb is not very competitive among p-type cryogenic thermoelectric materials.

Chapter 4

Modeling of the resistivity and the Seebeck coefficient of p-type Bi-Sb alloys

To better understand the thermoelectric properties of p-type Bi-Sb alloys, we apply an effective mass model to fit the resistivity and the Seebeck coefficient of pure Ge, Sn, and Pb doped Bi-Sb samples. A shrinking behavior of the band gap is extracted in the modeling process.

4.1 Modeling method

Starting with the calculation of electron and hole concentrations n and p, respectively, the charge neutrality is set as a constraint:

$$p + N_d^+ = n + N_a^- \tag{4.1}$$

where N_d^+, N_a^- are the concentrations of ionized donors and acceptors, respectively. $|n - p| = |N_d^+ - N_a^-|$ which can be estimated from the Hall coefficient data at low temperature. This number is assumed to be constant for each sample as temperature varies.

For the carrier concentrations,

$$n, p = \int D_{n,p}(E) f_{n,p}(E) dE \tag{4.2}$$

where $D(E) = \frac{1}{2\pi^2}\left(\frac{2m_d^*}{\hbar^2}\right)^{3/2}\sqrt{E}$ is the density of states, $f(E) = \frac{1}{1+exp\left(\frac{E-\mu}{k_B T}\right)}$ is the Fermi-Dirac distribution function, m_d^* is the total density of states effective mass and μ is the chemical potential.

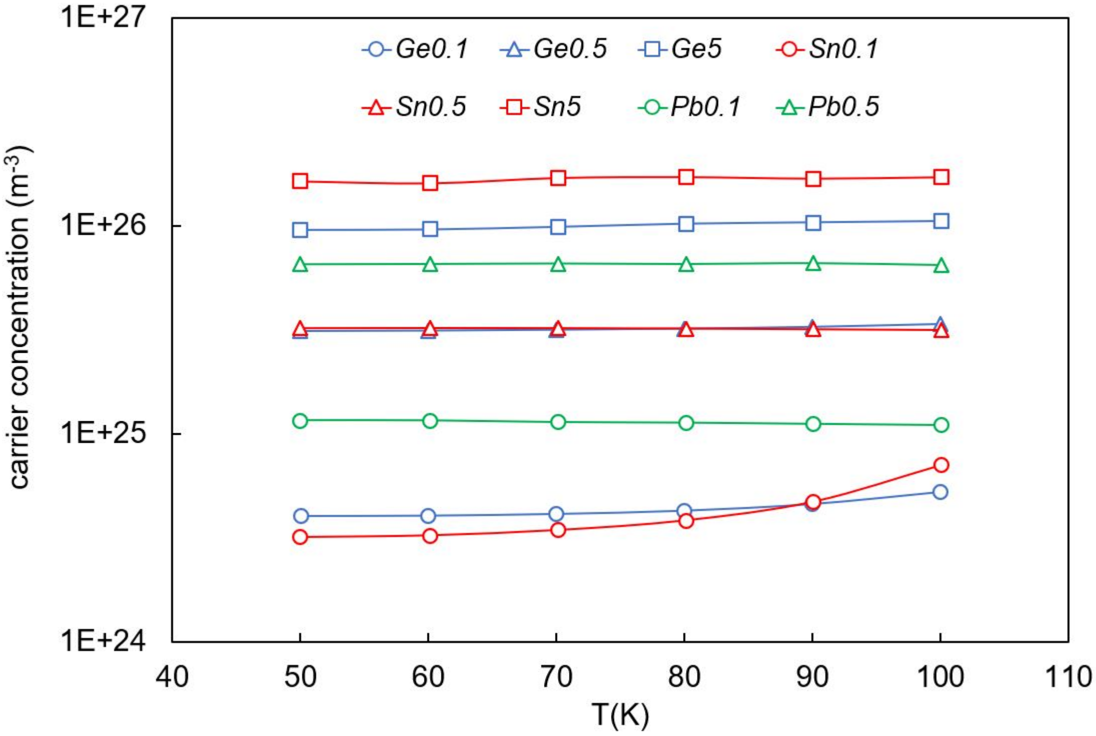

Figure 4.1: Hole concentration of Ge, Sn, and Pb doped $Bi_{85}Sb_{15}$ below 100 K

We use the low temperature hole concentration in p-type Bi-Sb as the known values for $|n-p| = |N_d^+ - N_a^-|$ in the calculation. Figure 4.1 shows the hole concentration for the samples that we choose to model the properties.

The electrical conductivity and the Seebeck coefficient are written as

$$\sigma = -\frac{2e^2}{3m_c^*}\int_0^\infty \frac{\partial f}{\partial E} D(E) E \tau dE \tag{4.3}$$

$$S = \frac{1}{eT}\frac{\int_0^\infty \frac{\partial f}{\partial E} D(E) E (E-\mu) \tau dE}{\int_0^\infty \frac{\partial f}{\partial E} D(E) E \tau dE} \tag{4.4}$$

where e is the unit charge, m_c^* is the conductivity effective mass, f is the Fermi-Dirac distribution function, μ is the chemical potential and τ is the scattering time.

In terms of determining the scattering time in the undoped $Bi_{85}Sb_{15}$, we calculate the mobility using the single band approximation in view of the electron dominated transport. The mobility is found to be roughly proportional to $T^{1.5}$ at low temperature ($<$ 100 K) and $T^{-1.5}$ at high temperature ($>$ 100 K). Thus, we apply the Matthiessen's rule below to calculate the total scattering rate $\frac{1}{\tau_{total}}$.

$$\frac{1}{\tau_{total}} = \frac{1}{\tau_{acoustic}} + \frac{1}{\tau_{impurity}} \tag{4.5}$$

The first term $\frac{1}{\tau_{acoustic}}$, acoustic deformation potential (ADP) scattering, is known to be the dominant scattering mechanism at relatively high temperature and leads to a mobility trend as $T^{-1.5}$. It can be described by using the following equation [56]:

$$\frac{1}{\tau_{acoustic}} = \frac{\pi \epsilon_{ac}^2 k_B T}{\hbar c_l} g(E) \tag{4.6}$$

where ϵ_{ac} is the acoustic deformation potential, c_l is the longitudinal elastic constant, $g(E) = \frac{1}{2\pi^2}\left(\frac{2m_b^*}{\hbar^2}\right)^{3/2}\sqrt{E}$, $m_b^* = \frac{m_d^*}{N_v^{2/3}}$ is the density of states effective mass of a single valley and N_v is the number of valleys in the Fermi surfaces.

The defect impurity scattering time has the form $\tau_{impurity} = \tau_0 \left(E/k_B T\right)^{3/2}$, where τ_0 is constant. It leads to a mobility trend as $T^{1.5}$ [56]. As a result, the total scattering rate $\frac{1}{\tau_{total}}$ can be written as

$$\frac{1}{\tau_{total}} = \frac{\pi \epsilon_{ac}^2 k_B T}{\hbar c_l} g(E) + \frac{1}{\tau_0 \left(E/k_B T\right)^{3/2}} = A \cdot T\sqrt{E} + B \cdot \left(\frac{E}{T}\right)^{-3/2} \tag{4.7}$$

where A and B are constants and can be determined in the fitting process. The same scattering mechanisms are applied to the electron-channel and the hole-channel calculations.

For p-type Bi-Sb samples, which are essentially semi-metallic, the mobility trend reveals the dominance of the acoustic deformation potential (ADP) scattering even at low temperatures. The apparent absence of the ionized impurity scattering in p-type samples is the result of high dopant concentration which makes the average distance between dopant atoms small and on average, the motion of the charge carriers (electrons and holes) will not be affected much by the dopant ions.

As we discussed in Chapter 3, below 7% antimony, the alloy behaves as a semimetal. As the antimony content is increased to 7% $\sim$ 22%, a gap opens between the L_a band and T band and the alloy becomes a semiconductor. This is a result of the inversion of L_a and L_s bands, which occurs at 4% antimony. In the semiconductor region, the L_s band becomes a direct hole band, while the T and H bands act as indirect hole bands. Once the antimony content is larger than 22%, the alloy returns to the semi-metallic state.

For the composition $Bi_{85}Sb_{15}$, L_a, L_s and H bands are the conduction band, direct light valence band, and indirect heavy valence band, respectively. Due to the low density-of-states effective mass of the L_s band [41], it makes little contribution to the TE transport properties compared to the H band. Therefore, the L_a band and H band are used as the conduction band and valence band in the modeling.

Considering the two channels together, the resistivity ρ and the Seebeck coefficient S_{total} can be written as

$$\rho = \frac{1}{\sigma_n + \sigma_p} + \rho_R \tag{4.8}$$

$$S_{total} = \frac{\sigma_n S_n + \sigma_p S_p}{\sigma_n + \sigma_p} \tag{4.9}$$

where ρ_R is the residual resistivity, σ_n and σ_p are the electrical conductivity components of the electron and the hole channel, and S_n and S_p are the Seebeck components of the electron and the hole channel, respectively. Detailed equations for calculating the effective mass, the longitudinal elastic constant, the carrier concentration, the electrical conductivity and the Seebeck coefficient can be found in the appendix. The modeling parameters for undoped $Bi_{85}Sb_{15}$ are listed in Table 4.1.

Parameters	Electrons	Holes
$m_d^*\,(m_e)$	0.203	0.483
$m_c^*\,(m_e)$	0.025	0.084
N_v	3	6
$c_l\,(N\,m^{-2})$	6.6×10^{10}	6.6×10^{10}

Table 4.1: The parameters in the modeling of undoped $Bi_{85}Sb_{15}$

In the modeling of p-type samples, the electron effective masses are the same as the undoped sample. The hole effective mass ($m_{d,p}^*$, $m_{c,p}^*$) and the acoustic deformation potential (ϵ_{ac}) are used as the fitting parameters and listed in Table 4.2. The hole effective masses are found to be larger than those for undoped Bi-Sb. The enhancement of the hole effective masses can be attributed to the presence of the impurity band in the narrow-gap ($\sim$ 20 meV) region.

Samples	$m_{d,p}^*\,(m_e)$	$m_{c,p}^*\,(m_e)$	ϵ_{ac} (eV)
Ge0.5	1.264	0.2	19
Ge5	1.39	0.109	24
Sn0.5	0.755	0.2	20
Sn5	1.492	0.133	20
Pb0.1	0.701	0.2	19
Pb0.5	1.209	0.15	23

Table 4.2: The parameters in the modeling of doped $Bi_{85}Sb_{15}(Ge, Sn, Pb)_x$

The deformation potential of undoped $Bi_{85}Sb_{15}$ above 100 K and doped $Bi_{85}Sb_{15}(Ge, Sn, Pb)_x$ are close to the value of the deformation potential (18 eV) of undoped $Bi_{90}Sb_{10}$ [57]. It is worth noting that the band gap plays an important role in Equation 4.2, Equation 4.8, and Equation 4.9 as it affects the relative positions between the chemical potential μ and the conduction band minimum or the valence band maximum. Calculations of the carrier concentration, the electrical conductivity and the Seebeck coefficient all depend on that. In order to fully fit the undoped and doped $Bi_{85}Sb_{15}(Ge, Sn, Pb)_x$ samples, a temperature dependent band gap is used.

4.2 Plots of the modeled TE transport properties in comparison with the measurement data, and the Pisarenko's plot of Ge-, Sn-, and Pb-doped $Bi_{85}Sb_{15}$ samples

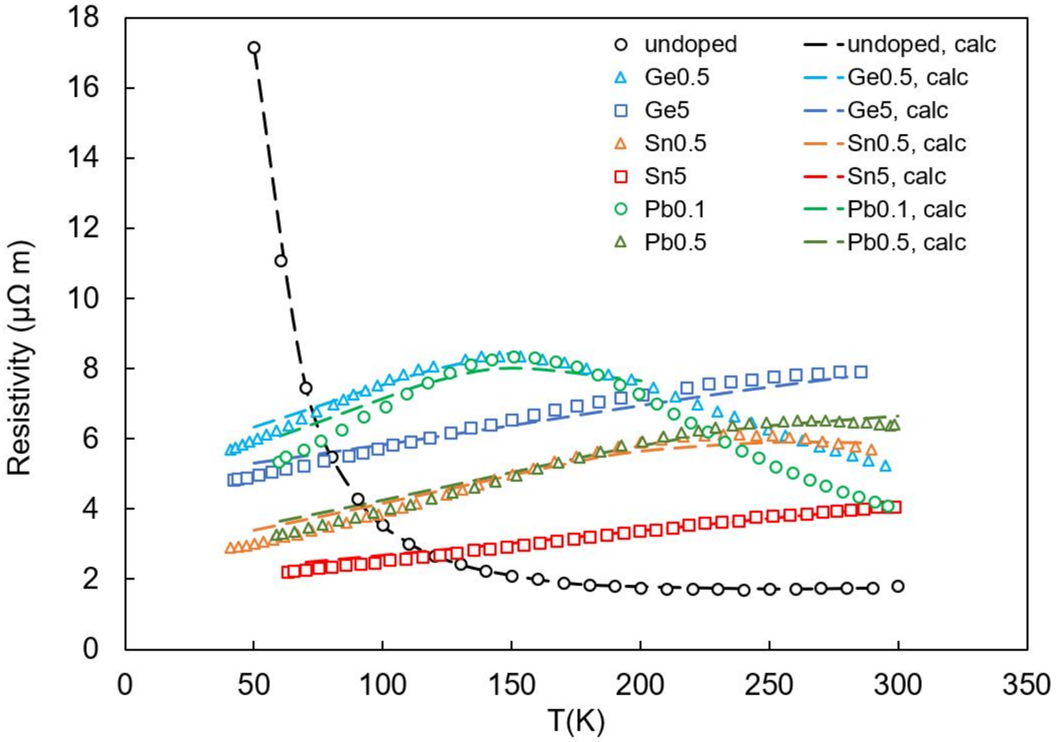

Figure 4.2: Comparison between the modeled and the experimental resistivity of Bi-Sb samples

The modeled results are compared with the experimental results in Figure 4.2 and Figure 4.3. The discrete points are the experimental data. The dashed lines are the fitting results.

Based on the following equation derived from a single parabolic band model,

$$S = \frac{8\pi^2 k_B^2}{3eh^2} m_d^* T \left(\frac{\pi}{3p}\right)^{2/3} (1 + \lambda_\tau) \tag{4.10}$$

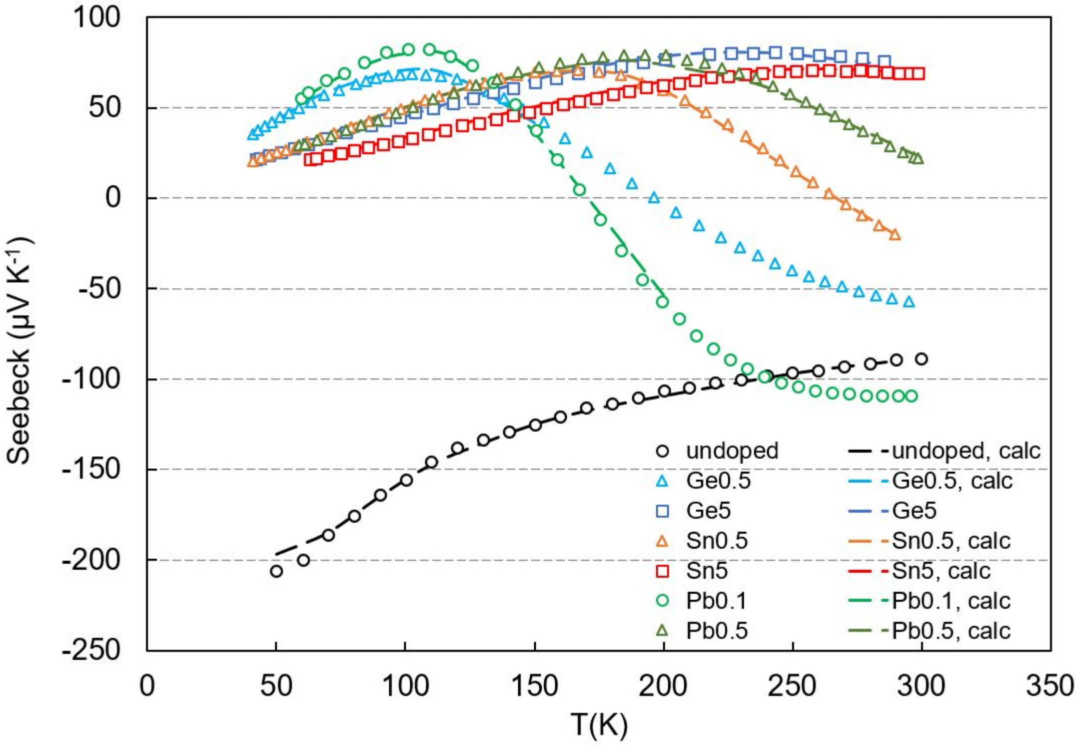

Figure 4.3: Comparison between the modeled and the experimental Seebeck coefficient of Bi-Sb samples

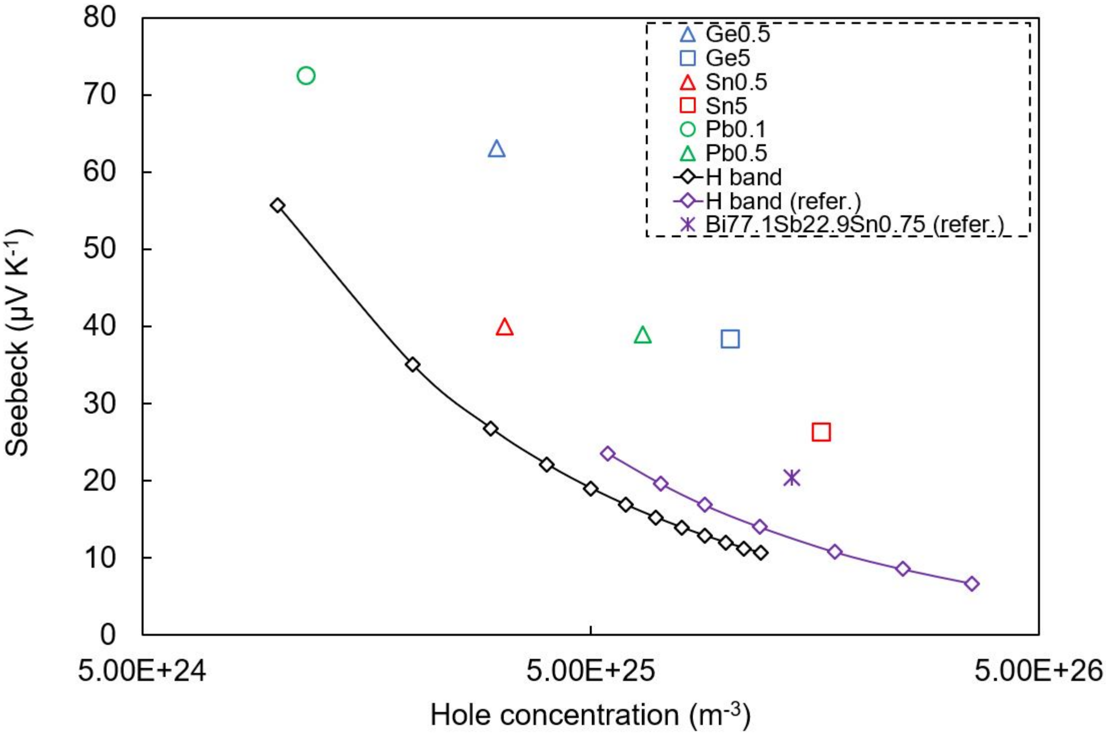

Figure 4.4: Pisarenko's plot of p-type Bi-Sb

we have made the Pisarenko's plot in Figure 4.4. λ_τ is a parameter which is related to the scattering mechanisms (in ADP scattering approximation, $\lambda_\tau = 0$) [58]. Our results together with the results in the work [43] (purple points and line in Figure 4.4) appear to follow a certain trend. All the data points are seen to lie above the H band lines. Furthermore, the data points of Ge-, Sn- and Pb-doped samples are scattered between each other which indicates the different changes of the hole effective masses for Ge-, Sn- and Pb-doped samples.

4.3 Band gap shrinking

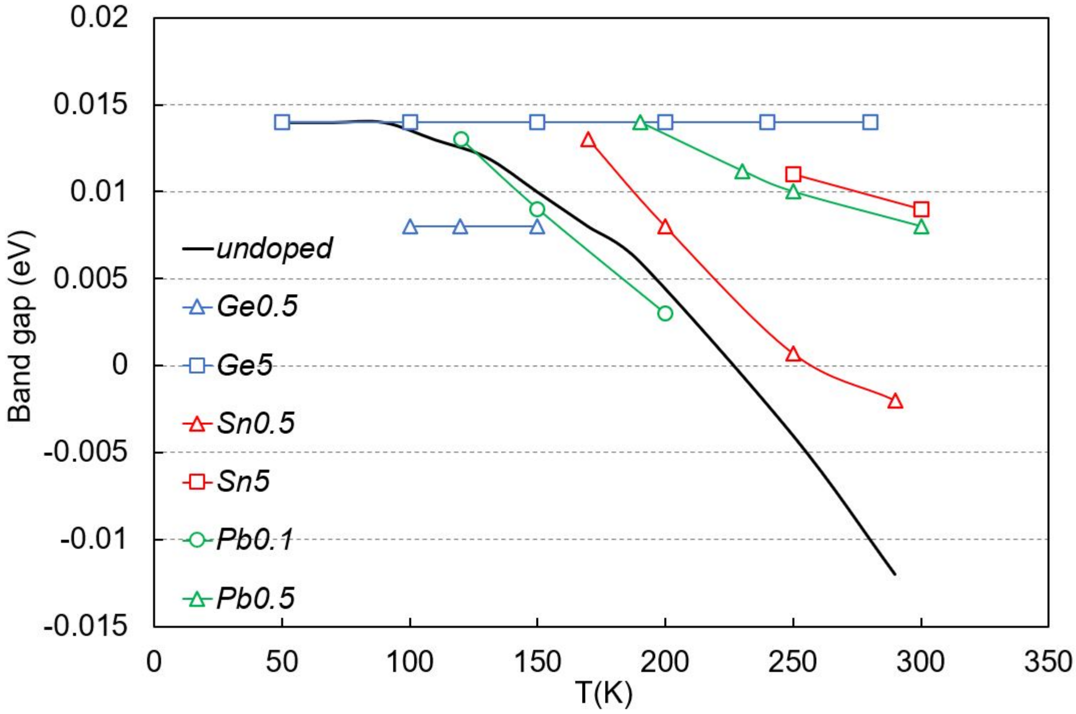

Figure 4.5: Band gap shrinking in Bi-Sb samples

Previous studies of $Bi_{85}Sb_{15}$ alloys reported a band gap (E_g) in the range of 10 ∼ 24 meV [34], [37], [42], [52]. Given the large variation of E_g, we use E_g as a fitting parameter in the modeling. Our result shows band gap to have a temperature dependence both for the undoped and doped samples. The gap is found to shrink in size at increasing temperature, even reaching zero at certain threshold temperatures, as shown in Figure 4.5.

The decreasing of the band gap can be explained by the band edge movement at the L-point for Bi-Sb alloys: the L_a band is found to move down as temperature increases [59]. The impurity band created by adding Ge/Sn/Pb also plays a role here since band gap decreasing is also noted in our doped samples. Besides, it is reported that the undoped Bi-Sb alloy shows lattice deformation at around 150 K $\sim$ 200 K [60], which might lead to the change in its band gap. The decreasing of the band gap is clearly an obstacle when pursuing good TE properties of p-type Bi-Sb. It is known that the hole Seebeck coefficient is low in comparison with the electron thermopower in Bi-Sb alloys due to the mobility difference between electrons and holes. Bipolar effect (see Equation 4.11) associated with the gap-decreasing would further undermine the figure of merit zT of the hole-doped samples.

The bipolar thermal conductivity is written as:

$$\kappa_{bipolar} = \frac{\sigma_n \sigma_p}{\sigma_n + \sigma_p} \left(S_n - S_p\right)^2 T \tag{4.11}$$

where σ_n and σ_p are the electrical conductivity of the electron channel and the hole channel, S_n and S_p are the Seebeck coefficient of the electron channel and the hole channel. S_n is negative while S_p is positive. When both the electron channel and the hole channel participate in the transport, the bipolar thermal conductivity tends to be larger which increases the total thermal conductivity of the sample.

Chapter 5

Resistivity and Seebeck coefficient study on p-type Si-Ge alloys

Si-Ge alloys have decent thermoelectric properties at high temperature. It has been utilized to build the radioisotope thermoelectric generators (RTGs) for deep space missions by NASA [8]. For several decades, the thermoelectric performance of Si-Ge alloy hasn't improved much. It stays about the same as the one used on RTGs since 1976. The breakthrough on Si-Ge happened about 10 years ago [11], [12]. Researchers successfully enhanced the figure of merit zT by applying the nano-structure idea on Si-Ge alloys to decrease the thermal conductivity.

5.1 P-type Si-Ge related research

The following discussion will be focused on p-type Si-Ge in particular.

With the help of the mechanical alloy method – ball milling, and the hot-pressing technique, the zT of p-type Si-Ge is enhanced from 0.65 to 0.95 around 900 $\sim$ 950 °C [12] where $zT = 0.65$ is the referenced value of the Si-Ge alloy used on RTGs. It is found that the grain size of the alloy ranges from 5 $\sim$ 50 nm. The small grain size leads to more interfaces distributed in the alloy. As a result, the increased phonon scattering at the interfaces, such as the grain boundaries, leads to a low thermal conductivity ($\sim 2.5\ WK^{-1}m^{-1}$ in the temperature range $50 \sim 900$ °C). Since the grain size doesn't affect much of the power factor, the figure of merit zT is benefited from the low thermal conductivity overall. Later on, researchers in the same group apply a modulation-doping method to enhance the power factor of the p-type boron doped Si-Ge [61]. With the separation of the charge carriers and the impurity atoms in a two-phase composite ($Si_{80}Ge_{20} + Si_{100}B_5$), the carrier mobility can be enhanced due to the decrease of the impurity scattering. That leads to a higher electrical conductivity and also a higher power factor (~ 40 % increase compared to the power factor of the alloy made using the uniform doping with the same composition). As a result, the figure of merit zT of the modulation-doping sample is about the same as the uniform-doping sample. However, the factors that lead to the enhancement of the zT compared to the RTG SiGe sample are different for those two approaches. For the modulation-doping method, the major factor is the enhanced power factor. For the case of uniform-doping, the major factor is the decreased thermal conductivity.

People have added Au into p-type Si-Ge to form $Si_{0.62}Ge_{0.31}B_{0.03}Au_{0.04}$ and enhanced the zT to 1.6 around 1000 K [62]. The increase of zT can be attributed to the large Seebeck coefficient of 464 $\mu V/K$ which may be caused by the sharp peak in the density of states consisting the 5d states of Au, and the low thermal conductivity due to the phonon scattering at grain boundaries. Moreover, there are first-principle calculations on the transition metals' doping effects in Si-Ge alloys [63]. It shows that the Seebeck coefficient can be enhanced with the transition metal elements.

The band gap E_g (eV) of $Si_{1-x}Ge_x$ can be calculated using the following formula when $x < 0.85$ [64]:

$$E_g = 1.12 - 0.41x + 0.008x^2 \tag{5.1}$$

The result is approximately 1.04 eV for $Si_{0.8}Ge_{0.2}$ which is the basic composition that we make during the research. Since this band gap value is relatively large, the rising temperature cannot effectively excite enough electrons to the conduction band in p-type Si-Ge alloys. We can treat this system using the single band model.

Following the nano-structure and the nano-composite ideas, the first-principle calculations, and the experimental methods, we have studied several different particles' effects in p-type Si-Ge alloys.

5.2 Transition metal Fe/Ni codoped p-type Si-Ge

The resistivity and the Seebeck results of the Fe/Ni transition metal codoped p-type Si-Ge are shown in Figure 5.1 and Figure 5.2. The red lines are the results of the normal boron doped p-type Si-Ge that we make and set as a benchmark. The black lines show the referenced results of p-type Si-Ge [12]. We keep the referenced results in all the plots in this chapter to make comparison with our samples. The blue lines and green lines are the results of Fe and Ni codoped p-type Si-Ge, respectively. Compared with the referenced results, our samples show a lower resistivity and a lower Seebeck.

In the whole temperature range that we measure, the resistivity and the Seebeck of the samples show the linear metallic behaviors. Adding Fe decreases the resistivity of the samples while the Seebeck keeps roughly the same. Adding Ni increases both the resistivity and Seebeck of the samples. Adding transition metal particles into the system should decrease the carrier mobility by increasing the carrier scattering. So, adding Fe particles into p-type Si-Ge should help increase the hole concentration to cancel out the effect of the decreased carrier mobility and leads to the decrease of the resistivity. Besides, we can find a saturation effect in the Fe codoped samples. The resistivity and Seebeck curves of $Si_{78}Ge_{20}B_2Fe_1$ sample are almost the same as the curves of $Si_{78}Ge_{20}B_2Fe_2$. This indicates that the codoping of Fe is not very effective in p-type Si-Ge. For the case of Ni, we find

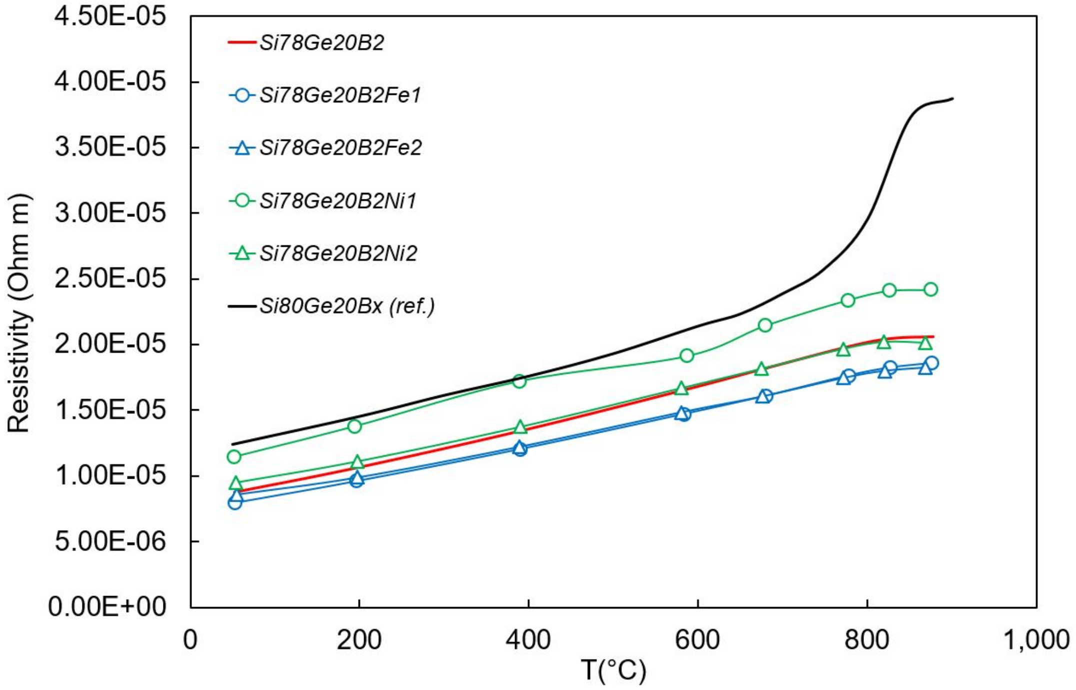

Figure 5.1: Resistivity of $Si_{78}Ge_{20}B_2$ samples codoped with Fe/Ni

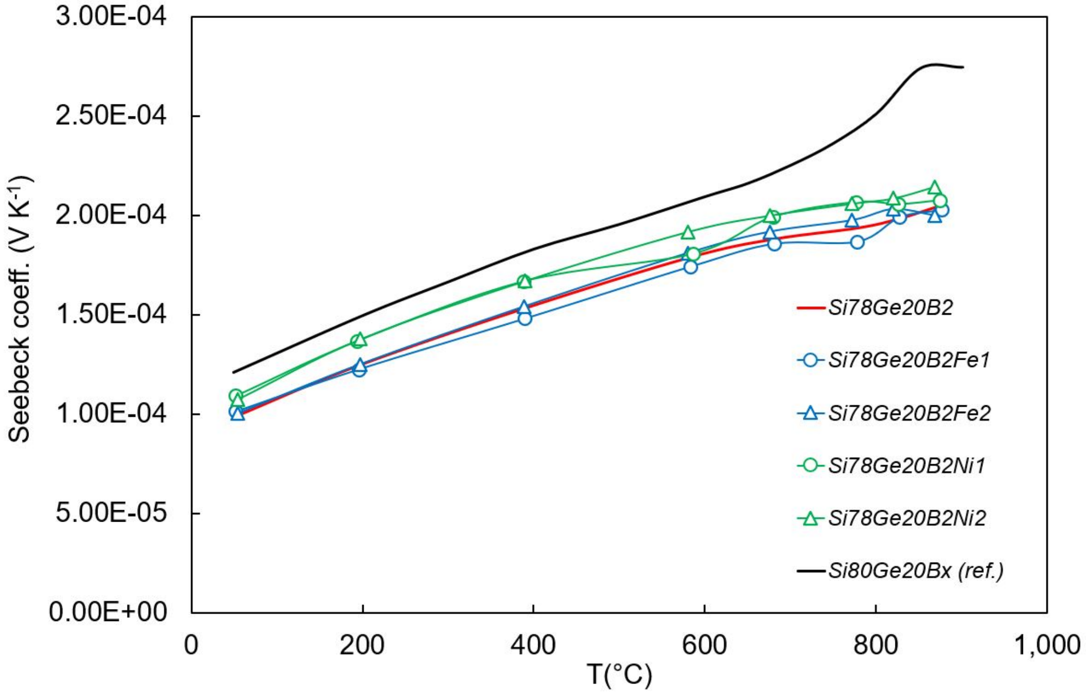

Figure 5.2: Seebeck coefficient of $Si_{78}Ge_{20}B_2$ samples codoped with Fe/Ni

that the resistivity increases first for $Si_{78}Ge_{20}B_2Ni_1$ sample and then decreases as we increase the Ni content to get $Si_{78}Ge_{20}B_2Ni_2$ sample. Compared with Fe, Ni particles have a stronger scattering effect in p-type Si-Ge samples which leads to a lower carrier mobility. Similar to Fe, adding Ni can increase the hole concentration, so that the resistivity of $Si_{78}Ge_{20}B_2Ni_2$ sample can be lower than $Si_{78}Ge_{20}B_2Ni_1$ sample.

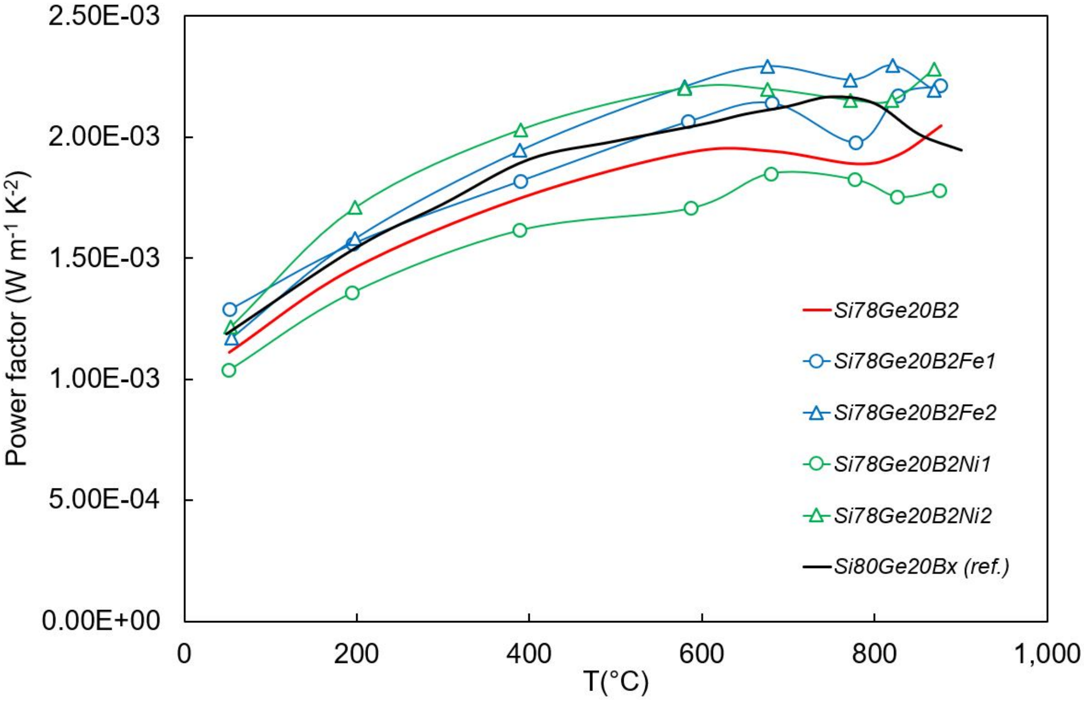

Figure 5.3: Power factor of $Si_{78}Ge_{20}B_2$ samples codoped with Fe/Ni

The power factor results are shown in Figure 5.3. The power factor of the $Si_{78}Ge_{20}B_2Fe_2$ sample gets some enhancement due to its lower resistivity. The power factor of the $Si_{78}Ge_{20}B_2Ni_2$ sample improves because of its higher Seebeck. Overall, we get about 10 % enhancement of the power factor of the Fe/Ni codoped p-type Si-Ge samples in the temperature range 500∼900 °C compared with the referenced values.

5.3 P-type Si-Ge embedded with aerogel particles

Figure 5.4, Figure 5.5, and Figure 5.6 show the results of p-type Si-Ge samples embedded with aerogel particles. Interestingly, adding aerogel particles into the system can decrease the resistivity. The aerogel is made of silica and we expected that it would increase the resistivity of Si-Ge samples since silica has poor electrical conductivity.

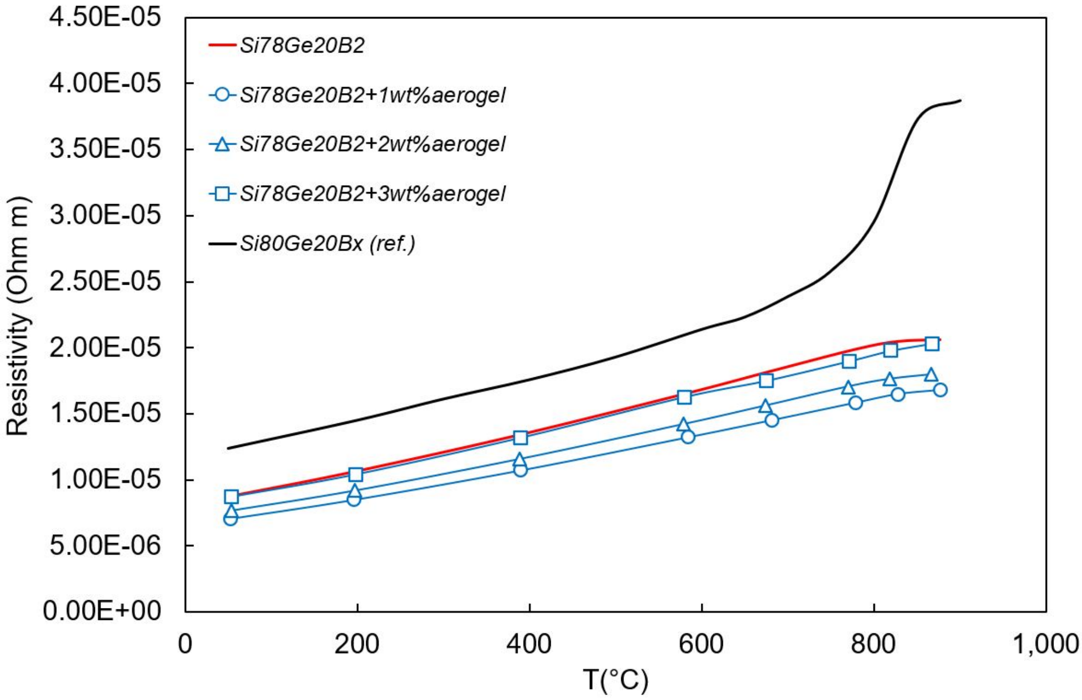

Figure 5.4: Resistivity of $Si_{78}Ge_{20}B_2$ samples embedded with aerogel particles

The 1 $wt\%$ aerogel embedded sample shows the lowest resistivity. As we increase the aerogel content, the resistivity increases which matches our original expectation. Adding aerogel should increase the doping efficiency of boron in Si-Ge to account for the lowered resistivity values. The Seebeck trends follow the similar trends as the resistivity. Overall, the power factor curves of the aerogel embedded p-type Si-Ge samples are a little higher than the result of the benchmark sample and close to the referenced p-type Si-Ge result.

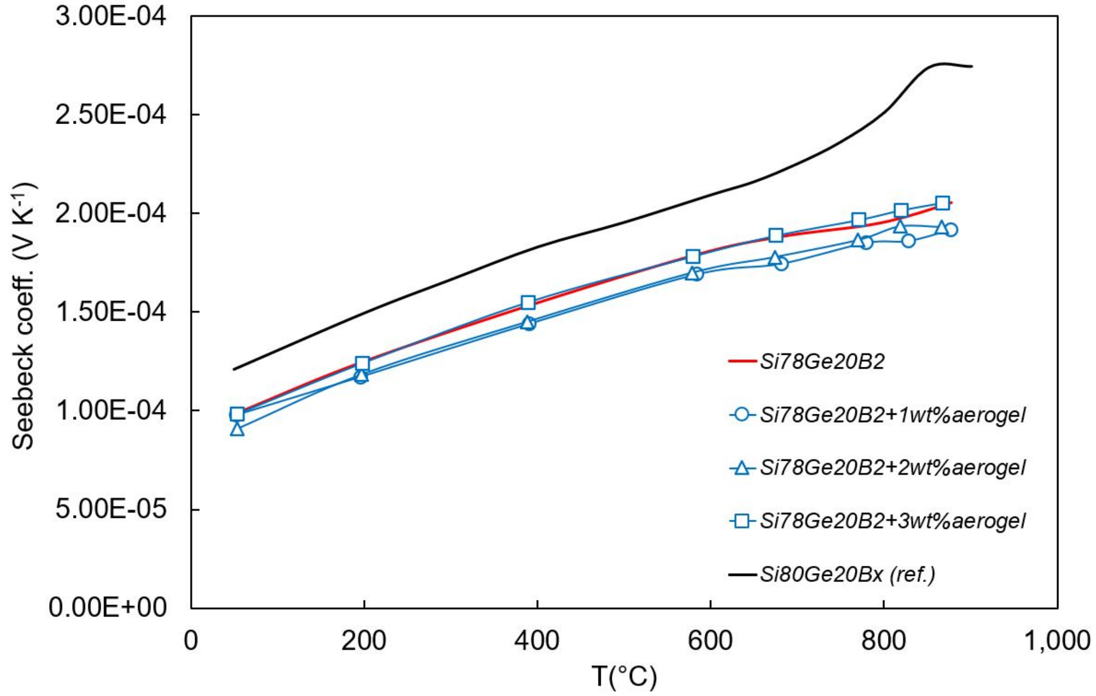

Figure 5.5: Seebeck coefficient of $Si_{78}Ge_{20}B_2$ samples embedded with aerogel particles

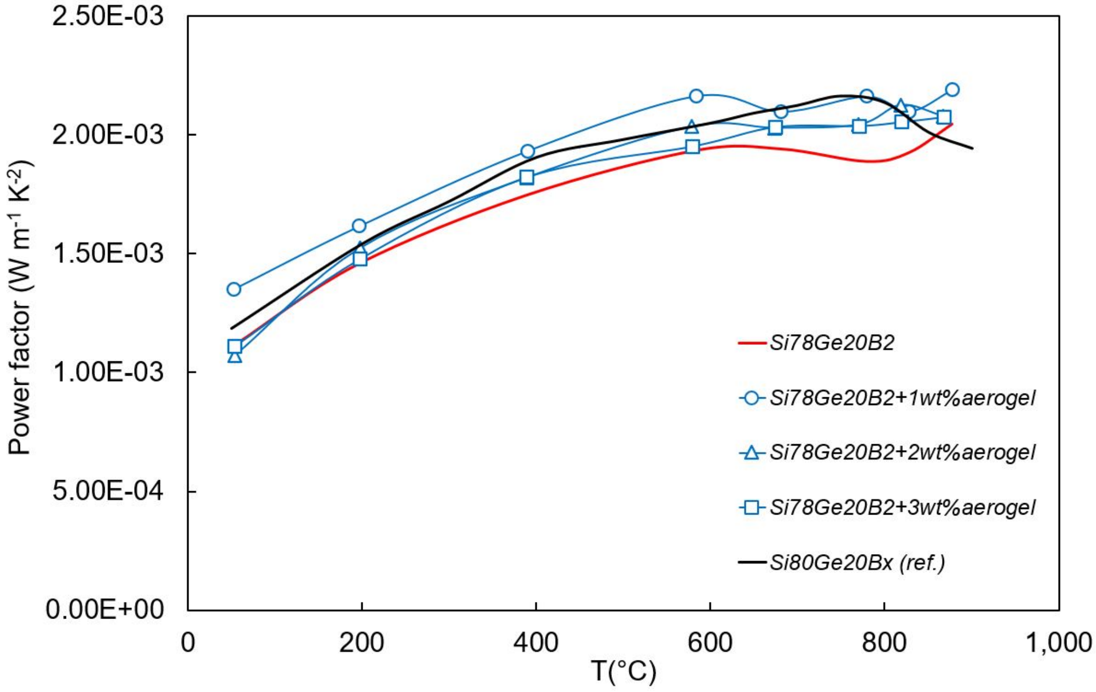

Figure 5.6: Power factor of $Si_{78}Ge_{20}B_2$ samples embedded with aerogel particles

5.4 Mo codoped p-type Si-Ge, and Si-Mo doped with boron

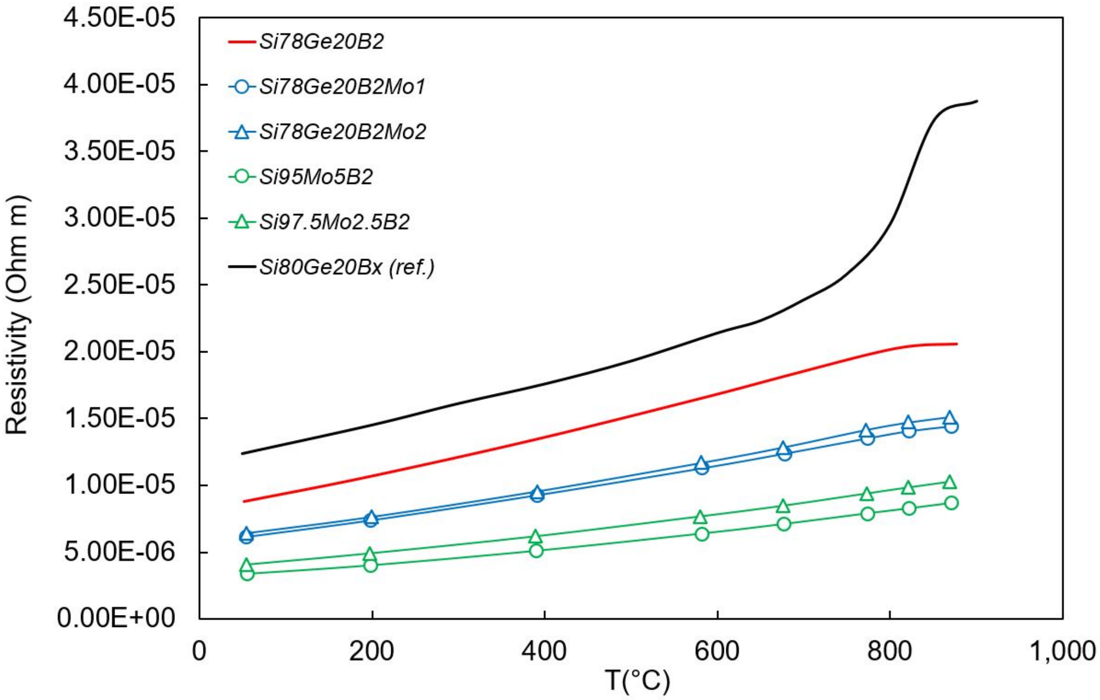

Figure 5.7: Resistivity of $Si_{78}Ge_{20}B_2$ samples codoped with Mo, and $SiMoB$ samples

Figure 5.7, Figure 5.8, and Figure 5.9 show the results of Mo codoped p-type Si-Ge, and Si-Mo samples doped with boron. Compared with the benchmark Si-Ge sample, the Mo codoped samples (blue lines) show the significantly lower resistivity and Seebeck values. Also, the saturation behavior of adding Mo can be observed as the differences between the properties of $Si_{78}Ge_{20}B_2Mo_1$ and $Si_{78}Ge_{20}B_2Mo_2$ are small. We are interested in why adding Mo can cause such an effective decrease on the resistivity in Si-Ge samples. Noticing that Si and Mo may form a second phase in Mo codoped p-type Si-Ge, we make Si-Mo samples doped with boron and measure the resistivity and the Seebeck. The $Si_{95}Mo_5B_2$ and $Si_{97.5}Mo_{2.5}B_2$ samples show the much lower resistivity values than the benchmark Si-Ge sample. The second phase of Si-Mo in Mo codoped Si-Ge samples may be the reason that causes the decrease of the resistivity.

In the power factor plot, the Mo codoped p-type Si-Ge samples have close

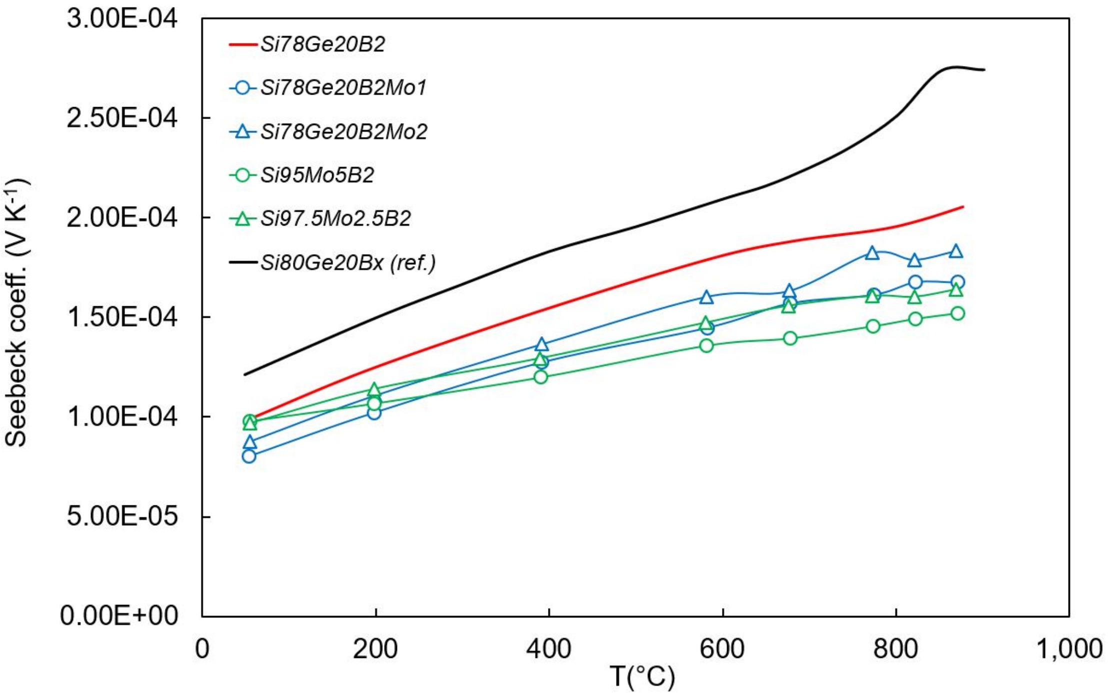

Figure 5.8: Seebeck coefficient of $Si_{78}Ge_{20}B_2$ samples codoped with Mo, and $SiMoB$ samples

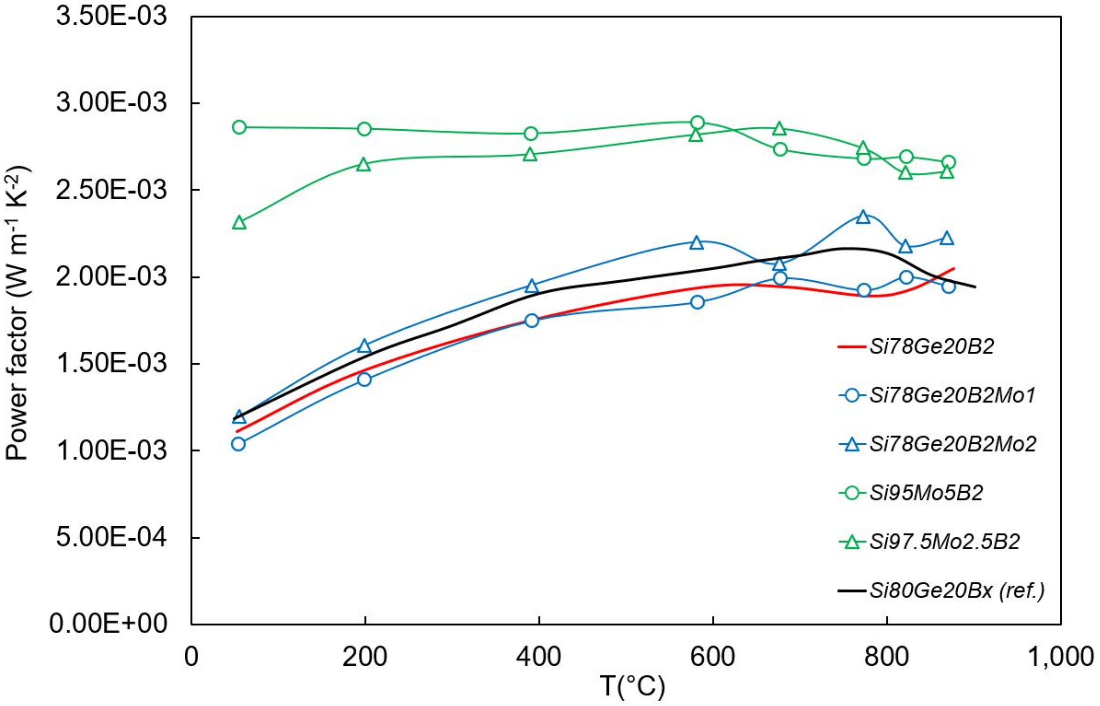

Figure 5.9: Power factor of $Si_{78}Ge_{20}B_2$ samples codoped with Mo, and $SiMoB$ samples

values as the referenced result. We find that Si-Mo-B samples show higher power factors than Si-Ge samples. However, it may not be very helpful to utilize the Si-Mo phase to enhance the figure of merit zT in Si-Ge since Si-Mo system has a much higher thermal conductivity [65] than Si-Ge system. In the end, the enhanced power factor and the high thermal conductivity may cancel out in the zT calculation.

Chapter 6

Conclusion

To summarize the work, we have studied the doping effects in p-type Bi-Sb samples. The samples are synthesized using the melt spinning technique and the spark plasma sintering method. The X-ray diffraction patterns, the scanning electron microscope images, and the energy dispersive spectroscopy results are shown to check the sample quality and the grain features. The Hall coefficient and the doping efficiency are discussed in light of the donor and the acceptor sites in Bi-Sb. It is found that the "high pressure low temperature" method can largely increase the doping level of Ge and the doping efficiency of Pb in Bi-Sb. Several strategies are shown to enhance the power factor in p-type Bi-Sb including: Ge codoped with Pb or Sn; transition metals codoped with Sn or Pb; Te codoped with Sn or Pb; post high-pressure effect. The Ni particles, the Te particles, and the post high-pressure effect show the similar mechanism to enhance the Seebeck of p-type Bi-Sb samples which is the decreased electron/hole mobility ratio. In order to get a high figure of merit zT in p-type Bi-Sb alloys, we need to decrease the electron mobility a lot and keep the good performance of the hole channel. Different Bi-Sb compositions doped with Ni1Pb0.5 are tested. $Bi_{88}Sb_{12}Ni_1Pb_{0.5}$ is found to show the best figure of merit $zT = 0.1{\sim}0.13$ in the temperature range 150∼200 K among all the samples. A two-band effective mass model is applied to fit the resistivity and the Seebeck data of undoped Bi-Sb and pure Ge/Sn/Pb doped Bi-Sb. The band gap shrinking behavior is extracted from the modeling process which partially explains why it is difficult to improve the thermoelectric properties of p-type Bi-Sb. The shrinking band gap makes the electron channel be able to participate in the transport at relatively low temperature which leads to a decreasing p-type Seebeck and an increasing bipolar thermal conductivity.

The resistivity and the Seebeck coefficient have been measured and analyzed for p-type Si-Ge samples. Adding transition metal Fe/Ni particles or aerogel particles affect the carrier concentration and the carrier scattering rate in Si-Ge alloys. The power factor of the samples can be optimized by varying the particle content. Compared with the referenced results, the sample $Si_{78}Ge_{20}B_2Fe_2$ and $Si_{78}Ge_{20}B_2Ni_2$ show about 10 % increase of the power factor in the temperature range 500$\sim$900 °C. The 1 $wt\%$ aerogel embedded Si-Ge sample shows the comparable power factor as the referenced data. Adding Mo into Si-Ge can significantly decrease the resistivity. But the Seebeck coefficient also decreases which keeps the power factor roughly the same. Si-Mo-B samples show the consistent results of decreased resistivity and Seebeck coefficient and the power factors are higher than Si-Ge-B samples. However, the high thermal conductivity of Si-Mo is detrimental to the figure of merit zT of this system which makes this phase less useful in enhancing the thermoelectric performance of Si-Ge alloys.

Appendix A

Detailed equations for modeling thermoelectric transport properties in Bi-Sb

A.1 Effective mass

Conductivity effective mass m_c^*:

$$\frac{1}{m_c^*} = \frac{1}{3}\left(\frac{1}{m_{1'}} + \frac{1}{m_{2'}} + \frac{1}{m_{3'}}\right) \tag{A.1}$$

Density-of-states (DOS) effective mass of a single valley m_b^*:

$$m_b^* = \left(m_{1'} m_{2'} m_{3'}\right)^{1/3} \tag{A.2}$$

Total DOS effective mass m_d^*:

$$m_d^* = N_V^{2/3} m_b^* \tag{A.3}$$

The values of $m_{1'}$, $m_{2'}$, $m_{3'}$ and N_V are found from the literature for Bi-Sb alloys [41].

A.2 Longitudinal elastic constant

Volume fraction of antimony in $Bi_{85}Sb_{15}$: 13 %. Volume fraction of bismuth in $Bi_{85}Sb_{15}$: 87 %. Longitudinal elastic constant of antimony: 9.9×10^{10} $N\,m^{-2}$ [66]. Longitudinal elastic constant of bismuth: 6.3×10^{10} $N\,m^{-2}$ [67]. We use the reciprocal sum to get the longitudinal elastic constant of the alloys:

$$c_l = \left(\frac{0.13}{9.9 \times 10^{10}} + \frac{0.87}{6.3 \times 10^{10}}\right)^{-1} \approx 6.6 \times 10^{10}\,N\,m^{-2} \tag{A.4}$$

A.3 Carrier concentration

$$n = \frac{1}{2\pi^2}\left(\frac{2m^*_{d,n}k_BT}{\hbar^2}\right)^{3/2}\int_{0(CBM)}^{\infty} x^{1/2}\frac{1}{1+e^{x-\eta}}dx \tag{A.5}$$

$$p = \frac{1}{2\pi^2}\left(\frac{2m^*_{d,p}k_BT}{\hbar^2}\right)^{3/2}\int_{-\infty}^{0(VBM)} |x|^{1/2}\left(1-\frac{1}{1+e^{x-\eta-\xi}}\right)dx \tag{A.6}$$

where $\eta = \frac{\mu}{k_BT}$, $\xi = \frac{E_g}{k_BT}$, $x = \frac{E}{k_BT}$, CBM is the conduction band minimum and VBM is the valence band maximum.

A.4 Electrical conductivity

$$\begin{aligned}\sigma &= \sigma_n + \sigma_p \\ &= -\frac{2e^2}{3m^*_{c,n}}\int_0^{\infty}\frac{\partial f_n}{\partial E}D_n(E)E\tau_n dE - \frac{2e^2}{3m^*_{c,p}}\int_0^{\infty}\frac{\partial f_p}{\partial E}D_p(E)E\tau_p dE\end{aligned} \tag{A.7}$$

Taking the ADP scattering time $\tau_{n,p} = \frac{\pi\hbar^4 c_l}{\sqrt{2}k_BT\epsilon_{ac}^2\left(m^*_{b(n,p)}\right)^{3/2}}E^{-1/2}$, let $\eta = \frac{\mu}{k_BT}$,

$\xi = \frac{E_g}{k_B T}$, and $x = \frac{E}{k_B T}$, after changing the variable, we can get

$$\begin{aligned}\sigma = & \frac{2\left(m^*_{d,n}\right)^{3/2}}{3m^*_{c,n}\left(m^*_{b,n}\right)} \frac{e^2 \hbar c_l}{\pi \epsilon^2_{ac}} \int_0^\infty \frac{xexp[x-\eta]}{\left(1+exp[x-\eta]\right)^2} dx + \\ & \frac{2\left(m^*_{d,p}\right)^{3/2}}{3m^*_{c,p}\left(m^*_{b,p}\right)} \frac{e^2 \hbar c_l}{\pi \epsilon^2_{ac}} \int_0^\infty \frac{xexp[x+\eta+\xi]}{\left(1+exp[x+\eta+\xi]\right)^2} dx\end{aligned} \tag{A.8}$$

A.5 Seebeck coefficient

$$\begin{aligned}S = & \frac{S_n \sigma_n + S_p \sigma_p}{\sigma_n + \sigma_p} \\ = & \frac{\frac{2e}{3Tm^*_{c,n}} \int_0^\infty \frac{\partial f_n}{\partial E} D_n(E) E (E-\mu) \tau_n dE - \frac{2e}{3Tm^*_{c,p}} \int_0^\infty \frac{\partial f_p}{\partial E} D_p(E) E (E + E_g + \mu) \tau_p dE}{-\frac{2e^2}{3m^*_{c,n}} \int_0^\infty \frac{\partial f_n}{\partial E} D_n(E) E \tau_n dE - \frac{2e^2}{3m^*_{c,p}} \int_0^\infty \frac{\partial f_p}{\partial E} D_p(E) E \tau_p dE}\end{aligned} \tag{A.9}$$

Let $\eta = \frac{\mu}{k_B T}$, $\xi = \frac{E_g}{k_B T}$, and $x = \frac{E}{k_B T}$, after changing the variable, we can get

$$S = \frac{k_B}{e} \frac{-\int_0^\infty \frac{x(x-\eta)exp[x-\eta]}{(1+exp[x-\eta])^2} dx + \lambda \int_0^\infty \frac{x(x+\eta+\xi)exp[x+\eta+\xi]}{(1+exp[x+\eta+\xi])^2} dx}{\int_0^\infty \frac{xexp[x-\eta]}{(1+exp[x-\eta])^2} dx + \lambda \int_0^\infty \frac{xexp[x+\eta+\xi]}{(1+exp[x+\eta+\xi])^2} dx} \tag{A.10}$$

where $\lambda = \frac{\frac{\left(m^*_{d,p}\right)^{3/2}}{m^*_{c,p}\left(m^*_{b,p}\right)^{3/2}}}{\frac{\left(m^*_{d,n}\right)^{3/2}}{m^*_{c,n}\left(m^*_{b,n}\right)^{3/2}}}$.

Considering the total scattering time τ_{total}, the integral part in the expressions of σ and S will be modified accordingly.

Bibliography

[1] G. J. Snyder and E. S. Toberer, “Complex thermoelectric materials,” *Materials for sustainable energy: a collection of peer-reviewed research and review articles from Nature Publishing Group*, pp. 101–110, 2011.

[2] T. J. Seebeck, *Magnetische polarisation der metalle und erze durch temperatur-differenz*, 70. W. Engelmann, 1895.

[3] J. Goldsmid, *The physics of thermoelectric energy conversion.* Morgan & Claypool Publishers, 2017.

[4] J. C. A. Peltier, *Nouvelles expériences sur la caloricité des courans électriques.* 1834.

[5] W. Thomson, “On a mechanical theory of thermo-electric currents,” *Proceedings of the Royal society of Edinburgh*, vol. 3, pp. 91–98, 1857.

[6] H.-S. Kim, Z. M. Gibbs, Y. Tang, H. Wang, and G. J. Snyder, “Characterization of Lorenz number with Seebeck coefficient measurement,” *APL materials*, vol. 3, no. 4, p. 041 506, 2015.

[7] J. P. Heremans, V. Jovovic, E. S. Toberer, A. Saramat, K. Kurosaki, A. Charoenphakdee, S. Yamanaka, and G. J. Snyder, “Enhancement of thermoelectric efficiency in PbTe by distortion of the electronic density of states,” *Science*, vol. 321, no. 5888, pp. 554–557, 2008.

[8] B. Yu, M. Zebarjadi, H. Wang, K. Lukas, H. Wang, D. Wang, C. Opeil, M. Dresselhaus, G. Chen, and Z. Ren, “Enhancement of thermoelectric prop-

erties by modulation-doping in silicon germanium alloy nanocomposites," *Nano letters*, vol. 12, no. 4, pp. 2077–2082, 2012.

[9] L.-D. Zhao, G. Tan, S. Hao, J. He, Y. Pei, H. Chi, H. Wang, S. Gong, H. Xu, V. P. Dravid, *et al.*, "Ultrahigh power factor and thermoelectric performance in hole-doped single-crystal snse," *Science*, vol. 351, no. 6269, pp. 141–144, 2016.

[10] M. S. Dresselhaus, G. Chen, M. Y. Tang, R. Yang, H. Lee, D. Wang, Z. Ren, J.-P. Fleurial, and P. Gogna, "New directions for low-dimensional thermoelectric materials," *Advanced materials*, vol. 19, no. 8, pp. 1043–1053, 2007.

[11] X. Wang, H. Lee, Y. Lan, G. Zhu, G. Joshi, D. Wang, J. Yang, A. Muto, M. Tang, J. Klatsky, *et al.*, "Enhanced thermoelectric figure of merit in nanostructured n-type silicon germanium bulk alloy," *Applied Physics Letters*, vol. 93, no. 19, p. 193 121, 2008.

[12] G. Joshi, H. Lee, Y. Lan, X. Wang, G. Zhu, D. Wang, R. W. Gould, D. C. Cuff, M. Y. Tang, M. S. Dresselhaus, *et al.*, "Enhanced thermoelectric figure-of-merit in nanostructured p-type silicon germanium bulk alloys," *Nano letters*, vol. 8, no. 12, pp. 4670–4674, 2008.

[13] A. Minnich, M. S. Dresselhaus, Z. Ren, and G. Chen, "Bulk nanostructured thermoelectric materials: Current research and future prospects," *Energy & Environmental Science*, vol. 2, no. 5, pp. 466–479, 2009.

[14] J.-H. Bahk, Z. Bian, and A. Shakouri, "Electron energy filtering by a nonplanar potential to enhance the thermoelectric power factor in bulk materials," *Physical Review B*, vol. 87, no. 7, p. 075 204, 2013.

[15] A. Soni, Y. Shen, M. Yin, Y. Zhao, L. Yu, X. Hu, Z. Dong, K. A. Khor, M. S. Dresselhaus, and Q. Xiong, "Interface driven energy filtering of thermoelectric power in spark plasma sintered $Bi_2Te_{2.7}Se_{0.3}$ nanoplatelet composites," *Nano letters*, vol. 12, no. 8, pp. 4305–4310, 2012.

[16] L. Chen, Y. Liu, J. He, T. M. Tritt, and S. J. Poon, “High thermoelectric figure of merit by resonant dopant in half-Heusler alloys,” *AIP Advances*, vol. 7, no. 6, p. 065 208, 2017.

[17] M. Markov, X. Hu, H.-C. Liu, N. Liu, S. J. Poon, K. Esfarjani, and M. Zebarjadi, “Semi-metals as potential thermoelectric materials,” *Scientific reports*, vol. 8, no. 1, pp. 1–10, 2018.

[18] S. Gao, J. Gaskins, X. Hu, K. Tomko, P. Hopkins, and S. J. Poon, “Enhanced figure of merit in bismuth-antimony fine-grained alloys at cryogenic temperatures,” *Scientific reports*, vol. 9, no. 1, pp. 1–10, 2019.

[19] W. Xie, S. Wang, S. Zhu, J. He, X. Tang, Q. Zhang, and T. M. Tritt, “High performance Bi_2Te_3 nanocomposites prepared by single-element-melt-spinning spark-plasma sintering,” *Journal of Materials Science*, vol. 48, no. 7, pp. 2745–2760, 2013.

[20] H. Zhu, J. Mao, Y. Li, J. Sun, Y. Wang, Q. Zhu, G. Li, Q. Song, J. Zhou, Y. Fu, *et al.*, “Discovery of TaFeSb-based half-Heuslers with high thermoelectric performance,” *Nature communications*, vol. 10, no. 1, pp. 1–8, 2019.

[21] G. J. Snyder and T. S. Ursell, “Thermoelectric efficiency and compatibility,” *Physical review letters*, vol. 91, no. 14, p. 148 301, 2003.

[22] H. Okamoto, “Bi-Sb (bismuth-antimony),” *Journal of Phase Equilibria and Diffusion*, vol. 33, no. 6, pp. 493–494, 2012.

[23] Y. Feutelais, G. Morgant, J. Didry, and J. Schnitter, “Thermodynamic evaluation of the system bismuth-antimony,” *Calphad*, vol. 16, no. 2, pp. 111–119, 1992.

[24] A. Shirzadi, T. Kozieł, G. Cios, and P. Bała, “Development of auto ejection melt spinning (AEMS) and its application in fabrication of cobalt-based ribbons,” *Journal of Materials Processing Technology*, vol. 264, pp. 377–381, 2019.

[25] H. Liebermann and C. Graham, “Production of amorphous alloy ribbons and effects of apparatus parameters on ribbon dimensions,” *IEEE Transactions on Magnetics*, vol. 12, no. 6, pp. 921–923, 1976.

[26] H. Liebermann, “The dependence of the geometry of glassy alloy ribbons on the chill block melt-spinning process parameters,” *Materials science and Engineering*, vol. 43, no. 3, pp. 203–210, 1980.

[27] V. I. Tkatch, A. I. Limanovskii, S. N. Denisenko, and S. G. Rassolov, “The effect of the melt-spinning processing parameters on the rate of cooling,” *Materials Science and Engineering: A*, vol. 323, no. 1-2, pp. 91–96, 2002.

[28] M. Sopicka-Lizer, *High-energy ball milling: mechanochemical processing of nanopowders*. Elsevier, 2010.

[29] O. Guillon, J. Gonzalez-Julian, B. Dargatz, T. Kessel, G. Schierning, J. Räthel, and M. Herrmann, “Field-assisted sintering technology/spark plasma sintering: Mechanisms, materials, and technology developments,” *Advanced Engineering Materials*, vol. 16, no. 7, pp. 830–849, 2014.

[30] M. Zhou, L. Ren, G. Quan, and M. Gupta, “Solid phase processing of metal matrix composites,” 2021.

[31] “Physical property measurement system: Thermal transport option user’s manual,” *Quantum Design*, 2002.

[32] L. J. van der Pauw, “A method of measuring specific resistivity and Hall effect of discs of arbitrary shape,” *Philips Res. Rep*, vol. 13, no. 1, pp. 1–9, 1958.

[33] Z. Du, T. Zhu, Y. Chen, J. He, H. Gao, G. Jiang, T. M. Tritt, and X. Zhao, “Roles of interstitial Mg in improving thermoelectric properties of Sb-doped $Mg_2Si_{0.4}Sn_{0.6}$ solid solutions,” *Journal of Materials Chemistry*, vol. 22, no. 14, pp. 6838–6844, 2012.

[34] A. L. Jain, “Temperature dependence of the electrical properties of bismuth-antimony alloys,” *Physical Review*, vol. 114, no. 6, p. 1518, 1959.

[35] G. Smith and R. Wolfe, "Thermoelectric properties of bismuth-antimony alloys," *Journal of Applied Physics*, vol. 33, no. 3, pp. 841–846, 1962.

[36] W. Yim and A. Amith, "BiSb alloys for magneto-thermoelectric and thermomagnetic cooling," *Solid-State Electronics*, vol. 15, no. 10, pp. 1141–1165, 1972.

[37] B. Lenoir, M. Cassart, J.-P. Michenaud, H. Scherrer, and S. Scherrer, "Transport properties of Bi-rich Bi-Sb alloys," *Journal of Physics and Chemistry of Solids*, vol. 57, no. 1, pp. 89–99, 1996.

[38] R. Wolfe and G. Smith, "Effects of a magnetic field on the thermoelectric properties of a bismuth-antimony alloy," *Applied Physics Letters*, vol. 1, no. 1, pp. 5–7, 1962.

[39] D. Hsieh, D. Qian, L. Wray, Y. Xia, Y. S. Hor, R. J. Cava, and M. Z. Hasan, "A topological Dirac insulator in a quantum spin Hall phase," *Nature*, vol. 452, no. 7190, pp. 970–974, 2008.

[40] B. Lenoir, H. Scherrer, and T. Caillat, "An overview of recent developments for BiSb alloys," *Semiconductors and semimetals*, vol. 69, pp. 101–137, 2001.

[41] M. Dresselhaus, "Electronic properties of the group V semimetals," *J Phys Chem Solids*, vol. 32, no. Suppl 1, pp. 3–33, 1971.

[42] B. Lenoir, A. Dauscher, M. Cassart, Y. I. Ravich, and H. Scherrer, "Effect of antimony content on the thermoelectric figure of merit of $Bi_{1-x}Sb_x$ alloys," *Journal of Physics and Chemistry of Solids*, vol. 59, no. 1, pp. 129–134, 1998.

[43] H. Jin, C. M. Jaworski, and J. P. Heremans, "Enhancement in the figure of merit of p-type $Bi_{100-x}Sb_x$ alloys through multiple valence-band doping," *Applied Physics Letters*, vol. 101, no. 5, p. 053 904, 2012.

[44] Z. Chen, Y. Han, M. Zhou, C. Song, R. Huang, Y. Zhou, and L. Li, "Thermoelectric properties of Ge-doped $Bi_{85}Sb_{15}$ alloys at low temperatures," *Journal of Physics and Chemistry of Solids*, vol. 75, no. 4, pp. 523–527, 2014.

[45] D. M. Brown and F. K. Heumann, “Growth of bismuth-antimony single-crystal alloys,” *Journal of applied physics*, vol. 35, no. 6, pp. 1947–1951, 1964.

[46] V. Zemskov, A. Belaya, G. Kozhemyakin, V. Lyuttsau, and Y. Kostyukova, “Growth of single crystals of bismuth-antimony alloys by Czochralski method,” *Journal of crystal growth*, vol. 71, no. 1, pp. 243–245, 1985.

[47] V. Zemskov, A. Belaya, U. Beluy, and G. Kozhemyakin, “Growth and investigation of thermoelectric properties of Bi-Sb alloy single crystals,” *Journal of crystal growth*, vol. 212, no. 1-2, pp. 161–166, 2000.

[48] Y. S. Hor and R. J. Cava, “Thermoelectric properties of Sn-doped Bi-Sb,” *Journal of alloys and compounds*, vol. 479, no. 1-2, pp. 368–371, 2009.

[49] H. Noguchi, H. Kitagawa, T. Kiyabu, K. Hasezaki, and Y. Noda, “Low temperature thermoelectric properties of Pb-or Sn-doped Bi-Sb alloys,” *Journal of Physics and Chemistry of Solids*, vol. 68, no. 1, pp. 91–95, 2007.

[50] Z. Chen, Y. Han, M. Zhou, C. Song, R. Huang, Y. Zhou, and L. Li, “Improved thermoelectric properties of p-type bismuth antimony-based alloys prepared by spark plasma sintering,” *Journal of electronic materials*, vol. 43, no. 4, pp. 1295–1301, 2014.

[51] L. Norén, R. L. Withers, S. Schmid, F. J. Brink, and V. Ting, “Old friends in a new light: “SnSb” revisited,” *Journal of Solid State Chemistry*, vol. 179, no. 2, pp. 404–412, 2006.

[52] D. M. Brown and S. Silverman, “Electrons in Bi-Sb alloys,” *Physical Review*, vol. 136, no. 1A, A290, 1964.

[53] M. L. Tietze, L. Burtone, M. Riede, B. Lüssem, and K. Leo, “Fermi level shift and doping efficiency in p-doped small molecule organic semiconductors: A photoelectron spectroscopy and theoretical study,” *Physical Review B*, vol. 86, no. 3, p. 035 320, 2012.

[54] D.-Y. Chung, T. P. Hogan, M. Rocci-Lane, P. Brazis, J. R. Ireland, C. R. Kannewurf, M. Bastea, C. Uher, and M. G. Kanatzidis, "A new thermoelectric material: $CsBi_4Te_6$," *Journal of the American Chemical Society*, vol. 126, no. 20, pp. 6414–6428, 2004.

[55] M. V. Vedernikov, V. A. Kutasov, L. N. Luk'yanova, and P. P. Konstantinov, "Recent optimization work on p-type $Bi_{2-x}Sb_xTe_{3-y}Se_y$ alloys reported a low-temperature zT_{max} value of 0.64 at $\sim$ 210 K," *Proceedings of the 16thInternational Conference on Thermoelectrics*, p56, 1997.

[56] M. Lundstrom, *Fundamentals of carrier transport.* Cambridge university press, 2009.

[57] K. Koumoto and T. Mori, *Thermoelectric nanomaterials.* Springer, 2015.

[58] Y. Tang, Z. M. Gibbs, L. A. Agapito, G. Li, H.-S. Kim, M. B. Nardelli, S. Curtarolo, and G. J. Snyder, "Convergence of multi-valley bands as the electronic origin of high thermoelectric performance in $CoSb_3$ skutterudites," *Nature materials*, vol. 14, no. 12, pp. 1223–1228, 2015.

[59] E. E. M. Ph.D., *thesis*, 1979.

[60] K. Malik, D. Das, A. Deb, V. Kulbachinskii, V. Srihari, S. Bandyopadhyay, and A. Banerjee, "Evidence of iso-structural phase transition in rhombohedral Bi-Sb alloy," *EPL (Europhysics Letters)*, vol. 115, no. 5, p. 58 001, 2016.

[61] M. Zebarjadi, G. Joshi, G. Zhu, B. Yu, A. Minnich, Y. Lan, X. Wang, M. Dresselhaus, Z. Ren, and G. Chen, "Power factor enhancement by modulation doping in bulk nanocomposites," *Nano letters*, vol. 11, no. 6, pp. 2225–2230, 2011.

[62] M. Omprakash, K. Delime-Codrin, S. Ghodke, S. Singh, S. Nishino, M. Adachi, Y. Yamamoto, M. Matsunami, S. Harish, M. Shimomura, *et al.*, "Au and B co-doped p-type Si-Ge nanocomposites possessing $zT = 1.63$

synthesized by ball milling and low-temperature sintering," *Japanese Journal of Applied Physics*, vol. 58, no. 12, p. 125 501, 2019.

[63] R. Yamada, A. Masago, T. Fukushima, H. Shinya, T. Q. Nguyen, and K. Sato, "First-principles calculation of electronic density of states and Seebeck coefficient in transition-metal-doped Si-Ge alloys," *Solid State Communications*, vol. 323, p. 114 115, 2021.

[64] M. E. Levinshtein, S. L. Rumyantsev, and M. S. Shur, *Properties of Advanced Semiconductor Materials: GaN, AIN, InN, BN, SiC, SiGe*. John Wiley & Sons, 2001.

[65] Y. Li, J. Han, Q. Xiang, C. Zhang, and J. Li, "Enhancing thermoelectric properties of p-type SiGe by SiMo addition," *Journal of Materials Science: Materials in Electronics*, vol. 30, no. 10, pp. 9163–9170, 2019.

[66] S. Epstein and A. P. deBretteville Jr, "Elastic constants of and wave propagation in antimony and bismuth," *Physical Review*, vol. 138, no. 3A, A771, 1965.

[67] Y. Eckstein, A. Lawson, and D. H. Reneker, "Elastic constants of bismuth," *Journal of Applied Physics*, vol. 31, no. 9, pp. 1534–1538, 1960.